Valvular and coronary blood flow quantification by cardiac 4D flow MRI

Blanken, C.P.S.

Publication date
2022
Document Version
Final published version

VALVULAR AND CORONARY BLOOD FLOW QUANTIFICATION BY CARDIAC 4D FLOW MRI

Carmen P.S. Blanken

Valvular and Coronary Blood Flow Quantification by Cardiac 4D Flow MRI

Carmen P.S. Blanken

Chapter illustrations and cover design: Sanne Fonteijn-Roseboom
Layout: Yasmin Katlich | persoonlijkproefschrift.nl
Printing: Ipskamp Printing | proefschriften.net

Financial support by the Dutch Heart Foundation for the publication of this thesis is gratefully acknowledged.
Further financial support for the publication of this thesis was kindly provided by Pie Medical Imaging BV.

ISBN: 978-94-6421-602-8

Valvular and Coronary Blood Flow Quantification by Cardiac 4D Flow MRI

ACADEMISCH PROEFSCHRIFT

ter verkrijging van de graad van doctor
aan de Universiteit van Amsterdam
op gezag van de Rector Magnificus
prof. dr. ir. K.I.J. Maex
ten overstaan van een door het College voor Promoties ingestelde commissie,
in het openbaar te verdedigen in de Agnietenkapel
op donderdag 3 februari 2022, te 10.00 uur

door Carmen Pieta Susanna Blanken
geboren te Nuenen, Gerwen en Nederwetten

Promotiecommissie

Promotor	prof. dr. ir. A.J. Nederveen	AMC–UvA
Copromotores:	dr. R.N. Planken	AMC–UvA
	dr. ir. P. van Ooij	AMC–UvA
Overige leden:	prof. dr. S. Schnell	Universität Greifswald
	prof. dr. J. van der Velden	Vrije Universiteit Amsterdam
	prof. dr. H.J. Lamb	Universiteit Leiden
	prof. dr. S.A.J. Chamuleau	AMC–UvA
	dr. M. Groenink	AMC–UvA
	dr. E.M. Schrauben	AMC–UvA

Faculteit der Geneeskunde

Contents

Chapter 1	Introduction and thesis outline	7
Chapter 2	Advanced Cardiac MRI Techniques for Evaluation of Left-Sided Valvular Heart Disease	25
Chapter 3	Quantification of Mitral Valve Regurgitation from 4D Flow MRI using Semi-Automated Flow Tracking	53
Chapter 4	Whole-Heart 4D Flow MRI for Evaluation of Normal and Regurgitant Valvular Flow: A Quantitative Comparison Between Pseudo-Spiral Sampling and EPI Readout	77
Chapter 5	Retrospective Camera-Based Respiratory Gating in Clinical Whole-Heart 4D Flow MRI	103
Chapter 6	Coronary Flow Assessment using Accelerated 4D Flow MRI with Respiratory Motion Correction	129
Chapter 7	General discussion and summaries	155
Chapter 8	Appendices	169
	List of publications	170
	PhD portfolio	172
	Acknowledgements	174
	Curriculum vitae	178

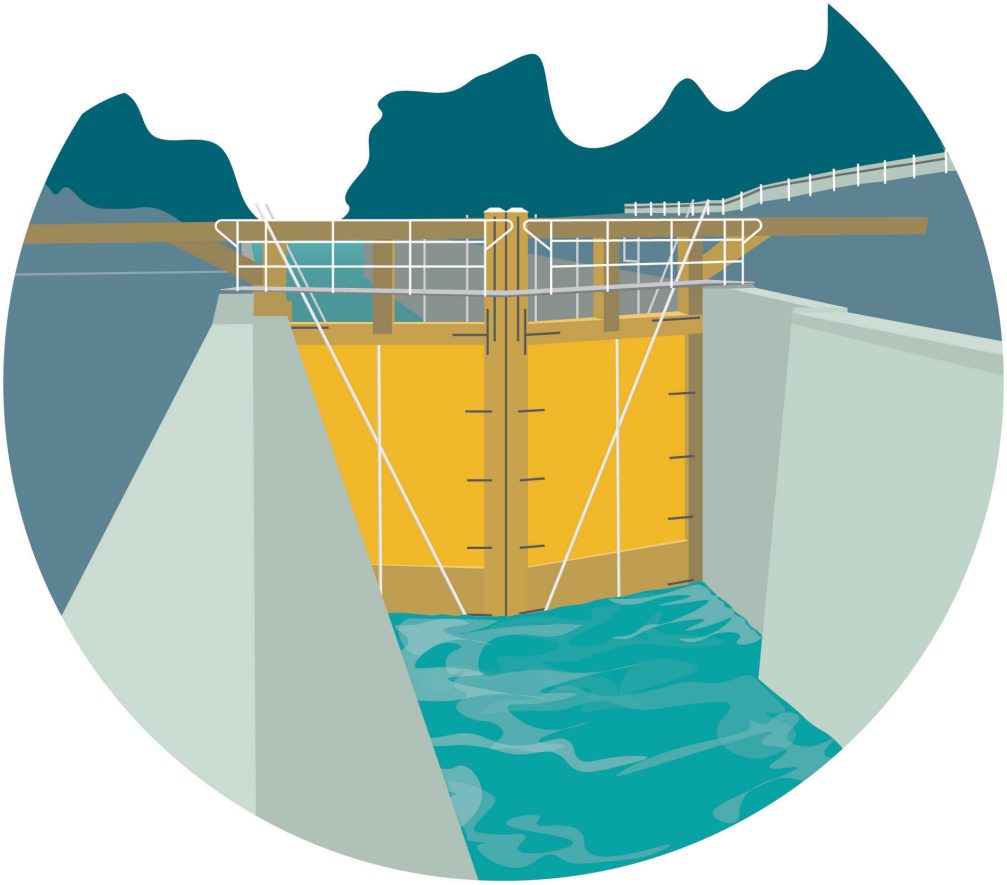

Introduction and thesis outline

1

1.1 Introduction

1.1.1 4D flow MRI

Just like the invention of X-ray in 1895 meant a revolution in the imaging of bones, the recent development of 4D flow MRI has meant a revolution in the imaging of *in vivo* blood flow. Part of the reason these techniques are so revolutionary is that they are non-invasive. On top of that, 4D flow MRI is non-ionizing, and so, does not harm the body.

The application territories of 4D flow MRI include the heart, aorta, pulmonary arteries, carotid arteries, intracranial arteries and abdominal arteries and veins (1–8). Currently, MRI-based assessment of cardiac hemodynamics largely relies on 2D flow MRI, which can characterize blood flow in two-dimensional imaging planes over time[1]. 4D flow imaging is relatively new to the field (9). While it is being implemented in more and more centers, its technical innovation and clinical validation are still in full swing.

1.1.2 Theory behind 4D flow MRI

Unlike X-ray, CT, PET and SPECT, which image body tissues based on their interaction with ionizing radiation, MRI exploits the tissues' interaction with a magnetic field and radio waves. The human body is for about 65% made up of water molecules, each containing two hydrogen atoms, which act like little magnets: when exposed to a magnetic field, their orientations align with the direction of that field. In this context, the hydrogen atoms are called spins, because the magnetic field makes them spin ("precess") around their axes. They do so with a frequency directly proportional to the strength of the magnetic field. This relationship between magnetic field strength and spin precession frequency is central to the workings of MRI.

The first seed for the development of *phase-contrast* or *flow* MRI was planted in 1960 by Erwin Hahn (10). He observed that spins moving through a spatially varying magnetic field develop a phase difference compared to stationary spins. Under the right experimental conditions, these phase differences are proportional to the spins' velocities.

1 The nomenclature of 4D flow MRI is not consistent with that of 2D flow MRI. 4D flow MRI could also be called 3D flow MRI, as the word "flow" already implies its 4th dimension (time).

1.1.2.1 The underlying principle

Consider the following experiments, keeping in mind that there is a proportional relationship between spin precession frequency and magnetic field strength.

1) We place a moving and a stationary spin in a homogeneous magnetic field. Both spins will precess at the same, constant frequency.

2) We repeat the experiment, but give the magnetic field a linear slope in space: a gradient. Depending on their position in the magnetic field, the spins start to either precess faster or slower; for this example, let's assume faster. Whereas the stationary spin reaches a new, constant precession frequency, the moving spin starts to precess *increasingly* faster as it experiences an increasingly stronger magnetic field. Another way of looking at it is: the spins develop a phase difference φ relative to their phases in the homogeneous magnetic field. Whereas the stationary spin's phase difference grows linearly over time, the moving spin's phase difference grows non-linearly.

3) We repeat the experiment, but after the first gradient, apply a second with opposite polarity: a bipolar gradient. The stationary spin's phase difference will return to zero: its linear increase is compensated by a linear decrease. In the moving spin however, the non-linear phase increase is opposed by an even stronger non-linear decrease due to a change in the spin's location (**Figure 1.1**). The final phase difference is proportional to the spin's velocity in the direction of the gradient (11).

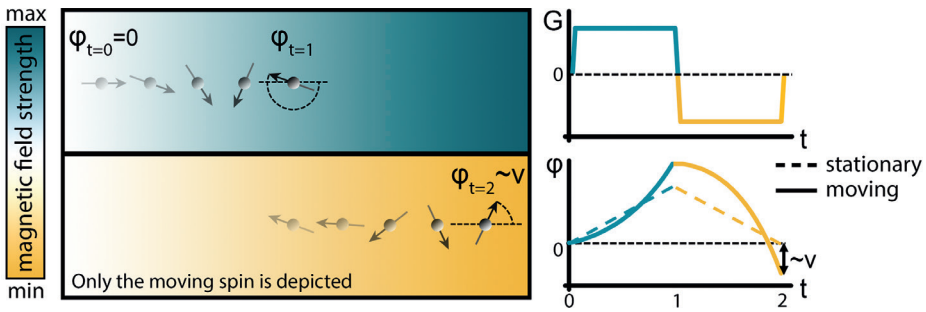

Figure 1.1: a spin moving through a magnetic field to which a bipolar gradient is applied develops a phase difference that is proportional to its velocity. G = gradient strength, φ = phase difference compared to the spin's phase when no gradient is applied, t = time, v = velocity.

In 4D flow MRI, three bipolar gradients are subsequently applied to achieve three-directional, three-dimensional velocity encoding over time (9). To eliminate phase offsets caused by magnetic field inhomogeneities, the bipolar gradients are preceded by a reference measurement with a reversed bipolar gradient. Subtraction with this reference measurement yields a phase map representing just the spins' velocities. However, to get to a phase image in the first place, velocity encoding is not enough; one also needs spatial encoding.

1.1.2.2 Spatial encoding and image reconstruction

All grayscale images have a representation in *k-space*, meaning they can be expressed as a set of overlapping sinusoidal signals, or spatial frequencies, with different amplitudes and directions. K-space can be viewed as the coordinate system in which these frequencies are stored. Translating an image into its representation in k-space is done by Fourier transformation. The opposite can be achieved by inverse Fourier transformation.

During an MRI-scan, what is measured is a set of spatial frequencies that together, after inverse Fourier transformation, constitute an image. The process of collecting the spatial frequencies that characterize a body part is called k-space sampling. It involves clever use of radiofrequency waves and magnetic field gradients causing the body's protons to produce signal echoes (12). Each echo holds information on one line of k-space, along the so-called *frequency-encoding* or *readout* direction. Repeating this line-wise sampling for all instances along the *phase-encoding* direction (and *slice-encoding* direction, in three-dimensional imaging), k-space is fully sampled and an image can be calculated. Electrocardiography (ECG)-based binning of the k-space samples allows for time-resolved imaging of the heart (**Figure 1.2**). In 4D flow MRI, each cardiac bin is reconstructed into three phase images, and a magnitude image for anatomical reference.

Dedicated k-space sampling strategies allow for accelerated imaging; a non-accelerated whole-heart 4D flow MRI scan can easily take longer than an hour. K-space trajectories can be Cartesian, radial, spiral or combinations of those. The sequences handled about in this thesis are an echo planar imaging (EPI) Cartesian sequence (Chapters 3 and 4) and a pseudo-spiral Cartesian sequence (Chapters 4, 5 and 6).

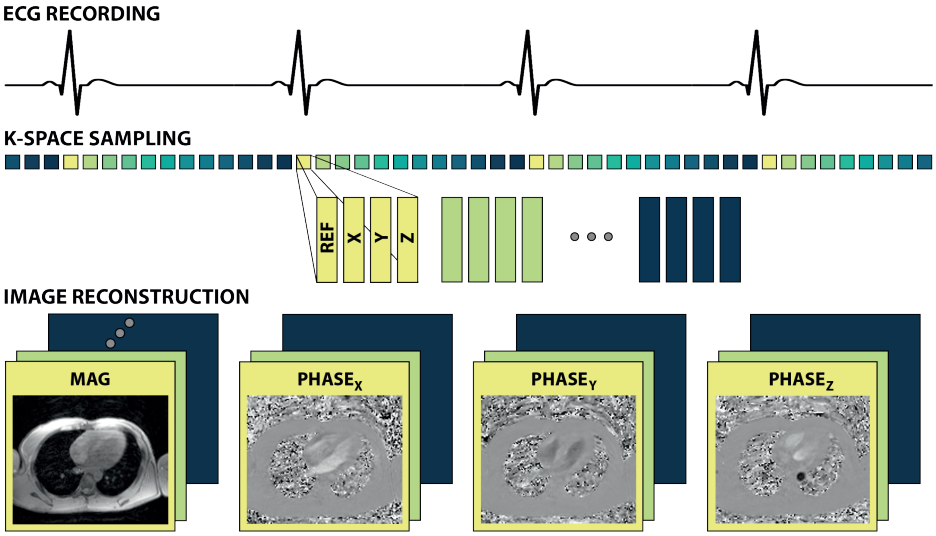

Figure 1.2: electrocardiogram (ECG)-based binning of k-space samples into cardiac frames. Every line of k-space is read out four times: after applying a reversed bipolar gradient (the reference measurement, REF) and after applying bipolar gradients in the three directions x, y and z. From each cardiac bin, a magnitude image and three phase images are reconstructed.

1.1.2.3 Echo planar imaging 4D flow MRI

In EPI 4D flow MRI, instead of reading out one line of k-space after every bipolar gradient, multiple lines are read out (**Figure 1.3**). The EPI factor indicates how many. The EPI sequence used in this thesis is a built-in Philips sequence.

1.1.2.4 Pseudo-spiral 4D flow MRI

Whereas in EPI 4D flow MRI, acceleration is achieved by efficient k-space readout, in pseudo-spiral 4D flow MRI, it is achieved by reducing the total number of k-space readouts. While the missing data points would normally cause image artifacts, iterative compressed sensing (CS) image reconstruction aided by total variation regularization in time provides a way to recover artifact-free images by exploiting image sparsity (13). A condition for this to work is that k-space is incoherently undersampled in space and time, which is achieved by ECG-independent continuous sampling and retrospective cardiac binning. This way, the individual cardiac bins, or time frames, contain different sampling patterns. The sequence is called *pseudo*-spiral because not the k-space readout is spiral, but the sampling pattern between the readouts (**Figure 1.3**). The spirals together make up a sampling pattern that is more dense in the center than in the periphery of k-space.

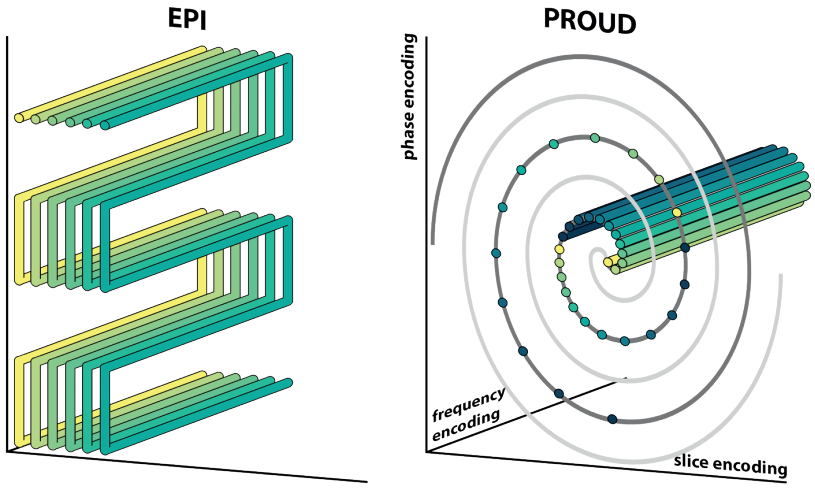

Figure 1.3: EPI and PROUD k-space sampling patterns. Colors correspond to those used in **Figure 1.2**.

As the pseudo-spiral acquisition is facilitated by an in-house developed software modification called "PROspective Undersampling in multiple Dimensions (PROUD)" (14,15), it will be referred to as PROUD 4D flow MRI. An important advantage of PROUD over EPI 4D flow MRI is that its echo times and readout times are shorter, making it less prone to velocity misregistration. Reconstruction-wise, it is flexible in settings like the desired number of cardiac frames and the possibility to perform respiratory motion compensation retrospectively. PROUD is in-house developed and clinically used at Amsterdam UMC for whole-heart imaging in patients with congenital and/or valvular heart disease.

1.1.3 Valvular heart disease

If we were to follow a red blood cell starting from the left atrium of the heart, it would travel across the mitral valve (MV) into the left ventricle, across the aortic valve (AV) into the aorta, make its way through the systemic circulation, and reenter the heart in the right atrium. After traveling across the tricuspid valve (TV) into the right ventricle, and across the pulmonary valve (PV) into the pulmonary artery, it would make its way through the pulmonary circulation to end up in the left atrium again (**Figure 1.4**). The function of the heart valves is to let blood through in one direction and stop it in the opposite direction. The MV and TV open up during ventricular relaxation and close

during ventricular contraction; the opposite holds for the AV and PV. This opening and closing occurs in an entirely passive way, led by continuously changing pressure differences between the different compartments.

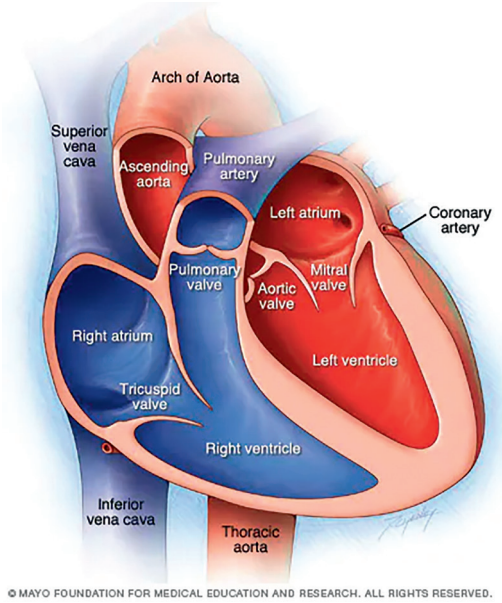

Figure 1.4: the anatomy of the human heart. Reused with permission.

Each valve is made up of two or three leaflets or *cusps*. These cusps are interconnected by a ring-like structure called the valve annulus. The MV has two cusps; the TV, AV and PV each have three. For efficient opening and closing of the valves, these cusps need to be flexible yet sturdy. Moreover, in a closed state, they need to closely fit together. A valve that cannot fully open is called stenotic. A valve that does not properly close can cause blood to leak back, called valvular regurgitation. Both these pathologies undermine the pumping efficiency of the heart, and can, when left untreated, lead to ventricular remodeling and eventually heart failure. Timely clinical evaluation and well-informed clinical decision-making is therefore important.

1.1.3.1 Evaluation by transthoracic echocardiography

Transthoracic echocardiography (TTE) offers a relatively cheap, fast and noninvasive way to obtain information on valve function and anatomy. Moreover, it allows for blood velocity measurement and can be used for severity assessment in valvular stenosis and valvular regurgitation. Its accuracy in measuring regurgitant volumes

is however limited by directional restrictions, operator dependency and the need for assumptions on the geometry of the regurgitation jet – as the acquisition is typically two-dimensional and parallel, or *in-plane*, with the regurgitant jet. While TTE remains the first-line modality for diagnostics and prognostics in valvular regurgitation, recent years have seen a shift toward more frequent use of cardiac MRI: guidelines on the clinical management of valvular regurgitation nowadays recommend the use of MRI when TTE is deemed unreliable (16,17). As a matter of fact, MRI has demonstrated higher prognostic power than echocardiography in the evaluation of MV regurgitation (18–20).

1.1.3.2 Evaluation by cardiac MRI

A typical cardiac MRI exam for the assessment of valvular heart disease consists of a series of breathheld 2D balanced steady state free precession (bSSFP) scans to assess atrial and ventricular volumes and function, followed by 2D flow MRI to quantify forward and backward – or *regurgitant* – flow volumes and velocities across the AV and PV. Blood flow quantification across the MV and TV requires a workaround, because 2D flow MRI at the level of these highly dynamic atrioventricular valves tends to be inaccurate. Key to this workaround is the principle of *what goes around, comes around* – literally speaking: the total amount of blood leaving a cardiac chamber per heartbeat has to equal the total amount of blood entering it per heartbeat. In the left ventricle, that means that the AV forward flow volume (FFV) and MV backward flow volume (BFV, in this thesis denoted as Rvol) together sum up to the same volume as the MV forward and AV backward flow volume. As the total volume leaving the left ventricle per heartbeat is nothing more than the left ventricular stroke volume (LVSV), we can write:

$$LVSV = FFV_{AV} + BFV_{MV} = FFV_{MV} + BFV_{AV}$$

Some reordering leaves:

$$FFV_{MV} = LVSV - BFV_{AV}$$

$$and$$

$$BFV_{MV} = LVSV - FFV_{AV}$$

Hence, using 2D flow MRI to determine AV forward and backward flow volumes and using short-axis bSSFP MRI to determine the LVSV (via planimetric measurement of end-diastolic and end-systolic ventricular volume), MV forward and backward flow volumes can be derived. Likewise, TV forward and backward flow volumes can be derived from the right ventricular stroke volume (RVSV) and PV forward and backward flow volumes. This way, cardiac MRI provides valvular flow quantification across all four heart valves. However, like in echocardiography, the accuracy of the measurements depends on correct positioning of the imaging slices – and thus on operator experience and prior knowledge of the studied pathology. Furthermore, physiological (e.g. heart rate) variability over time can give rise to inaccuracies in parameters that are computed from a combination of different acquisitions, like the flow volumes across the MV and TV. 4D flow MRI is not affected by these sources of error, due to its single-scan, volumetric nature.

1.1.3.3 Evaluation by cardiac 4D flow MRI

Cardiac 4D flow MRI has fostered a better understanding of both healthy and pathological hemodynamics in the human heart. It has been used to study pre- and postoperative hemodynamics in various types of heart disease, including transposition of the great arteries, tetralogy of Fallot, univentricular heart disease and bicuspid aortic valve disease (21–24). In valvular heart disease, it has been used to quantify blood flow volumes, flow eccentricity, peak velocities, (turbulent) kinetic energy and wall shear stress (25–34) (Chapter 2). In **Figure 1.5**, peak-systolic blood flow as recorded by whole-heart 4D flow MRI is depicted in the form of a pathline visualization.

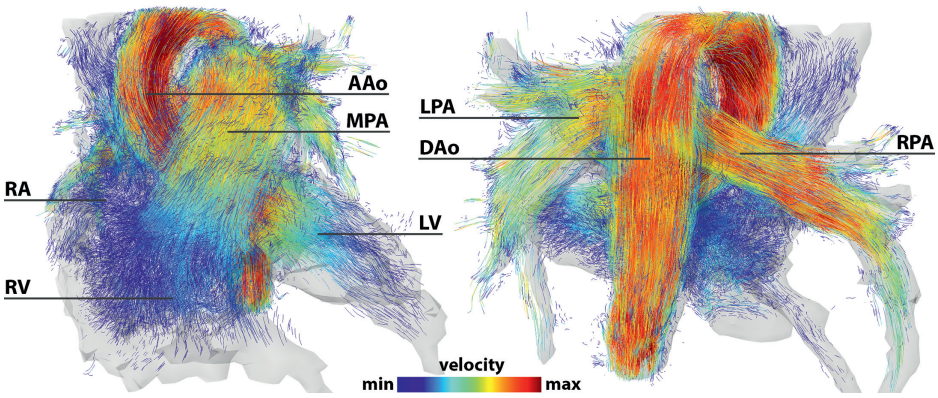

Figure 1.5: Peak-systolic pathline visualization of a whole-heart 4D flow MRI data set, viewed from the front and from the rear. RA/RV = right atrium/ventricle, AAo/DAo = ascending/descending aorta, MPA/LPA/RPA = main/left/right pulmonary artery.

An important focus of this thesis lies on the validation of PROUD and EPI 4D flow MRI for accurate quantification of normal and regurgitant valvular blood flow (Chapters 3 and 4). In this context, 4D flow MRI offers inherent advantages over conventional cardiac MRI. As the time of acquisition is the same throughout the measured volume, all locations of measurement are influenced equally by physiological variability. Furthermore, no choices on specific regions of interest or directions of flow measurement have to be made prior to image acquisition. Only during post-processing, two-dimensional analysis planes are defined. These planes can be placed at any desired location within the scanned volume and can even be made to follow the motion of the heart valves.

1.1.3.4 Retrospective valve tracking and flow tracking

The concept of valve tracking is simple: by making the 4D flow MRI analysis plane move along with the valve, flow is measured right at the level of the valve. This way, no more workaround is needed for flow quantification across the MV and TV. Because the anatomical detail of 4D flow MRI does not (yet) allow localization of the valve annulus, 2D CINE (i.e. time-resolved) bSSFP is used for the actual tracking. The procedure is nowadays largely automated: the only input it requires is manual identification of the valve annulus in a single time frame, in two orthogonal bSSFP views per valve. Feature tracking is then applied to make the four identified points follow the valve annulus over time, such that a frame-specific analysis plane can be defined for analysis of the 4D flow MRI data set.

4D flow MRI in combination with retrospective valve tracking has enabled accurate and reproducible valvular blood flow quantification across all four heart valves (35–37). However, it tends to be inaccurate when it comes to *regurgitant* and *stenotic* flow quantification (38–40). These types of flow are characterized by high velocities, large local velocity differences and turbulence causing signal loss in 4D flow MRI. It was recently suggested that in these circumstances, flow underestimation can be avoided by placing the analysis plane some distance from the valve, where the flow is more laminar and velocities are lower (41,42). This is called flow tracking, as the analysis plane is placed perpendicular to the flow jet and is made to follow it over time. Especially in severe valvular regurgitation, highly eccentric and dynamic flow jets are not uncommon. In Chapter 3, the added value of flow tracking compared to valve tracking is studied for quantification of mild, moderate and severe MV regurgitation.

As mentioned, 4D flow MRI has also been applied to the aorta, pulmonary arteries, carotid arteries, intracranial arteries and abdominal veins. These application territories are all part of either the systemic or the pulmonary circulation. There is a third kind of circulation, the coronary circulation, which has remained unexplored by 4D flow MRI.

1.1.4 Application to coronary artery disease

The coronary circulation ensures that the myocardium receives oxygenated blood before every contraction. After aortic valve closure, part of the blood that just entered the ascending aorta finds its way into the coronary arteries. The blood is then guided into a tree of arterioles and capillaries embedded in the myocardium. Once deoxygenated, the blood is channeled back into venules and veins, ending up in the coronary sinus, which drains into the right atrium.

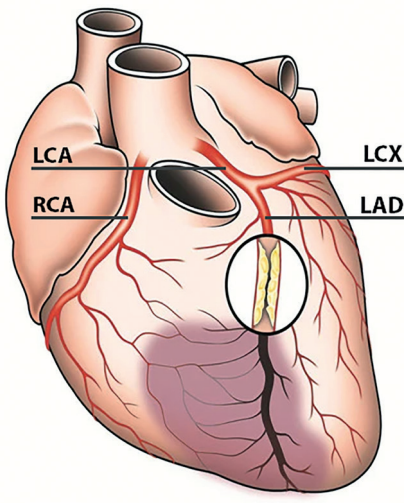

Figure 1.6: the coronary vasculature, with an obstructed left anterior descending (LAD) coronary artery resulting in reduced blood flow to the myocardium. LCA/RCA = left/right coronary artery, LCX = left circumflex coronary artery.

In obstructive coronary artery disease (CAD), the coronary arteries are narrowed due to plaque, reducing blood flow to the myocardium (**Figure 1.6**). The clinical evaluation of obstructive CAD relies on catheter-based, and thus invasive, coronary artery angiography. MRI can potentially be used as a non-invasive screening modality, as it offers coronary angiography for morphological assessment, and myocardial perfusion and coronary flow measurement for functional assessment (43–45). To date, MRI-

based coronary flow measurement has only been performed in a 2D fashion, limiting its clinical applicability. Getting 4D flow MRI to work in the coronary arteries could play a pivotal role in the diagnostic workup of CAD patients. However, while there is much to gain from coronary 4D flow MRI, its technical challenges are considerable and have hindered its realization up to now. A combination of factors plays a role, the most important being the small diameter of the coronary arteries, necessitating high spatial resolution at the cost of longer scan time. On top of that, the coronary arteries move with every heartbeat and with every breath, necessitating advanced acquisition and post-processing strategies to avoid image blurring. These challenges are tackled in Chapter 6.

1.1.5 Respiratory motion compensation

Respiratory motion can be monitored and compensated for in different ways. A monitoring technique commonly used in cardiac 4D flow MRI is lung-liver interface navigation. By periodically acquiring signal in a small beam-shaped area crossing the diaphragm, the up-and-down motion of the liver can be kept track of during the 4D flow scan. Another approach is to record the motion of the breast cage using a camera installed in the MRI machine. This method recently became available and is a subject of study in Chapter 5, in a comparison with lung-liver navigation.

Once recorded, the respiratory motion can be accounted for to mitigate its effect on the image quality. One way is to use only k-space samples that were acquired during end-expiration. This method, called respiratory gating and used in Chapter 5, is easy to implement but results in exclusion of typically about fifty percent of the acquired data. Higher efficiency is achieved by more advanced methods that translate the recorded respiration heights into phase shifts in k-space that, after image reconstruction, result in alignment of the different respiration heights. In Chapter 6, respiratory motion correction based on lung-liver navigation is employed to reduce image blurring in coronary 4D flow MRI.

1.2 Thesis outline

This thesis concerns the innovation and validation of cardiac 4D flow MRI for blood flow quantification in valvular heart disease and coronary artery disease.

Chapter 2 reviews the current status of 4D flow MRI in the evaluation of left-sided valvular heart disease. Current clinical imaging techniques (echocardiography and MRI) are discussed, followed by an overview of novel hemodynamic parameters derived from 4D flow MRI and their potential for prognosis and treatment planning. Furthermore, we discuss the role of tissue mapping and strain quantification in the assessment of left-sided valvular heart disease.

Chapter 3 investigates the potential of 4D flow MRI in combination with flow tracking for quantification of mild, moderate and severe MV regurgitation. We compare flow tracking with valve tracking in terms of intervalve consistency, agreement with conventional MRI, and interobserver agreement. Severity grading based on regurgitant volume measurements allows for comparison with semiquantitative echocardiography-based grading.

In **Chapter 4**, we investigate the robustness of PROUD whole-heart 4D flow MRI with compressed sensing reconstruction for quantification of normal and regurgitant blood flow across the heart valves. We compare its performance to that of a clinically used EPI readout strategy, and investigate the possibility of shortening the scan time further by increasing the undersampling factor.

Chapter 5 evaluates the application of retrospective respiratory gating to whole-heart 4D flow MRI in a cohort of patients with congenital and/or valvular heart disease. Camera-based and lung-liver navigator-based gating are tested for their effect on the image quality and on valvular flow measurements.

Chapter 6 presents a framework for non-invasive coronary blood flow quantification using PROUD-accelerated 4D flow MRI equipped with respiratory motion correction. We test its feasibility and reproducibility in healthy subjects at rest, using 2D flow MRI flow and velocity measurements as a reference.

In **Chapter 7**, the findings of this thesis are discussed and summarized.

1.3 References

1. Markl M, Frydrychowicz A, Kozerke S, Hope M, Wieben O. 4D flow MRI. J Magn Reson Imaging. 2012;36(5):1015–1036.
2. Ha H, Kim GB, Kweon J, et al. Hemodynamic measurement using four-dimensional phase-contrast MRI: Quantification of hemodynamic parameters and clinical applications. Korean J Radiol. 2016;17(4):445–462.
3. Crandon S, Elbaz MSM, Westenberg JJM, van der Geest RJ, Plein S, Garg P. Clinical applications of intra-cardiac four-dimensional flow cardiovascular magnetic resonance: A systematic review. Int J Cardiol. 2017;249:486–493.
4. Kamphuis VP, Westenberg JJM, van der Palen RLF, et al. Unravelling cardiovascular disease using four dimensional flow cardiovascular magnetic resonance. Int J Cardiovasc Imaging. 2017;33(7):1069–1081.
5. Alabed S, Garg P, Johns CS, et al. Cardiac Magnetic Resonance in Pulmonary Hypertension—an Update. Curr Cardiovasc Imaging Rep. 2020;13(12):30.
6. Youn S, Lee J. From 2D to 4D Phase-Contrast MRI in the Neurovascular System: Will It Be a Quantum Jump or a Fancy Decoration? J Magn Reson Imaging. 2020;doi:10.1002/jmri.27430.
7. Riedel C, Lenz A, Fischer L, et al. Abdominal Applications of 4D Flow MRI. RöFo - Fortschritte auf dem Gebiet der Röntgenstrahlen und der Bildgeb Verfahren. 2020;193(4):388–398.
8. Haarbye SO, Nielsen MB, Hansen AE, Lauridsen CA. Four-Dimensional Flow MRI of Abdominal Veins: A Systematic Review. Diagnostics. 2021;11(5):767.
9. Markl M, Chan FP, Alley MT, et al. Time-resolved three-dimensional phase-contrast MRI. J Magn Reson Imaging. 2003;17(4):499–506.
10. Hahn EL. Detection of sea-water motion by nuclear precession. J Geophys Res. 1960;65(2):776–777.
11. Walker MF, Souza SP, Dumoulin CL. Quantitative flow measurement in phase contrast MR angiography. J Comput Assist Tomogr. 1988;12(2):304–313.
12. Bernstein MA, King KF, Zhou XJ. Handbook of MRI pulse sequences. 2004.
13. Lustig M, Donoho D, Pauly JM. Sparse MRI: The application of compressed sensing for rapid MR imaging. Magn Reson Med. 2007;58(6):1182–1195.
14. Gottwald LM, Peper ES, Zhang Q, et al. Pseudo-spiral sampling and compressed sensing reconstruction provides flexibility of temporal resolution in accelerated aortic 4D flow MRI: A comparison with k-t principal component analysis. NMR Biomed. 2020;33(4):e4255.
15. Peper ES, Gottwald LM, Zhang Q, et al. Highly accelerated 4D flow cardiovascular magnetic resonance using a pseudo-spiral Cartesian acquisition and compressed sensing reconstruction for carotid flow and wall shear stress. J Cardiovasc Magn Reson. 2020;22(1):7.
16. Zoghbi, Adams D, Bonow RO, et al. Recommendations for Noninvasive Evaluation of Native Valvular RegurgitationA Report from the American Society of Echocardiography Developed in Collaboration with the Society for Cardiovascular Magnetic Resonance. J Indian Acad Echocardiogr Cardiovasc Imaging. 2020;4(1):58.
17. Vahanian A, Beyersdorf F, Praz F, et al. 2021 ESC/EACTS Guidelines for the management of valvular heart disease. Eur. Heart J. 2021.
18. Uretsky S, Gillam L, Lang R, et al. Discordance between echocardiography and MRI in the assessment of mitral regurgitation severity: a prospective multicenter trial. J Am Coll Cardiol. 2015;65(11):1078–1088.
19. Myerson SG, D'Arcy J, Christiansen JP, et al. Determination of Clinical Outcome in Mitral Regurgitation With Cardiovascular Magnetic Resonance Quantification. Circulation. 2016;133(23):2287–2296.

20. Penicka M, Vecera J, Mirica DC, Kotrc M, Kockova R, Van Camp G. Prognostic Implications of Magnetic Resonance-Derived Quantification in Asymptomatic Patients With Organic Mitral Regurgitation: Comparison With Doppler Echocardiography-Derived Integrative Approach. Circulation. 2017;137(13):1349–1360.
21. Warmerdam E, Krings GJ, Leiner T, Grotenhuis HB, Heynric D, Grotenhuis B. Three-dimensional and four-dimensional flow assessment in congenital heart disease. Heart. 2020;106(6):421–426.
22. Elsayed A, Gilbert K, Scadeng M, Cowan BR, Pushparajah K, Young AA. Four-dimensional flow cardiovascular magnetic resonance in tetralogy of Fallot: a systematic review. J Cardiovasc Magn Reson. 2021;23(1):1–23.
23. Cave DGW, Panayiotou H, Bissell MM. Hemodynamic Profiles Before and After Surgery in Bicuspid Aortic Valve Disease—A Systematic Review of the Literature. Front Cardiovasc Med. 2021;8:201.
24. Thakkar AN, Chinnadurai P, Huie Lin C. Imaging adult patients with coarctation of the aorta. Curr Opin Cardiol. 2017;32(5):503–512.
25. Eriksson J, Carlhäll C, Dyverfeldt P, Engvall J, Bolger AF, Ebbers T. Semi-automatic quantification of 4D left ventricular blood flow. J Cardiovasc Magn Reson. 2010;12(1):9.
26. Palen RLF van der, Deurvorst QS, Kroft LJM, et al. Altered Ascending Aorta Hemodynamics in Patients After Arterial Switch Operation for Transposition of the Great Arteries. J Magn Reson Imaging. 2020;51(4):1105–1116.
27. Rahman O, Scott M, Bollache E, et al. Interval changes in aortic peak velocity and wall shear stress in patients with bicuspid aortic valve disease. Int J Cardiovasc Imaging 2019 3510. 2019;35(10):1925–1934.
28. Al-Wakeel N, Fernandes JF, Amiri A, et al. Hemodynamic and energetic aspects of the left ventricle in patients with mitral regurgitation before and after mitral valve surgery. J Magn Reson Imaging. 2015;42(6):1705–1712.
29. Sjöberg P, Bidhult S, Bock J, et al. Disturbed left and right ventricular kinetic energy in patients with repaired tetralogy of Fallot: pathophysiological insights using 4D-flow MRI. Eur Radiol. 2018;28(10):4066–4076.
30. Elhawaz A, Archer GT, Zafar H, et al. Left ventricular blood flow kinetic energy is associated with the six-minute walk test and left ventricular remodelling post valvular intervention in aortic stenosis. Quant Imaging Med Surg. 2021;11(4):1470–1482.
31. Giese D, Weiss K, Baeßler B, et al. In vitro evaluation of flow patterns and turbulent kinetic energy in trans-catheter aortic valve prostheses. Magn Reson Mater Physics, Biol Med. 2017;31(1):165–172.
32. Fredriksson A, Trzebiatowska-Krzynska A, Dyverfeldt P, Engvall J, Ebbers T, Carlhäll C-J. Turbulent kinetic energy in the right ventricle: Potential MR marker for risk stratification of adults with repaired Tetralogy of Fallot. J Magn Reson Imaging. 2018;47(4):1043–1053.
33. van Ooij P, Markl M, Collins JD, et al. Aortic valve stenosis alters expression of regional aortic wall shear stress: New insights from a 4-dimensional flow magnetic resonance imaging study of 571 subjects. J Am Heart Assoc. 2017;6(9):1–14.
34. Farag ES, Ooij P van, Planken RN, et al. Aortic valve stenosis and aortic diameters determine the extent of increased wall shear stress in bicuspid aortic valve disease. J Magn Reson Imaging. 2018;48(2):522–530.
35. Roes SD, Hammer S, van der Geest RJ, et al. Flow assessment through four heart valves simultaneously using 3-dimensional 3-directional velocity-encoded magnetic resonance imaging with retrospective valve tracking in healthy volunteers and patients with valvular regurgitation. Invest Radiol. 2009;44(10):669–675.
36. Hsiao A, Tariq U, Alley MT, Lustig M, Vasanawala SS. Inlet and outlet valve flow and regurgitant volume may be directly and reliably quantified with accelerated, volumetric phase-contrast MRI. J Magn Reson Imaging. 2015;41(2):376–385.

37. Kamphuis VP, Roest AAW, Ajmone Marsan N, et al. Automated Cardiac Valve Tracking for Flow Quantification with Four-dimensional Flow MRI. Radiology. 2019;290(1):70–78.
38. Gatenby JC, McCauley TR, Gore JC. Mechanisms of signal loss in magnetic resonance imaging of stenoses. Med Phys. 1993;20(4):1049–1057.
39. Westenberg JJ., van der Geest RJ, Wasser MNJ., et al. Objective stenosis quantification from post-stenotic signal loss in phase-contrast magnetic resonance angiographic datasets of flow phantoms and renal arteries. Magn Reson Imaging. 1998;16(3):249–260.
40. Kweon J, Yang DH, Kim GB, et al. Four-dimensional flow MRI for evaluation of post-stenotic turbulent flow in a phantom: comparison with flowmeter and computational fluid dynamics. Eur Radiol. 2016;26(10):3588–3597.
41. Myerson SG, Francis JM, Neubauer S. Direct and indirect quantification of mitral regurgitation with cardiovascular magnetic resonance, and the effect of heart rate variability. Magn Reson Mater Physics, Biol Med. 2010;23(4):243–249.
42. Calkoen EE, Westenberg JJ, Kroft LJ, et al. Characterization and quantification of dynamic eccentric regurgitation of the left atrioventricular valve after atrioventricular septal defect correction with 4D Flow cardiovascular magnetic resonance and retrospective valve tracking. J Cardiovasc Magn Reson. 2015;17(1):18.
43. Motwani M, Swoboda PP, Plein S, Greenwood JP. Role of cardiovascular magnetic resonance in the management of patients with stable coronary artery disease. Heart. 2018;104(11):888–894.
44. Roy CW, Heerfordt J, Piccini D, et al. Motion compensated whole-heart coronary cardiovascular magnetic resonance angiography using focused navigation (fNAV). J Cardiovasc Magn Reson. 2021;23(1):33.
45. Zhu D, Bonanno G, Hays AG, Weiss RG, Schär M. Phase contrast coronary blood velocity mapping with both high temporal and spatial resolution using triggered Golden Angle rotated Spiral k-t Sparse Parallel imaging (GASSP) with shifted binning. Magn Reson Med. 2021;86(4):1929–1943.

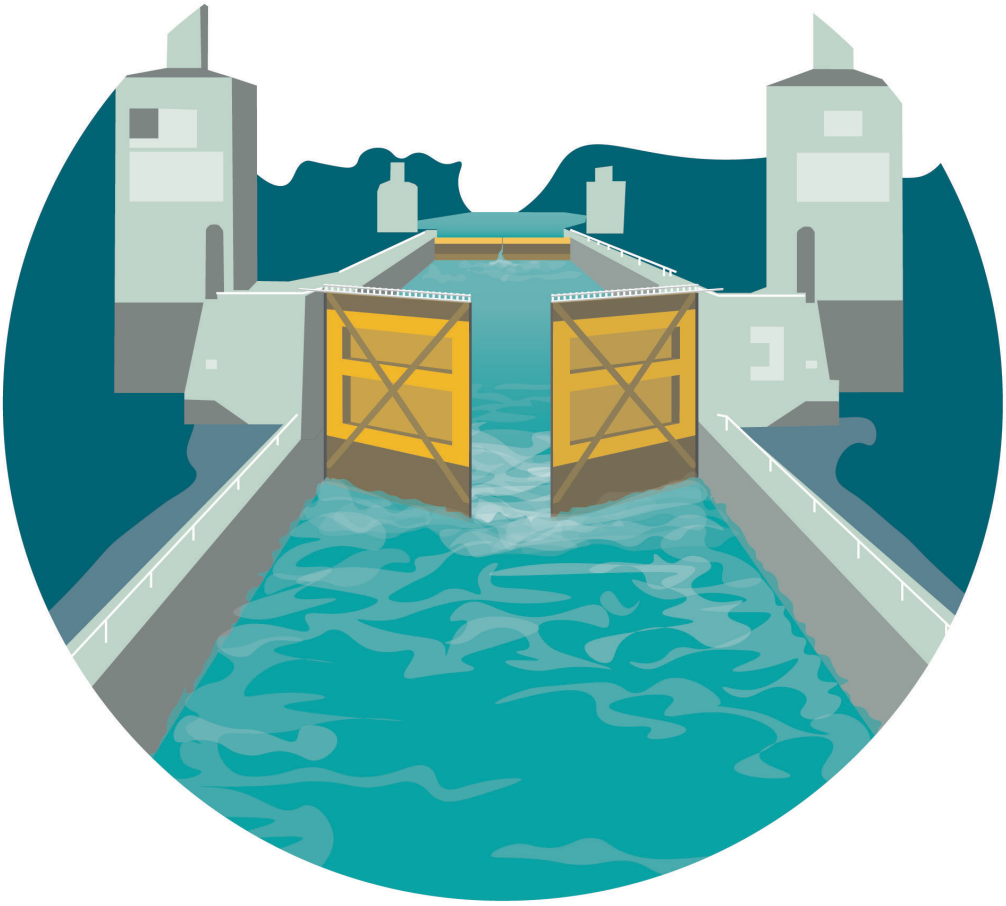

Advanced Cardiac MRI Techniques for Evaluation of Left-Sided Valvular Heart Disease

2

Carmen P.S. Blanken*
Emile S. Farag*
S. Matthijs Boekholdt
Tim Leiner
Jolanda Kluin
Aart J. Nederveen
Pim van Ooij
R. Nils Planken
*contributed equally

J. Magn. Reson. Imaging 2018; 48: 318–329.

Abstract

The most common types of left-sided valvular heart disease (VHD) in the Western world are aortic valve stenosis (AS), aortic valve regurgitation (AR) and mitral valve regurgitation (MR). Comprehensive clinical evaluation entails both hemodynamic analysis and structural as well as functional characterization of the left ventricle. Cardiac magnetic resonance imaging (MRI) is an established diagnostic modality for assessment of left-sided VHD and is progressively gaining ground in modern-day clinical practice. Detailed flow visualization and quantification of flow-related biomarkers in VHD can be obtained using 4D flow MRI, an imaging technique capable of measuring blood flow in three orthogonal directions over time. In addition, recent MRI sequences enable myocardial tissue characterization and strain analysis. In this review, we will discuss the emerging potential of state-of-the-art MRI including 4D flow MRI, tissue mapping and strain quantification for the diagnosis, prognosis and treatment planning of left-sided VHD.

2.1 Introduction

Cardiac magnetic resonance imaging (MRI) and echocardiography are non-invasive imaging modalities that are of paramount importance in daily clinical practice for diagnosis, prognosis and treatment planning in patients with left-sided valvular heart disease (VHD) (1–3). The most common types of left-sided VHD in the Western world are aortic valve stenosis (AS), aortic valve regurgitation (AR) and mitral valve regurgitation (MR), with estimated prevalences of 0.4%, 0.5% and 1.7%, respectively (4). AS is most often caused by degenerative calcification of the aortic valve leaflets, whereas AR can result from stiffening of the valve due to calcification, but can also occur as a result of aortic valve endocarditis or secondary to aortic annulus dilatation (5). MR is generally divided into two categories: primary organic MR, which occurs as a result of an intrinsically abnormal mitral valve, and functional MR which develops secondary to left ventricular (LV) dysfunction or annular dilatation prohibiting normal valve closure (6). AS, AR and MR may all lead to LV remodeling due to LV pressure and/or volume overload and eventually heart failure.

Cardiac MRI is the standard of reference for the quantification of ventricular volumes, mass and function and is a highly valuable and reproducible tool in the diagnostic armamentarium for VHD (1,7). Images are typically obtained using time-resolved (cine) MRI techniques, allowing targeted imaging of all heart valves and myocardial structures during the cardiac cycle. Furthermore, MR angiography allows for assessment of large vessels like the aorta, with or without the use of contrast agents. However, to investigate which hemodynamic mechanisms drive disease progression in VHD, three-dimensional evaluation of flow patterns is indispensable, as two-dimensional imaging does not fully capture complex blood flow.

Four-dimensional flow MRI (4D flow MRI or time-resolved three-dimensional phase-contrast MRI with three-directional velocity encoding) is an imaging modality capable of measuring blood flow in the three principal directions and as a function of time, allowing for accurate quantification of blood flow in patients with VHD. An example acquisition protocol for cardiac MRI including 4D flow MRI can be found in Allen et al. (8). 4D flow MRI-derived parameters, such as wall shear stress and kinetic energy, enable characterization of hemodynamic mechanisms in patients with left-sided VHD. In addition, tissue characterization techniques such as T1- and T2-mapping enable quantification of myocardial fibrosis, extracellular volume (ECV) fraction and edema,

which can be used to study the effects of VHD on the myocardium. Strain analysis provides functional information regarding the contractility of the heart, facilitating timely identification of myocardial dysfunction (9). Thus, novel state-of-the-art cardiac MRI techniques include 4D flow MRI, tissue characterization mapping and strain quantification (8).

In this review, we provide a comprehensive overview of advanced MRI techniques for the evaluation of left-sided VHD. Current clinical imaging techniques (echocardiography and MRI) will be discussed, followed by an overview of novel hemodynamic parameters derived from 4D flow MRI and their diagnostic and prognostic potential. Finally, we will discuss the role of tissue mapping and strain quantification in left-sided VHD.

2.2 Current clinical diagnostic tools

2.2.1 Echocardiography

Current clinical guidelines recommend transthoracic echocardiography (TTE) or transesophageal echocardiography (TEE) as the first-line diagnostic modality for the evaluation of left-sided VHD (1). TTE is relatively cheap, fast, non-invasive and can be performed real-time at the bedside to acquire relevant information on valve function and anatomy. Furthermore, cardiac blood flow assessment is possible using the color Doppler mode. In AS patients, echocardiography can be used to assess aortic valve morphology, as well as several parameters to grade AS severity including peak systolic blood flow velocities and derivatives such as transvalvular pressure gradients and the aortic valve area (AVA) (1). In AR, echocardiography can be used to assess valve morphology and the direction and severity of the regurgitation jet (1). Quantification of AR can be performed by measuring the regurgitation fraction, but is typically performed taking into account a variety of parameters such as LV dilatation, the width of the regurgitant jet (vena contracta width), pressure half-time and the presence of flow reversal in the descending aorta. In patients with MR, echocardiography is useful to discriminate organic from functional MR. Assessment of MR severity is based on a range of qualitative and semiquantitative measures, including valve morphology and movement, LV dilatation and function, left atrial dilatation, effective regurgitant orifice area, vena contracta width, flow reversal in the pulmonary veins and pulmonary artery pressure (1,10).

One of the main limitations of routine 2D echocardiography for hemodynamic assessment is that due to the assumption of a circular geometry of the flow pattern, the complex dynamic nature of the blood flow tends to be overlooked. As a result, quantification of transvalvular flow is challenging and possibly inaccurate. Also, echocardiography can only measure velocities in line with the transducer beam, making it susceptible to errors caused by misalignment of the transducer beam to the direction of the blood flow, especially for eccentric and dynamic flow jets (11,12). Furthermore, the complex geometry and dynamic nature of the valve apparatus during the cardiac cycle is not fully captured. Although three-dimensional (3D) echocardiography enables more comprehensive, volumetric imaging of the heart, spatial and temporal resolutions are poorer and its clinical applicability is limited due to the significant learning curve (13).

2.2.2 Current clinical cardiac MRI

MRI is becoming increasingly important in the assessment of left-sided VHD in addition to echocardiography, providing accurate information on functional and morphological valvular abnormalities, VHD severity and LV function. Recent clinical guidelines recommend MRI as an alternative for inconclusive TTE examinations, caused by poor acoustic windows for instance (1,14). Using steady state free precision (SSFP) imaging and accurate adjustment of imaging planes, all four heart valves can be visualized in predefined imaging planes (3). 2D phase-contrast velocity mapping enables quantification of blood flow volumes and velocities across heart valves. However, single-slice cine imaging for the assessment of AS, AR or MR requires manual positioning of the imaging plane and is thus sensitive to measurement errors due to incorrect plane position and angulation. In addition, imaging in a fixed plane does not allow for accurate assessment of dynamic cardiac structures, which is particularly relevant for the atrioventricular valves. Thus, although MRI is considered more accurate and reproducible than echocardiography in the assessment of ventricular volumes and flow across the heart valves (15,16), finding the correct imaging plane during acquisition and accurately delineating structures during post-processing remains a challenge. The most important advantages and disadvantages of cardiac MRI and echocardiography for the quantitative assessment of VHD are summarized in a publication by Thavendiranathan et al. (13).

2.3 4D flow MRI

4D flow MRI, or time-resolved three-dimensional phase-contrast MRI, is powerful in its capability to non-invasively measure blood flow velocities *in vivo* within a volume in the three principal directions. It allows for the dynamic quantification of blood flow in both the heart and the great vessels with good spatial and temporal resolutions. Pathline or streamline visualizations provide insight into 3D hemodynamics and 4D flow MRI-derived hemodynamic parameters may aid in the evaluation of VHD (**Figure 2.1**). Scan times range from 5 to 10 minutes with the use of advanced acceleration techniques and respiratory motion is usually compensated for with navigator gating at the lung-liver interface or a respiratory belt. Recommended acquisition parameters have been stated by Dyverfeldt et al. (17).

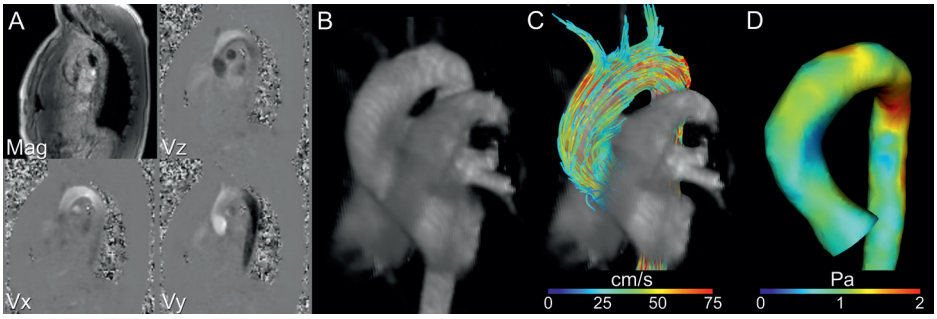

Figure 2.1: A) Thoracic 4D flow MRI acquisition consisting of magnitude (Mag) and velocity data in the three principal spatial dimensions (Vx, Vy and Vz), **B)** Phase contrast MR angiogram, **C)** Systolic pathline visualization of the thoracic aorta, color-coded for velocity and **D)** Systolic wall shear stress visualization.

In 4D flow MRI, velocity data are acquired in an entire volume of interest, enabling blood flow quantification during post-processing in any desired orientation. Consequently, 4D flow MRI is better suited for visualization and quantification of eccentric and dynamic transvalvular flow patterns than 2D PC-MRI (18,19). Valve orifice areas and pressure gradients can be calculated from peak flow velocities using the simplified Bernoulli equation (20). 4D flow MRI in combination with valve tracking offers the possibility to quantify transvalvular blood flow corrected for cardiac motion, and has been shown to yield good correlations across heart valves (21–23). Dedicated software facilitates semi-automated retrospective valve tracking, using two orthogonal cine MRI acquisitions to locate the valve annulus during each cardiac phase. As a result, the quantification plane closely follows the valve orifice throughout the

cardiac cycle. This is especially valuable for the atrioventricular heart valves, which have a complex valvular and annular anatomy and are highly dynamic. The use of 2D PC-MRI to measure net flows over the mitral valve (MV) and tricuspid valve (TV) has been associated with markedly lower correlations between valves than 4D flow MRI with valve tracking (Pearson's $r = 0.34$, $p = 0.34$ for 2D PC-MRI as opposed to $r = 0.91$, $P < 0.01$ for 4D flow MRI) (23).

Furthermore, various advanced hemodynamic parameters can be extracted from 4D flow MRI-acquired data. In this section, we will provide a brief overview of 4D flow MRI-derived hemodynamic parameters that may aid in the clinical evaluation of left-sided VHD. The application of 4D flow MRI to AS, AR and MR as proposed in current literature will be discussed in the subsequent section.

2.3.1 Wall shear stress

Wall shear stress (WSS) is defined as the viscous shear force of flowing blood acting tangentially on the vessel wall. It is the frictional force of the blood on the vascular endothelium and has been associated with vessel wall remodeling (24). 4D flow MRI can be used to calculate regional aortic WSS from near-wall blood flow velocity gradients (25). **Figure 2.2** shows examples of peak systolic patient-specific velocity vectors and cohort-averaged WSS patterns in the thoracic aorta of patients with aortic dilatation distal to a trileaflet aortic valve with and without AS. Histological validation shows that regions with increased WSS are subject to extracellular matrix degradation and elastic fiber degeneration in the ascending aorta of patients with bicuspid aortic valve (BAV) disease (26). Longitudinal studies will have to determine whether WSS is a good predictor of aortopathy in patients with aortic valve disease.

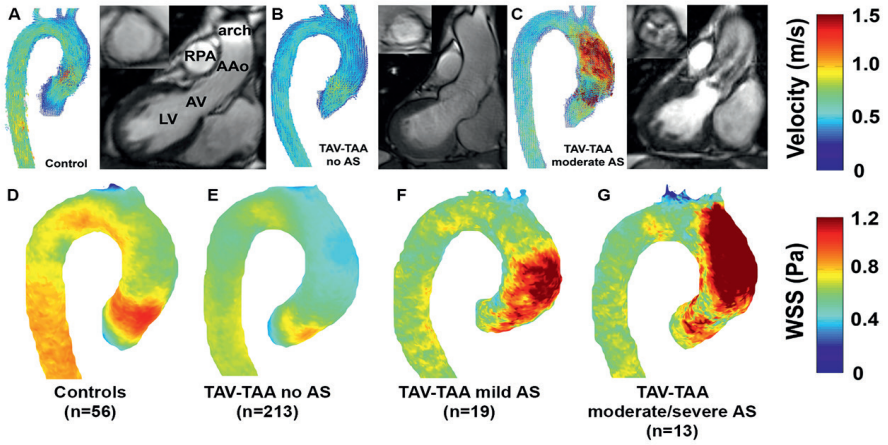

Figure 2.2: Exemplary 3D velocity vector visualizations and bSSFP images of the trifleaflet valve and the left ventricular outflow tract in **A)** a healthy control showing full opening of the valve, **B)** a patient with a trileaflet aortic valve (TAV) and a thoracic aortic aneurysm (TAA) – velocities are lower than in the control – and **C)** a patient with a stenosed trileaflet aortic valve showing high velocities. LV, left ventricle; AV, aortic valve; AAo, ascending aorta; RPA, right pulmonary artery. **D–G)** Cohort-averaging of WSS shows that WSS is lower for patients with TAV-TAA without AS, whereas WSS increases when AS severity increases. (Adapted from: van Ooij P, Markl M, Collins JD, et al. Aortic valve stenosis alters expression of regional aortic wall shear stress: New insights from a 4-dimensional flow magnetic resonance imaging study of 571 subjects. JAHA. 2017;6(9):e005959, with permission.)

2.3.2 Flow displacement

Flow displacement is a parameter used to quantify eccentricity of the flow jet in the ascending aorta. It is defined as the distance between the velocity-weighted center of the peak systolic flow jet and the ascending aorta luminal centerline (**Figure 2.3**). High degrees of flow displacement have been observed in patients with AS, BAV disease and after transcatheter aortic valve replacement (TAVR) (27–30). A study in 25 BAV patients has shown that typical displacements differ between various BAV morphologies and correspond with patterns of dilative aortopathy (31). Moreover, in this study flow displacement correlated with the aortic growth rate, making this parameter a potential risk marker in patients susceptible to valve-induced aortic dilatation.

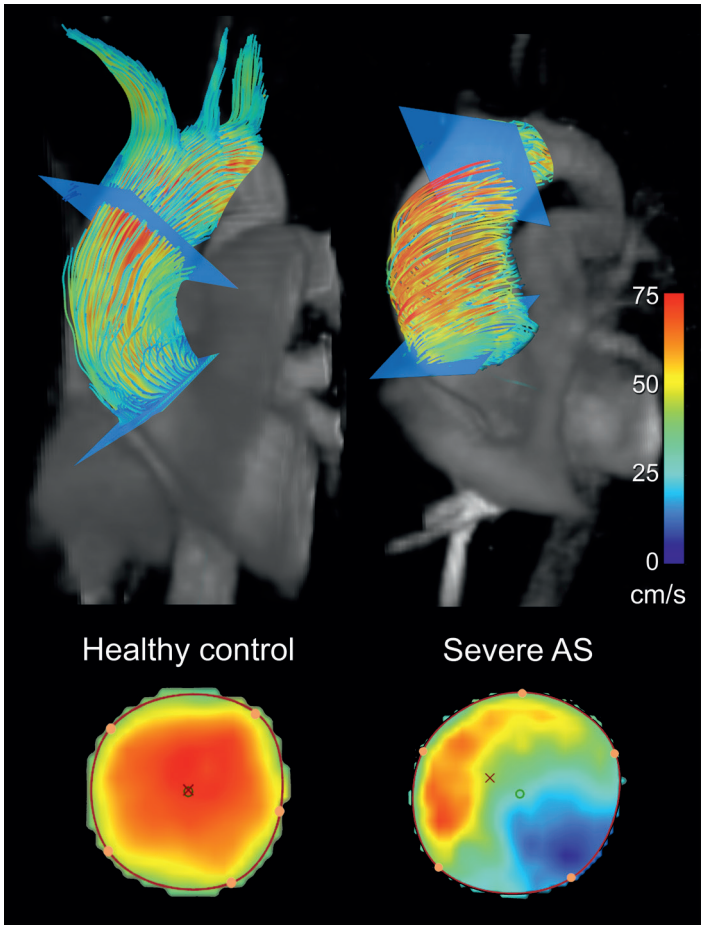

Figure 2.3: Differences in blood flow eccentricity between a 26-year-old healthy control (left) and a 21-year-old patient with severe AS accepted for surgical aortic valve replacement (right). Pathlines (top) show a more helical flow pattern for the AS patient than for the healthy control. Cross-sectional views of the velocities in the mid-ascending aorta (bottom) give insight into the flow displacement, which is defined by the distance between the center of the blood flow (indicated by the cross) and the centerline of the vessel (indicated by the circle) and is normalized to the lumen diameter.

2.3.3 Flow component analysis

Flow component analysis using particle tracing can provide insight into the efficiency of the cardiac cycle. Blood transiting the LV may follow different paths that can be specified by spatial origin and destination over the cardiac cycle, allowing for the definition of four components: 1) direct flow, i.e. blood entering and leaving the LV in the same cardiac cycle, 2) retained flow, i.e. blood that enters the LV but is not ejected during systole, 3) delayed ejected flow, i.e. blood that already resides in the LV before

diastole and is ejected during subsequent systole, and 4) residual volume, i.e. blood that already resides in the LV before diastole and stays there during systole (**Figure 2.4**) (32). These components can in turn be analyzed based on kinetic energy (KE). Flow component analysis (together with KE analysis) may in particular prove useful for the evaluation of complicated VHD phenotypes like low-flow low-gradient AS or combined VHD, as current clinical parameters do not always suffice in determining the severity and origin of these diseases (33).

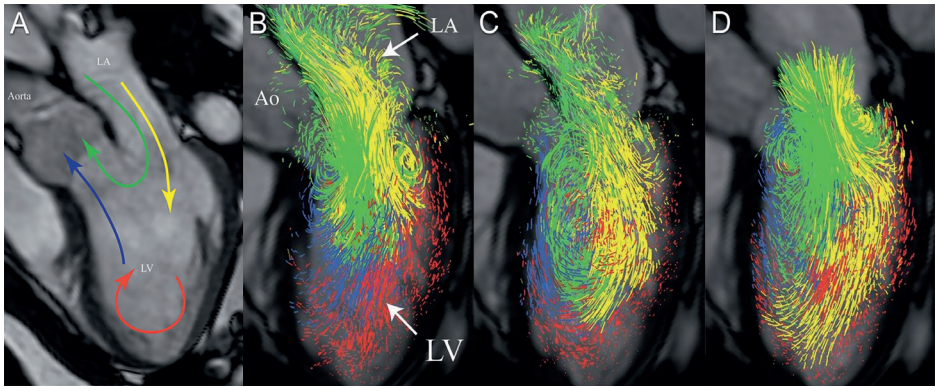

Figure 2.4: A) Illustration of the four functional components of LV blood flow: direct flow - green; retained flow - yellow; delayed ejected flow - blue; residual volume - red. **B–D)** Pathline visualizations of the four components in a healthy 50-year-old woman during **B)** early diastole, **C)** diastasis and **D)** atrial contraction. Ao, aorta; LV, left ventricle; LA, left atrium. (Adapted from: Eriksson J, Bolger AF, Ebbers T, Carlhäll CJ. Four-dimensional blood flow-specific markers of LV dysfunction in dilated cardiomyopathy. Eur Heart J Cardiovasc Imaging. 2013;14(5):417–24, by permission of Oxford University Press on behalf of the European Society of Cardiology.)

2.3.4 Vortical flow patterns

Passage of blood across the heart valves leads to a certain degree of flow disturbance, depending on valvular function. As a result, KE is converted into thermal energy in a process called viscous energy loss (34). Formation of vortices downstream of the heart valves minimizes this energy loss (35). Visual and quantitative evaluation of vortical flow by 4D flow MRI is particularly relevant for the assessment of diastolic LV inflow (36). Vortex formation during LV inflow is a natural phenomenon that is believed to be important for redirection of blood towards the LV outflow tract and thus for efficient cardiac function (37). A recent 4D flow MRI study in 32 patients who underwent atrioventricular septal defect (AVSD) repair revealed significant differences in vortex presence, position, shape and orientation compared to healthy

subjects, see **Figure 2.5** (38). Furthermore, vortex core shape and orientation were strongly related to valve shape and LV inflow direction.

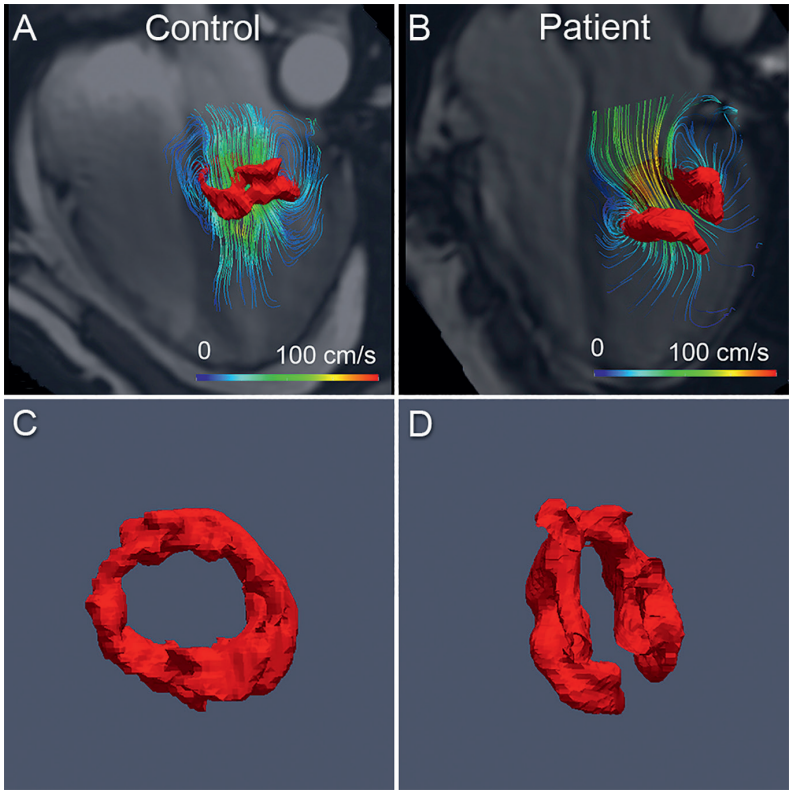

Figure 2.5: Different vortex core orientation and shape during early diastole in a patient with corrected atrioventricular septal defect (AVSD) **(A and C)** compared with a healthy control **(B and D)**. Streamline visualizations show a more lateral inflow direction in the patient **(B)** compared to the healthy control **(A)**. LA, left atrium; LV, left ventricle. (Adapted from: Calkoen EE, Westenberg JJ, Kroft LJ, et al. Characterization and quantification of dynamic eccentric regurgitation of the left atrioventricular valve after atrioventricular septal defect correction with 4D Flow cardiovascular magnetic resonance and retrospective valve tracking. J Cardiovasc Magn Reson. 2012;17:1–9, with permission.)

2.3.5 Turbulent kinetic energy

Whereas viscous energy loss is related to flow inefficiency in non-turbulent flow such as vortical and helical flow, turbulent kinetic energy (TKE) reflects flow inefficiency in regions of flow disturbance characterized by rapid velocity fluctuations in different directions, often referred to as turbulence (39,40). 4D flow MRI can be used to derive velocity distributions in individual voxels and subsequently calculate TKE and pressure

gradients. As heat dissipation is not accounted for in TKE calculations based on three-directional 4D flow MRI, Ha et al. propose the use a six-directional 4D flow encoding scheme to quantify TKE (41). They show that this method can robustly predict the irreversible pressure drop in a phantom stenosis model (41).

2.4 Application of 4D flow MRI to left-sided VHD

2.4.1 Aortic valve stenosis

Severe AS can lead to symptoms such as dyspnea, angina and syncope and is a major cause of morbidity and mortality worldwide (1). Grading of AS severity by MRI is typically based on peak blood flow velocity, to estimate the transvalvular pressure gradient, and/or AVA assessment using 2D PC-MRI (1,42). Echocardiographic estimation of pressure gradients has demonstrated systematic discrepancies between Doppler-based and catheter-based measurements (43). These discrepancies were assigned to pressure loss overestimation by Doppler echocardiography due to the pressure recovery phenomenon downstream of the aortic valve, and consequently overestimation of AS severity. 4D flow-derived estimation of transvalvular pressure gradients based on TKE has been proposed as a supplementary method in the evaluation of AS (44,45), as it allows for functional analysis of energy efficiency and cardiac workload which echocardiography does not offer. The clinical value of 4D flow-derived TKE is supported by good correlations between TKE values in the ascending aorta and post-stenotic pressure loss in AS patients (32,46). Furthermore, in AS patients with aortic dilatation, elevated 4D flow-derived viscous energy loss in both the ascending and thoracic aorta strongly correlated with the transvalvular pressure gradient as calculated with the modified Bernoulli equation (47,48). Another 4D flow study has focused on quantification of the effective orifice area (EOA) to determine AS severity, employing a method called jet shear layer detection (49). This method uses a mathematical approach to distinguish flow jets from recirculating flow to reveal a "shear layer" that represents the EOA border at the height of the vena contracta.

4D flow MRI may also aid in the assessment of VHD-induced aortic dilatation. Several 4D flow MRI studies show that the presence and severity of AS determine the extent of abnormal hemodynamics throughout the entire ascending aorta, giving rise to elevated WSS and subsequent extracellular matrix degradation and elastic fiber degeneration in the ascending aorta (26,50,51).

Treatment of severe AS consists of replacement of the stenotic valve through surgical aortic valve replacement (SAVR) or, predominantly in elderly or high-risk patients, transcatheter aortic valve replacement (TAVR) (42). Technical developments in both MR image acquisition and prosthetic valve designs have made MRI in patients with aortic valve prostheses possible, allowing for the evaluation of blood flow characteristics after AVR. 4D flow MRI studies focusing on the hemodynamic performance of prosthetic aortic valves have compared various biological aortic valves, mechanical aortic valves and transcatheter aortic valve implants (52,53). These studies show that after AVR, ascending aortic hemodynamics are different compared to native aortic valves and that blood flow velocities and WSS vary between different types of prostheses. Future 4D flow MRI studies are necessary to determine whether these differences between prostheses, such as differences in WSS patterns, have a prognostic value and may aid in patient-specific treatment selection.

2.4.2 Aortic valve regurgitation

AR is most often caused by BAV, infective endocarditis, or dilatation of the aortic root caused by connective tissue disease (1). Quantitative MRI assessment of AR consists of left ventricular volume assessment and aortic flow measurements. Treatment may consist of surgical aortic valve replacement, aortic valve repair or valve-sparing aortic root replacement. Timing of treatment is based on several factors, including LV ejection fraction (LVEF), LV diameters and the presence of symptoms. Several small studies have shown that MRI-derived regurgitant volume may provide important prognostic information in AR patients (54–56) and supersedes TTE-derived regurgitant volume in its association with outcome (54).

Research on the role of 4D flow MRI in patients with AR is limited. A study of 54 patients shows that visual, qualitative grading of AR is well possible with 4D flow MRI in patients with mild to moderate AR and leads to good agreement with TTE-based severity grading ($\kappa = 0.73$) (57). 4D flow MRI with valve tracking has also been used as a reference method for quantification of AR with 2D and 3D Doppler echocardiography. 2D Doppler echocardiography showed a moderate agreement with 4D flow MRI in qualitative severity grading ($\kappa = 0.53$), in part due to eccentric jets associated with weak correlation with 4D flow MRI-based quantification ($r = 0.66$, $p = 0.005$) (58). These results suggest that especially for eccentric jets and non-circular valve orifices, 4D flow MRI and 3D TTE can capture regurgitation better than 2D TTE because they are not limited by geometrical assumptions and suboptimal alignment with the flow

jet. Furthermore, 4D flow MRI studies using valve tracking in a study population of healthy subjects as well as AR patients demonstrated strong consistency between net flow volumes across all four heart valves (21,22).

2.4.3 Mitral valve regurgitation

MR is the most prevalent form of left-sided VHD. It can cause LV volume overload, which may lead to progressive dilatation of the left ventricle and left atrium, heart failure and pulmonary hypertension (6). Decisions regarding surgical interventions, being mitral valve repair or replacement, rely on symptomatology as well as the regurgitation severity, LVEF, and LV end-systolic diameter.

MRI has been proposed as an accurate and reproducible method for the quantification of MR and has been associated with more reproducible severity grading than echocardiography (59–61). Since direct 2D phase-contrast (PC) MRI over the mitral valve does not optimally account for annular motion and the valve's complex anatomy, quantification of regurgitant volume is typically performed in an indirect manner based on left ventricular (LV) stroke volume and aortic flow (62). A large multicenter study revealed a considerable discordance in categorical severity grading between MRI and echocardiography (61). Interestingly, in a subgroup of patients undergoing mitral valve surgery, MRI-based severity grading had superior prognostic value over echocardiography in predicting the degree of post-surgical LV remodeling. Also, recent large-scale studies found MRI-derived regurgitant volume to be a better predictor of referral for surgery and all-cause mortality than echocardiographic parameters (63,64). These findings may evoke changes in the diagnostic and prognostic workup of MR patients, causing MRI to gain ground in the clinical management of these patients.

4D flow MRI in combination with retrospective valve tracking enables accurate transmitral flow quantification. An early study demonstrated excellent correlation between net forward MV and tricuspid valve (TV) flow volumes ($r = 0.97$, $p < 0.01$) and good correlation with aortic valve (AV) forward flow volume ($r = 0.82$, $p < 0.01$ and $r = 0.74$, $p < 0.01$ for MV and TV, respectively) in 20 patients suspected of having mitral and/or tricuspid valve regurgitation (23). Excellent consistency between mitral and aortic valve flow ($r = 0.97$, $p < 0.001$) has been obtained even for complex regurgitant flow jets in MR patients who underwent atrioventricular septal defect (AVSD) correction (19). See **Figure 2.6** for an example of valve tracking in a patient with severe MR. Also, MR patients with eccentric regurgitation jets have demonstrated highly disturbed left

atrial flow patterns with elevated left atrial TKE levels which were, averaged over the cardiac cycle, closely related to net regurgitant volumes (65). Further characterization of left atrial flow in MR patients could render new insights into both accurate quantification of MR and the mechanisms driving disease progression.

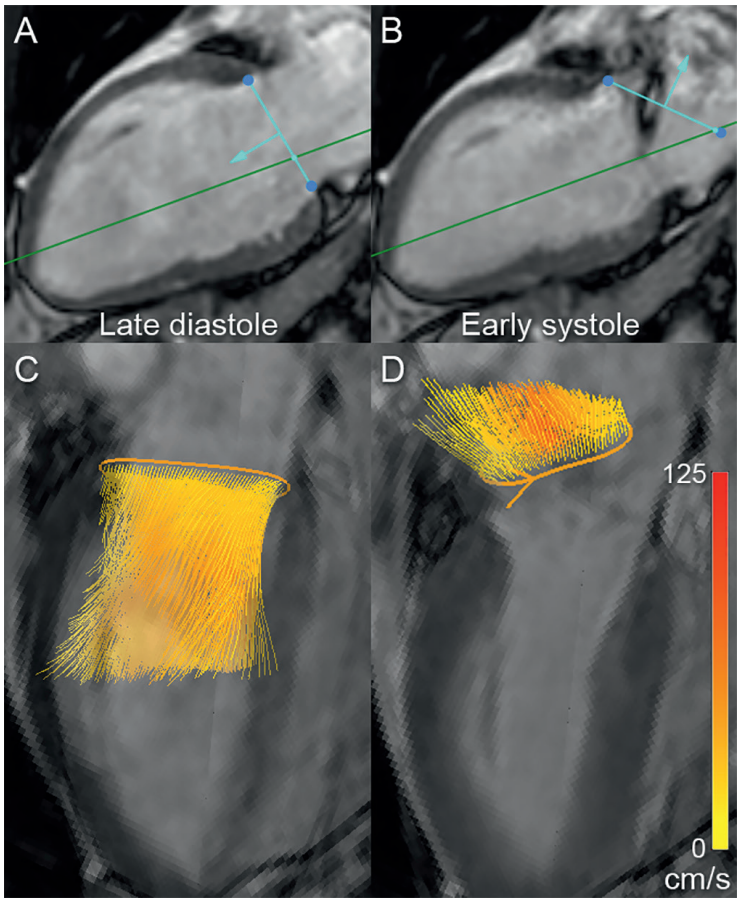

Figure 2.6: Retrospective valve tracking procedure on 4D flow MRI data with flow angulation for regurgitant flow in a patient with asymptomatic severe MI, as first diagnosed by echocardiography. **A)** The mitral valve is tracked on a two-chamber cine bSSFP image and four-chamber view (green line shows location of intersection). **B)** The quantification plane is angulated perpendicular to the regurgitation and shifted upward towards the vena contracta to minimize phase dispersion effects close to the valve. Corresponding time-resolved streamlines are shown in **C)** and **D)**. A regurgitation fraction of 44% was measured.

Retrospective studies with 4D flow MRI on surgical cohorts increasingly demonstrate the prognostic value of hemodynamic parameters. Al-Wakeel et al. studied the effect of MV repair on KE in patients with MR and found that MV repair resulted in normalization of systolic and early diastolic KE values, mainly due to reductions of blood volumes (66). The effect of MV repair on normal LV hemodynamics has been assessed with 4D flow MRI as well, using mitral annuloplasty rings of different sizes implanted in healthy sheep (67). Intraventricular flow patterns were shown to be disturbed after annuloplasty, with a significant relation between the size of the annuloplasty ring and the inflow angle, as well as peak-diastolic velocity.

2.5 Tissue characterization and myocardial function assessment by advanced MRI techniques

2.5.1 Tissue mapping

In patients with left-sided VHD, LV remodeling is an important marker of disease progression. It is often characterized by progressive myocardial fibrosis, resulting in LV systolic dysfunction (68). Tissue mapping is a novel MRI imaging modality, capable of visualizing and quantifying structural ability changes in the myocardium. Images are based on the MRI characteristics T1, T2 and T2*(star) of the myocardium and allow for quantification of both intracellular abnormalities (such as cytogenic edema, iron overload), extracellular abnormalities (such as vasogenic edema and fibrosis) or a combination of both (69).

2.5.1.1 T1-mapping and extracellular volume calculation

T1 values are a marker for myocardial fibrosis or tissue inflammation: important markers of disease progression in patients with left-sided VHD. In AS patients, mechanisms leading to myocardial fibrosis include diffuse ischemia in hypertrophic LV myocardium as a consequence of chronic pressure overload (70,71). In AR and MR, volume overload causes activation of the renin-angiotensin-aldosterone system, which activates profibrotic pathways in the myocardium (72,73). Myocardial fibrosis can be quantified through myocardial biopsy, but recent studies have shown that extracellular volume (ECV), a proxy of diffuse myocardial fibrosis, can be quantified using T1-mapping. This technique allows for measurement of native T1-values of the myocardium and gadolinium-enhanced T1-shortening: parameters that, after correction for hematocrit levels, can be used to quantify the amount of ECV

in the myocardial volume of interest. Various protocols have been proposed for the acquisition of T1-maps, such as the modified Look Locker inversion recovery (MOLLI) technique as described by Messroghli et al. (74). Although ECV mapping is traditionally performed using slow intravenous gadolinium infusion, several studies have shown that both simple bolus contrast administration and split dose contrast administration allow for myocardial ECV fraction measurements (75–77). These developments may accelerate the introduction of ECV mapping into routine clinical MRI protocols.

Wong et al. found, in an unselected cohort of patients undergoing cardiac MRI, that ECV is a strong predictor of mortality (78). Several studies in AS patients have shown that T1-values and the degree of myocardial fibrosis correlate with disease progression and mortality and that myocardial ECV is a strong predictor of cardiovascular complications (70,71,79–81) (**Figure 2.7**). Moreover, recent studies in AS patients indicate that T1-mapping may aid in the detection of cardiac amyloidosis, which can significantly influence the prognosis (82). Hence, T1-mapping can be useful in the diagnostic work-up and the prognostic evaluation of AS patients (82–85).

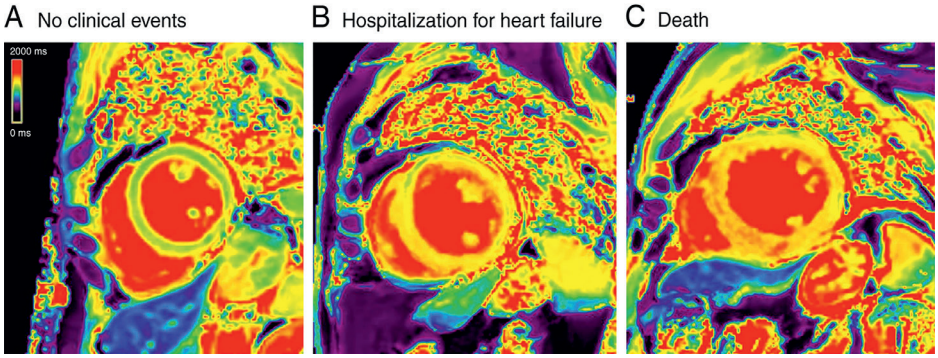

Figure 2.7: Color-coded native T1-weighted images of a mid-ventricular LV slice of **A)** a 63-year-old man with moderate AS who did not experience any clinical event, **B)** a 70-year-old man with severe AS who was hospitalized for decompensated heart failure, and **C)** a 65-year-old man with severe AS who died during follow-up. Native T1-values as measured in a septal region of interest were 1,163 ms, 1,257 ms and 1,358 ms, respectively. (Adapted from: Lee H, Park J-B, Yoon YE, et al. Noncontrast Myocardial T1 Mapping by Cardiac Magnetic Resonance Predicts Outcome in Patients With Aortic Stenosis. JACC Cardiovasc Imaging. 2017;1–10, with permission from Elsevier.)

T1-mapping has revealed differences in myocardial relaxation times between AR patients and normal hearts (86). Furthermore, increased ECV and diffuse fibrosis were found in patients with asymptomatic moderate to severe MR (86–89). Future T1- and ECV-mapping studies are required to investigate whether the finding of myocardial fibrosis in patients with left-sided VHD mandates early surgical intervention to prevent progressive and irreversible myocardial fibrosis. Finally, early studies in patients with BAV and hypertrophic cardiomyopathy show that the combination of 4D flow MRI with tissue mapping allows for comprehensive evaluation of flow and tissue abnormalities that may lead to LV remodeling (90,91).

2.5.2 Strain imaging

Strain imaging allows for dynamic assessment of LV function, reflecting the contractility of the myocardial wall. With MRI, strain can be measured longitudinally, circumferentially and radially using long-axis and short-axis cine images, typically by means of feature tracking over 16 myocardial segments as defined by the American Heart Association (AHA) model. An example is shown in **Figure 2.8**. This approach provides a simplified model of myocardial motion based on tracking of the myocardial borders and allows for quantification of global strain and strain rate – surrogates for diastolic function. In a large meta-analysis, global longitudinal strain (GLS), as assessed by echocardiography, has even shown to be more predictive for mortality than LVEF in patients with LV dysfunction (92). The potential of GLS has also been investigated specifically in VHD patients. A study comprising 233 patients with severe MR undergoing mitral valve repair identified impaired GLS as an independent predictor of LV dysfunction (LVEF < 50%) during long-term follow-up (93). These patients had a normal EF at the time of surgery and still developed LV dysfunction postoperatively, indicating that myocardial damage as a consequence of MR may occur before LV function deteriorates. Indeed, in a cohort of asymptomatic MR patients (n = 737) with preserved LVEF, abnormal baseline GLS was independently associated with long-term mortality (94). Moreover, impaired longitudinal and circumferential strain rates 6 months after MV repair have been associated with myofibrillar degeneration at the time of surgery (95,96), signifying the clinical value of impaired strain as an imaging biomarker of early myocardial dysfunction. Also for AR, long-term studies show that GLS is an independent predictor of mortality or indications for surgery (97–99). Outcome studies with similar results have been conducted in AS patients (100–102). In conclusion, future adoption of GLS evaluation into standard clinical practice may lead to improved surgical timing in patients with

VHD. However, the application of strain imaging for the assessment of LV function has so far not explicitly appeared in guidelines for the clinical management of VHD. Although most aforementioned strain studies employed echocardiographic methods, a recent comparison of echocardiographic speckle tracking with MRI-based feature tracking showed that MRI is a useful alternative to echocardiography for global strain analysis and more practicable due to better image quality (103).

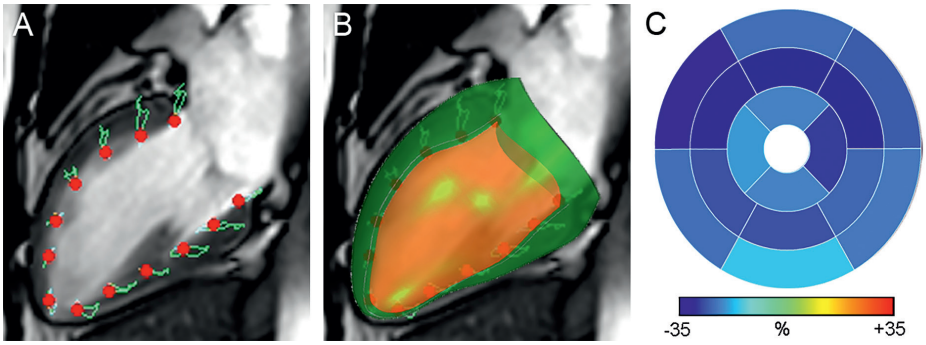

Figure 2.8: Longitudinal strain analysis of the left ventricle using feature tracking. Cardiac MRI images were obtained in a 59-year-old healthy person. **A)** Two-chamber cine bSSFP image with tracked points in red and time-resolved trajectories in green. **B)** Superimposed 3D model showing end-systolic (orange) and end-diastolic LV volume (green), obtained by combining feature tracking analyses in two-chamber, three-chamber and four-chamber view. **C)** AHA 16-segment model of longitudinal strain percentages.

2.6 Future perspectives and conclusion

This review demonstrates the potential of 4D flow MRI, tissue mapping and strain imaging for the diagnosis and quantitative assessment of left-sided VHD. Longitudinal studies on the natural course of AS, AR and MR as well as large-scale outcome studies on surgical patients are of great importance to prospectively investigate the relation between disease development and MRI-derived hemodynamic and tissue-characteristic parameters. Furthermore, research is ongoing to overcome various limitations. In 4D flow MRI, perhaps the largest challenge is to keep scan times low while reaching higher spatio-temporal resolutions in large volumes of interest. Also, post-processing is time consuming and user- and experience-dependent, delaying the implementation of these techniques into general clinical practice. Technical developments, such as acceleration of acquisition sequences using parallel imaging or k-t undersampling, may allow for more efficient data acquisition and analysis. To date, only few commercial 4D flow MRI

sequences and packages have been introduced to the market and most 4D flow studies and applications rely on protocols developed by individual research groups. The wide variety of used sequences and analysis software forms an obstacle for the development of 4D flow MRI to become a commonly employed clinical technique.

In tissue mapping, imaging studies have mainly been conducted in small cohorts and the accuracy of T1-values remains unclear. Although consensus-based recommendations for parametric mapping exist, histopathological validation of T1-mapping studies will have to clarify whether tissue mapping can be used for diagnostic and prognostic purposes (69). Strain imaging has not been performed as widely with MRI as with echocardiography, although it is feasible on routine MRI images and its prognostic value is supported by a large body of echocardiographic studies. Intervendor differences might however hamper the clinical implementation of strain imaging (104).

In conclusion, advanced cardiac MRI techniques provide valuable information that may guide clinical decision-making and surgical planning in patients with left-sided VHD. Future research should aim at exploring quantitative MRI to its full potential in the optimization and fine-tuning of clinical management in VHD. Employment of quantitative 4D flow MRI, multi-parametric mapping and strain quantification in combination with standard quantitative volumetry and qualitative imaging (such as contrast-enhanced MRA) ushers in a new era of increasingly accurate diagnosis, risk stratification, treatment selection and planning for best patient outcome.

2.7 References

1. Baumgartner H, Falk V, Bax JJ, et al. 2017 ESC/EACTS Guidelines for the management of valvular heart disease. Eur Heart J. 2017;38(36):2739–2786.
2. Chambers JB, Myerson SG, Rajani R, Morgan-Hughes GJ, Dweck MR. Multimodality imaging in heart valve disease. Open Hear. 2016;3(1):e000330.
3. Myerson SG. Heart valve disease: investigation by cardiovascular magnetic resonance. J Cardiovasc Magn Reson. 2012;14(1):7.
4. Nkomo VT, Gardin JM, Skelton TN, Gottdiener JS, Scott CG, Enriquez-Sarano M. Burden of valvular heart diseases: a population-based study. Lancet. 2006;368(9540):1005–1011.
5. Wollersheim LW, Li WW, De Mol BA. Current status of surgical treatment for aortic valve stenosis. J Card Surg. 2014;29(5):630–637.
6. Levine RA, Hagége AA, Judge DP, et al. Mitral valve disease-morphology and mechanisms. Nat Rev Cardiol. 2015;12(12):689–710.
7. Grothues F, Smith GC, Moon JC., et al. Comparison of interstudy reproducibility of cardiovascular magnetic resonance with two-dimensional echocardiography in normal subjects and in patients with heart failure or left ventricular hypertrophy. Am J Cardiol. 2002;90(1):29–34.
8. Allen BD, Syed AA, Bollache E, et al. Cardiovascular MRI in Thoracic Aortopathy: A Focused Review of Recent Literature Updates. Curr Radiol Rep. 2017;5(10):50.
9. Chitiboi T, Axel L. Magnetic resonance imaging of myocardial strain: A review of current approaches. J Magn Reson Imaging. 2017;46(5):1263–1280.
10. Zamorano JL, Fernández-Golfín C, González-Gómez A. Quantification of mitral regurgitation by echocardiography. Heart. 2015;101(2):146–154.
11. Chen CG, Thomas JD, Anconina J, et al. Impact of impinging wall jet on color Doppler quantification of mitral regurgitation. Circulation. 1991;84(2):712–720.
12. Sugeng L, Spencer KT, Mor-Avi V, et al. Dynamic Three-Dimensional Color Flow Doppler: An Improved Technique for the Assessment of Mitral Regurgitation. Echocardiography. 2003;20(3):265–273.
13. Thavendiranathan P, Phelan D, Thomas JD, Flamm SD, Marwick TH. Quantitative assessment of mitral regurgitation: Validation of new methods. J Am Coll Cardiol. 2012;60(16):1470–1483.
14. Zoghbi WA, Adams D, Bonow RO, et al. Recommendations for Noninvasive Evaluation of Native Valvular Regurgitation: A Report from the American Society of Echocardiography Developed in Collaboration with the Society for Cardiovascular Magnetic Resonance. J Am Soc Echocardiogr. 2017;30(4):303–371.
15. Elliott PM, Anastasakis A, Borger MA, et al. 2014 ESC Guidelines on diagnosis and management of hypertrophic cardiomyopathy. Eur Heart J. 2014;35(39):2733–2779.
16. Bellenger N, Burgess MI, Ray SG, et al. Comparison of left ventricular ejection fraction and volumes in heart failure by echocardiography, radionuclide ventriculography and cardiovascular magnetic resonance. Are they interchangeable? Eur Heart J. 2000;21(16):1387–1396.
17. Dyverfeldt P, Bissell M, Barker AJ, et al. 4D flow cardiovascular magnetic resonance consensus statement. J Cardiovasc Magn Reson. 2015;17(1):1–19.
18. Nordmeyer S, Riesenkampff E, Messroghli D, et al. Four-dimensional velocity-encoded magnetic resonance imaging improves blood flow quantification in patients with complex accelerated flow. J Magn Reson Imaging. 2013;37(1):208–216.
19. Calkoen EE, Westenberg JJ, Kroft LJ, et al. Characterization and quantification of dynamic eccentric regurgitation of the left atrioventricular valve after atrioventricular septal defect correction with 4D Flow cardiovascular magnetic resonance and retrospective valve tracking. J Cardiovasc Magn Reson. 2015;17(1):18.

20. Rose MJ, Jarvis K, Chowdhary V, et al. Efficient method for volumetric assessment of peak blood flow velocity using 4D flow MRI. J Magn Reson Imaging. 2016;44(6):1673–1682.
21. Roes SD, Hammer S, van der Geest RJ, et al. Flow assessment through four heart valves simultaneously using 3-dimensional 3-directional velocity-encoded magnetic resonance imaging with retrospective valve tracking in healthy volunteers and patients with valvular regurgitation. Invest Radiol. 2009;44(10):669–675.
22. Hsiao A, Tariq U, Alley MT, Lustig M, Vasanawala SS. Inlet and outlet valve flow and regurgitant volume may be directly and reliably quantified with accelerated, volumetric phase-contrast MRI. J Magn Reson Imaging. 2015;41(2):376–385.
23. Westenberg JJM, Roes SD, Ajmone Marsan N, et al. Mitral Valve and Tricuspid Valve Blood Flow: Accurate Quantification with 3D Velocity-encoded MR Imaging with Retrospective Valve Tracking. Radiology. 2008;249(3):792–800.
24. Lehoux S, Tedgui A. Cellular mechanics and gene expression in blood vessels. J Biomech. 2003;36(5):631–643.
25. van Ooij P, Potters W V., Collins J, et al. Characterization of Abnormal Wall Shear Stress Using 4D Flow MRI in Human Bicuspid Aortopathy. Ann Biomed Eng. 2015;43(6):1385–1397.
26. Guzzardi DG, Barker AJ, Van Ooij P, et al. Valve-Related Hemodynamics Mediate Human Bicuspid Aortopathy: Insights From Wall Shear Stress Mapping. J Am Coll Cardiol. 2015;66(8):892–900.
27. Sigovan M, Hope MD, Dyverfeldt P, Saloner D. Comparison of four-dimensional flow parameters for quantification of flow eccentricity in the ascending aorta. J Magn Reson Imaging. 2011;34(5):1226–1230.
28. Bissell MM, Hess AT, Biasiolli L, et al. Aortic dilation in bicuspid aortic valve disease: Flow pattern is a major contributor and differs with valve fusion type. Circ Cardiovasc Imaging. 2013;6(4):499–507.
29. Hope MD, Dyverfeldt P, Acevedo-Bolton G, et al. Post-stenotic dilation: Evaluation of ascending aortic dilation with 4D flow MR imaging. Int J Cardiol. 2012;156(2):e40–e42.
30. Markl M, Mikati I, Carr J, McCarthy P, Malaisrie SC. Three-dimensional blood flow alterations after transcatheter aortic valve implantation. Circulation. 2012;125(15):573–576.
31. Hope MD, Sigovan M, Wrenn SJ, Saloner D, Dyverfeldt P. MRI hemodynamic markers of progressive bicuspid aortic valve-related aortic disease. J Magn Reson Imaging. 2014;40(1):140–145.
32. Eriksson J, Carlhäll C, Dyverfeldt P, Engvall J, Bolger AF, Ebbers T. Semi-automatic quantification of 4D left ventricular blood flow. J Cardiovasc Magn Reson. 2010;12(1):9.
33. Pibarot P, Dumesnil JG. Low-flow, low-gradient aortic stenosis with normal and depressed left ventricular ejection fraction. J Am Coll Cardiol. 2012;60(19):1845–1853.
34. Akins CW, Travis B, Yoganathan AP. Energy loss for evaluating heart valve performance. J Thorac Cardiovasc Surg. 2008;136(4):820–833.
35. Pedrizzetti G, Domenichini F. Nature optimizes the swirling flow in the human left ventricle. Phys Rev Lett. 2005;95(10):1–4.
36. Division C, Töger J, Kanski M, et al. Vortex Ring Formation in the Left Ventricle of the Heart: Analysis by 4D Flow MRI and Lagrangian Coherent Structures. Ann Biomed Eng. 2012;40(12):2652–2662.
37. Kilner PJ, Yang G-Z, Wilkes AJ, Mohiaddin RH, Firmin DN, Yacoub MH. Asymmetric redirection of flow through the heart. Nature. 2000;404(6779):759–761.
38. Calkoen EE, Elbaz MSMM, Westenberg JJMM, et al. Altered left ventricular vortex ring formation by 4-dimensional flow magnetic resonance imaging after repair of atrioventricular septal defects. J Thorac Cardiovasc Surg. 2015;150(5):1233–1240.
39. Dyverfeldt P, Sigfridsson A, Kvitting JPE, Ebbers T. Quantification of intravoxel velocity standard deviation and turbulence intensity by generalizing phase-contrast MRI. Magn Reson Med. 2006;56(4):850–858.

40. Dyverfeldt P, Kvitting JPE, Sigfridsson A, et al. Assessment of fluctuating velocities in disturbed cardiovascular blood flow: In vivo feasibility of generalized phase-contrast MRI. J Magn Reson Imaging. 2008;28(3):655–663.
41. Ha H, Lantz J, Ziegler M, et al. Estimating the irreversible pressure drop across a stenosis by quantifying turbulence production using 4D Flow MRI. Sci Rep. 2017;7(1):46618.
42. Nishimura RA, Otto CM, Bonow RO, et al. 2014 AHA/ACC guideline for the management of patients with valvular heart disease: A report of the American college of cardiology/American heart association task force on practice guidelines. J Am Coll Cardiol. 2014;63(22):e57–e185.
43. Garcia D, Ng E, Dumesnil JG, et al. Discrepancies between catheter and doppler estimates of valve effective orifice area can be predicted from the pressure recovery phenomenon: Practical implications with regard to quantification of aortic stenosis severity. J Am Coll Cardiol. 2003;41(3):435–442.
44. Binter C, Gotschy A, Sündermann SH, et al. Turbulent Kinetic Energy Assessed by Multipoint 4-Dimensional Flow Magnetic Resonance Imaging Provides Additional Information Relative to Echocardiography for the Determination of Aortic Stenosis Severity. Circ Cardiovasc Imaging. 2017;10(6):e005486.
45. Ha H, Kim GB, Kweon J, et al. Turbulent Kinetic Energy Measurement Using Phase Contrast MRI for Estimating the Post-Stenotic Pressure Drop: In Vitro Validation and Clinical Application. del Alamo JC, editor. PLoS One. 2016;11(3):1–14.
46. Dyverfeldt P, Hope MD, Tseng EE, Saloner D. Magnetic resonance measurement of turbulent kinetic energy for the estimation of irreversible pressure loss in aortic stenosis. JACC Cardiovasc Imaging. 2013;6(1):64–71.
47. Barker AJ, van Ooij P, Bandi K, et al. Viscous energy loss in the presence of abnormal aortic flow. Magn Reson Med. 2014;72(3):620–628.
48. Garcia D, Pibarot P, Dumesnil JG, Sakr F, Durand L-G. Assessment of Aortic Valve Stenosis Severity : A New Index Based on the Energy Loss Concept. Circulation. 2000;101(7):765–771.
49. Garcia J, Markl M, Schnell S, et al. Evaluation of aortic stenosis severity using 4D flow jet shear layer detection for the measurement of valve effective orifice area. Magn Reson Imaging. 2014;32(7):891–898.
50. van Ooij P, Markl M, Collins JD, et al. Aortic valve stenosis alters expression of regional aortic wall shear stress: New insights from a 4-dimensional flow magnetic resonance imaging study of 571 subjects. J Am Heart Assoc. 2017;6(9):1–14.
51. von Knobelsdorff-Brenkenhoff F, Karunaharamoorthy A, Trauzeddel RF, et al. Evaluation of Aortic Blood Flow and Wall Shear Stress in Aortic Stenosis and Its Association With Left Ventricular Remodeling. Circ Cardiovasc Imaging. 2016;9(3):e004038.
52. van Kesteren F, Wollersheim LW, Baan J, et al. Four-dimensional flow MRI of stented versus stentless aortic valve bioprostheses. Eur Radiol. 2018;28(1):257–264.
53. von Knobelsdorff-Brenkenhoff F, Trauzeddel RF, Barker AJ, Gruettner H, Markl M, Schulz-Menger J. Blood flow characteristics in the ascending aorta after aortic valve replacement—a pilot study using 4D-flow MRI. Int J Cardiol. 2014;170(3):426–433.
54. Harris AW, Krieger E V, Kim M, et al. Cardiac Magnetic Resonance Imaging Versus Transthoracic Echocardiography for Prediction of Outcomes in Chronic Aortic or Mitral Regurgitation. Am J Cardiol. 2017;119(7):1074–1081.
55. Myerson SG, d'Arcy J, Mohiaddin R, et al. Aortic regurgitation quantification using cardiovascular magnetic resonance: association with clinical outcome. Circulation. 2012;126(12):1452–1460.
56. Ribeiro HB, Orwat S, Hayek SS, et al. Cardiovascular Magnetic Resonance to Evaluate Aortic Regurgitation After Transcatheter Aortic Valve Replacement. J Am Coll Cardiol. 2016;68(6):577–585.

57. Chelu RG, van den Bosch AE, van Kranenburg M, et al. Qualitative grading of aortic regurgitation: a pilot study comparing CMR 4D flow and echocardiography. Int J Cardiovasc Imaging. 2016;32(2):301–307.
58. Ewe SH, Delgado V, Geest R Van Der, et al. Accuracy of three-dimensional versus two-dimensional echocardiography for quantification of aortic regurgitation and validation by three-dimensional three-directional velocity-encoded magnetic resonance imaging. Am J Cardiol. 2013;112(4):560–566.
59. Uretsky S, Argulian E, Narula J, Wolff SD. Use of Cardiac Magnetic Resonance Imaging in Assessing Mitral Regurgitation. J Am Coll Cardiol. 2018;71(5):547–563.
60. Biner S, Rafique A, Rafii F, et al. Reproducibility of proximal isovelocity surface area, vena contracta, and regurgitant jet area for assessment of mitral regurgitation severity. JACC Cardiovasc Imaging. 2010;3(3):235–243.
61. Uretsky S, Gillam L, Lang R, et al. Discordance between echocardiography and MRI in the assessment of mitral regurgitation severity: a prospective multicenter trial. J Am Coll Cardiol. 2015;65(11):1078–1088.
62. Fujita N, Chazouilleres AF, Hartiala JJ, et al. Quantification of mitral regurgitation by velocity-encoded cine nuclear magnetic resonance imaging. J Am Coll Cardiol. 1994;23(4):951–958.
63. Myerson SG, D'Arcy J, Christiansen JP, et al. Determination of Clinical Outcome in Mitral Regurgitation With Cardiovascular Magnetic Resonance Quantification. Circulation. 2016;133(23):2287–2296.
64. Penicka M, Vecera J, Mirica DC, Kotrc M, Kockova R, Van Camp G. Prognostic Implications of Magnetic Resonance-Derived Quantification in Asymptomatic Patients With Organic Mitral Regurgitation: Comparison With Doppler Echocardiography-Derived Integrative Approach. Circulation. 2017;137(13):1349–1360.
65. Dyverfeldt P, Kvitting J-PE, Carlhäll CJ, et al. Hemodynamic aspects of mitral regurgitation assessed by generalized phase-contrast MRI. J Magn Reson Imaging. 2011;33(3):582–588.
66. Al-Wakeel N, Fernandes JF, Amiri A, et al. Hemodynamic and energetic aspects of the left ventricle in patients with mitral regurgitation before and after mitral valve surgery. J Magn Reson Imaging. 2015;42(6):1705–1712.
67. Witschey WRTT, Zhang D, Contijoch F, et al. The Influence of Mitral Annuloplasty on Left Ventricular Flow Dynamics. Ann Thorac Surg. 2015;100(1):114–121.
68. Podlesnikar T, Delgado V, Bax JJ. Cardiovascular magnetic resonance imaging to assess myocardial fibrosis in valvular heart disease. Int J Cardiovasc Imaging. 2018;34(1):97–112.
69. Messroghli DR, Moon JC, Ferreira VM, et al. Clinical recommendations for cardiovascular magnetic resonance mapping of T1, T2, T2* and extracellular volume: A consensus statement by the Society for Cardiovascular Magnetic Resonance (SCMR) endorsed by the European Association for Cardiovascular Im. J Cardiovasc Magn Reson. 2017;19(1):75.
70. Azevedo CF, Nigri M, Higuchi ML, et al. Prognostic Significance of Myocardial Fibrosis Quantification by Histopathology and Magnetic Resonance Imaging in Patients With Severe Aortic Valve Disease. J Am Coll Cardiol. 2010;56(4):278–287.
71. Lee H, Park J-B, Yoon YE, et al. Noncontrast Myocardial T1 Mapping by Cardiac Magnetic Resonance Predicts Outcome in Patients With Aortic Stenosis. JACC Cardiovasc Imaging. 2018;11(7):974–983.
72. Gaasch WH, Aurigemma GP. Inhibition of the renin-angiotensin system and the left ventricular adaptation to mitral regurgitation. J Am Coll Cardiol. 2002;39(8):1380–1383.
73. Perazella MA, Setaro JF. Renin-angiotensin-aldosterone system: Fundamental aspects and clinical implications in renal and cardiovascular disorders. J Nucl Cardiol. 2003;10(2):184–196.
74. Messroghli DR, Radjenovic A, Kozerke S, Higgins DM, Sivananthan MU, Ridgway JP. Modified Look-Locker inversion recovery (MOLLI) for high-resolution T1 mapping of the heart. Magn Reson Med. 2004;52(1):141–146.

75. McDiarmid AK, Swoboda PP, Erhayiem B, et al. Single bolus versus split dose gadolinium administration in extra-cellular volume calculation at 3 Tesla. J Cardiovasc Magn Reson. 2015;17(1):6.
76. Schelbert EB, Testa SM, Meier CG, et al. Myocardial extravascular extracellular volume fraction measurement by gadolinium cardiovascular magnetic resonance in humans: slow infusion versus bolus. J Cardiovasc Magn Reson. 2011;13(1):16.
77. White SK, Sado DM, Fontana M, et al. T1 Mapping for Myocardial Extracellular Volume Measurement by CMR. JACC Cardiovasc Imaging. 2013;6(9):955–962.
78. Wong TC, Piehler K, Meier CG, et al. Association between extracellular matrix expansion quantified by cardiovascular magnetic resonance and short-term mortality. Circulation. 2012;126(10):1206–1216.
79. Milano AD, Faggian G, Dodonov M, et al. Prognostic value of myocardial fibrosis in patients with severe aortic valve stenosis. J Thorac Cardiovasc Surg. 2012;144(4):830–837.
80. Dweck MR, Joshi S, Murigu T, et al. Midwall fibrosis is an independent predictor of mortality in patients with aortic stenosis. J Am Coll Cardiol. 2011;58(12):1271–1279.
81. Mewton N, Liu CY, Croisille P, Bluemke D, Lima JAC. Assessment of myocardial fibrosis with cardiovascular magnetic resonance. J Am Coll Cardiol. 2011;57(8):891–903.
82. Cavalcante JL, Rijal S, Abdelkarim I, et al. Cardiac amyloidosis is prevalent in older patients with aortic stenosis and carries worse prognosis. J Cardiovasc Magn Reson. 2017;19(1):98.
83. Lee S-P, Lee W, Lee JM, et al. Assessment of diffuse myocardial fibrosis by using MR imaging in asymptomatic patients with aortic stenosis. Radiology. 2015;274(2):359–369.
84. Sado DM, White SK, Piechnik SK, et al. Identification and assessment of Anderson-Fabry disease by cardiovascular magnetic resonance noncontrast myocardial T1 mapping. Circ Cardiovasc Imaging. 2013;6(3):392–398.
85. Bull S, White SK, Piechnik SK, et al. Human non-contrast T1 values and correlation with histology in diffuse fibrosis. Heart. 2013;99(13):932–937.
86. Sparrow P, Messroghli DR, Reid S, Ridgway JP, Bainbridge G, Sivananthan MU. Myocardial T1 Mapping for Detection of Left Ventricular Myocardial Fibrosis in Chronic Aortic Regurgitation: Pilot Study. Am J Roentgenol. 2006;187(6):W630–W635.
87. Edwards NC, Moody WE, Yuan M, et al. Quantification of left ventricular interstitial fibrosis in asymptomatic chronic primary degenerative mitral regurgitation. Circ Cardiovasc Imaging. 2014;7(6):946–953.
88. Van De Heyning CM, Magne J, Piérard LA, et al. Late gadolinium enhancement CMR in primary mitral regurgitation. Eur J Clin Invest. 2014;44(9):840–847.
89. Flett AS, Sado DM, Quarta G, et al. Diffuse myocardial fibrosis in severe aortic stenosis: an equilibrium contrast cardiovascular magnetic resonance study. Eur Heart J Cardiovasc Imaging. 2012;13(10):819–826.
90. Geiger J, Rahsepar AA, Suwa K, et al. 4D flow MRI, cardiac function, and T1-mapping: Association of valve-mediated changes in aortic hemodynamics with left ventricular remodeling. J Magn Reson Imaging. 2018;48(1):121–131.
91. Van Ooij P, Allen BD, Contaldi C, et al. 4D flow MRI and T1-Mapping: Assessment of altered cardiac hemodynamics and extracellular volume fraction in hypertrophic cardiomyopathy. J Magn Reson Imaging. 2016;43(1):107–114.
92. Kalam K, Otahal P, Marwick TH. Prognostic implications of global LV dysfunction: a systematic review and meta-analysis of global longitudinal strain and ejection fraction. Heart. 2014;100(21):1673–1680.
93. Witkowski TG, Thomas JD, Debonnaire PJMR, et al. Global longitudinal strain predicts left ventricular dysfunction after mitral valve repair. Eur Heart J Cardiovasc Imaging. 2013;14(1):69–76.

94. Mentias A, Naji P, Gillinov M, et al. Baseline LV strain independently predicts exercise capacity in asymptomatic primary mitral regurgitation patients and preserved LV ejection fraction undergoing rest-stress echocardiography. Eur Heart J. 2016;37(18):1238–1239.
95. Ahmed MI, Gladden JD, Litovsky SH, et al. Increased oxidative stress and cardiomyocyte myofibrillar degeneration in patients with chronic isolated mitral regurgitation and ejection fraction >60%. J Am Coll Cardiol. 2010;55(7):671–679.
96. Schiros CG, Dell'Italia LJ, Gladden JD, et al. Magnetic resonance imaging with 3-dimensional analysis of left ventricular remodeling in isolated mitral regurgitation: Implications beyond dimensions. Circulation. 2012;125(19):2334–2342.
97. Ewe SH, Haeck MLA, Ng ACT, et al. Detection of subtle left ventricular systolic dysfunction in patients with significant aortic regurgitation and preserved left ventricular ejection fraction: speckle tracking echocardiographic analysis. Eur Hear J - Cardiovasc Imaging. 2015;16(9):992–999.
98. Park SHSM, Yang YA, Kim KY, et al. Left ventricular strain as predictor of chronic aortic regurgitation. J Cardiovasc Ultrasound. 2015;23(2):78–85.
99. Di Salvo G, Rea A, Mormile A, et al. Usefulness of bidimensional strain imaging for predicting outcome in asymptomatic patients aged ≤ 16 years with isolated moderate to severe aortic regurgitation. Am J Cardiol. 2012;110(7):1051–1055.
100. Kearney LG, Lu K, Ord M, et al. Global longitudinal strain is a strong independent predictor of all-cause mortality in patients with aortic stenosis. Eur Heart J Cardiovasc Imaging. 2012;13(10):827–833.
101. Yingchoncharoen T, Gibby C, Rodriguez LL, Grimm RA, Marwick TH. Association of myocardial deformation with outcome in asymptomatic aortic stenosis with normal ejection fraction. Circ Cardiovasc Imaging. 2012;5(6):719–725.
102. Dahl JS, Videbæk L, Poulsen MK, Rudbæk TR, Pellikka PA, Maller JE. Global strain in severe aortic valve stenosis relation to clinical outcome after aortic valve replacement. Circ Cardiovasc Imaging. 2012;5(5):613–620.
103. Obokata M, Nagata Y, Wu VCC, et al. Direct comparison of cardiacmagnetic resonance feature tracking and 2D/3D echocardiography speckle tracking for evaluation of global left ventricular strain. Eur Heart J Cardiovasc Imaging. 2016;17(5):525–532.
104. Schuster A, Stahnke VC, Unterberg-Buchwald C, et al. Cardiovascular magnetic resonance feature-tracking assessment of myocardial mechanics: Intervendor agreement and considerations regarding reproducibility. Clin Radiol. 2015;70(9):989–998.

Quantification of Mitral Valve Regurgitation from 4D Flow MRI using Semi-Automated Flow Tracking

3

Carmen P.S. Blanken
Jos J.M. Westenberg
Jean-Paul Aben
Geertruida P. Bijvoet
Steven A.J. Chamuleau
S. Matthijs Boekholdt
Aart J. Nederveen
Tim Leiner
Pim van Ooij
R. Nils Planken

Radiol. Cardiothorac. Imaging 2020; 2(5): e200004.

Abstract

Background

Cardiac 4D flow MRI can potentially be used to improve clinical triage of patients with mitral valve regurgitation (MR). Retrospective valve tracking enables quantification of forward blood flow over the heart valves. For accurate quantification of absolute regurgitant volume (Rvol), semi-automated flow tracking has been suggested.

Purpose

To compare the accuracy of semi-automated flow tracking with that of semi-automated valve tracking for quantification of MR from clinical 4D flow MRI data obtained in patients with mild, moderate, and severe MR.

Methods

4D flow MRI data were retrospectively collected from 30 patients (21 men, 61 ± 10 years) who underwent 4D flow MRI between 2006 and 2016. Ten had mild MR, 9 had moderate MR and 11 had severe MR, as diagnosed by semi-quantitative echocardiography. Rvol across the mitral valve (MV) was quantified using three methods: indirect quantification ($Rvol_{INDIRECT}$), valve tracking ($Rvol_{VALVE}$) and flow tracking ($Rvol_{FLOW}$). A second observer repeated the measurements. Aortic valve (AV) flow was quantified as well, to test for intervalve consistency. Wilcoxon's signed-rank test, orthogonal regression, Bland–Altman analysis and coefficients of variation (CV) were used to assess agreement among measurements and between observers.

Results

$Rvol_{FLOW}$ was higher (24.8 ml, interquartile range [IQR] 14.3–45.7 ml) than $Rvol_{VALVE}$ (9.9 ml, IQR 6.0–16.9 ml, $p < 0.001$). Both $Rvol_{FLOW}$ and $Rvol_{VALVE}$ differed significantly from $Rvol_{INDIRECT}$ (19.1 ml, IQR 4.1–47.5 ml, $p = 0.03$). $Rvol_{FLOW}$ agreed better with $Rvol_{INDIRECT}$ ($\hat{y} = 0.78x + 12$, $r = 0.88$) than $Rvol_{VALVE}$ ($\hat{y} = 0.16x + 8.1$, $r = 0.53$). Bland–Altman analysis revealed underestimation of $Rvol_{VALVE}$ in severe MR. Interobserver agreement was excellent for $Rvol_{FLOW}$ ($r = 0.95$, CV = 27%) and moderate for $Rvol_{VALVE}$ ($r = 0.72$, CV = 57%). Orthogonal regression demonstrated better intervalve consistency for flow tracking ($\hat{y} = 1.2x - 13.4$, $r = 0.82$) than for valve tracking ($\hat{y} = 2.7x - 92.4$, $r = 0.67$).

Conclusion

Flow tracking provides more accurate 4D flow MRI-derived MR quantification than valve tracking in terms of agreement with indirect quantification and intervalve consistency, particularly in severe MR.

3.1 Introduction

Therapeutic decision-making in patients with mitral valve regurgitation (MR) is predominantly based on symptomatology and MR severity. Transthoracic echocardiography (TTE) is the method of choice for assessment of MR severity, and is based on an integrated approach using a broad spectrum of measures, including valve morphology, regurgitant jet characteristics, an estimate of the regurgitant volume (Rvol) using the proximal isovelocity surface area (PISA) method, vena contracta width, pulmonary vein systolic flow reversal and left ventricular (LV) dimensions (1,2). For patients in whom TTE examinations are unreliable due to poor acoustic windows or poor alignment of the transducer beam with the regurgitant jet, cardiac magnetic resonance imaging (MRI) is recommended for the diagnostic and prognostic assessment of MR (2,3). Furthermore, a growing body of literature suggests that MRI could improve diagnosis and surgical timing in MR patients compared to TTE (4–6). MRI is more accurate and reproducible than echocardiography in the assessment of ventricular volumes and flow across the heart valves (7,8). Although quantification of Rvol is possible with echocardiography, it has been associated with poor to moderate inter- and intra-observer agreements (4,9). Cardiac MRI-derived Rvol is associated with high interobserver agreement and is an independent predictor of the future need for surgery and post-surgical LV remodeling, with more predictive power than echocardiographic assessment (4,5). Moreover, in a cohort of 258 asymptomatic patients with moderate to severe primary MR who received treatment based on echocardiography, quantification of Rvol by MRI resulted in reclassification of 24% of patients and led to better prognostic assessment in terms of indication for mitral valve (MV) surgery, or death (6).

The current state-of-the-art MRI method to quantify MR makes use of two different acquisition techniques: two-dimensional phase-contrast MRI (2D flow MRI) across the aortic valve (AV) and short-axis cine MRI (balanced steady state free precession, bSSFP) of the left ventricle (LV). Combined, these acquisitions allow for calculation of Rvol across the MV, by subtracting the AV forward flow volume (as measured by 2D flow MRI) from the left ventricular stroke volume (LVSV, as measured by bSSFP). This indirect method is required because the MV has a high degree of annular motion which is not accounted for using 2D flow MRI in a fixed slice across the MV.

With the advent of 4D flow MRI, it has become possible to quantify three-directional blood flow in three dimensions over time and thus, to perform flow quantification during post-processing, using measurement planes that follow the motion of the heart valves. This technique is also known as retrospective valve tracking (10). 4D flow MRI in combination with retrospective valve tracking has been shown to provide accurate blood flow measurements across all four heart valves (11,12). Quantification of MR at the level of the valve is challenging however, since regurgitant flow is characterized by high blood velocity, turbulence and incoherent flow at the valvular level resulting in higher orders of motion. In such regions, protons within the same acquired voxel can have different velocities canceling out the composite signal (intravoxel phase dispersion), which in turn leads to signal loss and an underestimation of Rvol (13–16). A suggested solution is to measure in the left atrium at a distance of 1–2 cm from the regurgitant orifice, and perpendicular to the regurgitant jet, an approach called flow tracking (17,18). Thus far, this type of analysis has only been performed in patients with mild or moderate MR, and not in severe MR patients. Also, it is not known to what extent flow tracking can improve measurement accuracy compared to valve tracking analysis. The purpose of this study was to compare semi-automated flow tracking with semi-automated valve tracking for quantification of Rvol from clinical 4D flow MRI data obtained in a group of patients with mild, moderate, and severe MR. We hypothesized that semi-automated flow tracking is more accurate than semi-automated valve tracking for measurement of Rvol across the MV. A secondary objective was to compare 4D flow MRI-based severity classification with echocardiography-based classification of mild, moderate and severe MR.

3.2 Materials and methods

CAAS MR Solutions software was provided by Pie Medical Imaging BV, Maastricht, The Netherlands. Data inclusion and analysis was controlled by authors not employed by Pie Medical Imaging BV.

3.2.1 Study population

Thirty-four patients with MR as diagnosed by echocardiography who underwent cardiothoracic MRI including 4D flow MRI for assessment of MR were retrospectively selected from local research databases in a consecutive manner (Leiden UMC and UMC Utrecht, the Netherlands; examinations acquired between 2006 and 2016),

making sure that the data also contained cine bSSFP MRI (two-chamber, three-chamber, four-chamber, coronal aorta view and short-axis stack) and 2D flow MRI in the ascending aorta. Further inclusion criteria were data set compatibility with the post-processing software, a sufficiently large field of view to perform flow tracking, the absence of severe velocity aliasing in the 4D flow MRI data and the absence of shunt flow, since net flow volume differences between the MV and AV would invalidate intervalve consistency tests. Three data sets were excluded because of insufficient field of view coverage and one data set was excluded because of severe velocity aliasing. Thirty patients were included (21 male, 9 female, aged 61 ± 10 years). Sample size was determined based on prior knowledge of the number of available severe MR data sets (n = 11), making sure that mild, moderate and severe MR groups were approximately equal in size. The patients imaged at Leiden UMC had secondary mild (n = 10) or moderate MR (n = 9) and cardiomyopathy. Patients imaged at UMC Utrecht had asymptomatic primary severe MR (n = 11). Mild and moderate MR patients had previously been included in research studies on the application of manual and semi-automated valve tracking in patients with various heart diseases (11,19). However, those studies did not include severe MR patients nor did they investigate the diagnostic performance of semi-automated flow tracking.

Severity grading was based on semi-quantitative echocardiographic examinations with scores for abnormal valve morphology, visually assessed regurgitant jet characteristics, vena contracta width, the presence of pulmonary vein systolic flow reversal, and left ventricular dimensions (20). Echocardiographic scoring of severe MR patients was also performed using a recently proposed scoring index (21) by three cardiologists (S.M.B., S.A.J.C. and G.P.B., with 10, 12 and 2 years of experience in TTE and TEE, respectively). The cardiologists unanimously confirmed the presence of severe MR. Institutional medical ethical approval was obtained for the study, and all patients provided written informed consent.

3.2.2 Data acquisition

MRI scans were acquired on 1.5T MRI systems (Intera and Ingenia, Philips Healthcare, Best, the Netherlands). 2D cine bSSFP was performed at a spatial resolution of 1.25x1.25x8.00 mm^3 to 1.56x1.56x10.00 mm^3 and in 30 cardiac phases. 2D flow MRI measurements were performed at the level of the mid-ascending aorta at a spatial resolution of 1.25x1.25x8.00 mm^2 to 1.37x1.37x8.00 mm^2. The number of cardiac phases was 20 for the severe MR group and 40 for the mild and moderate MR group,

due to a difference in cardiac MRI protocols between the hospitals. Both acquisitions were ECG-gated and performed in breathholds. Mild and moderate MR patients received MRI and echocardiography on the same day. Severe MR patients received the exams several days or weeks apart (20 days, IQR 5–81 days).

4D flow MRI was performed using retrospective ECG gating and during free breathing, with a three-directional VENC of 150–280 cm/s, echo time/repetition time of 3.3/14 to 4.5/8.3 ms and a flip angle of 10°. For acceleration, echo planar imaging (EPI) was used with a factor of 5 and a SENSE factor of 2 (10). Acquired spatial resolution was 2.90x3.80x6.00 mm^3 for the mild and moderate patient groups and 3.43x3.66x3.50 mm^3 for the severe group. The through-plane spatial resolution was higher in the severe group to mitigate phase dispersion in eccentric and angulated regurgitation jets. Reconstructed spatial resolutions were 1.45x1.45x6.00 mm^3 and 2.89x2.89x3.50 mm^3, respectively, and the field of view was 370x370x48 mm^3 (mild and moderate) and 370x370x63 mm^3 (severe). Thirty cardiac phases were measured, resulting in reconstructed temporal resolutions of 21 to 39 ms.

3.2.3 Data analysis

Three methods were used to quantify Rvol across the MV: 1) indirect quantification, 2) semi-automated valve tracking, and 3) semi-automated flow tracking. Analyses were performed by C.P.S.B., who had 2.5 years of experience in cardiac 4D flow MRI analysis and access to the patients' echocardiography-based severity grades.

3.2.3.1 Indirect quantification

CAAS MR Ventricular analysis software (version 4.3, Pie Medical Imaging) was used to contour endocardial borders at end-diastole (LVEDV) and end-systole (LVESV) on short-axis bSSFP images to determine left ventricular stroke volume (LVSV = LVEDV – LVESV). Calculation of LVSV included apex-to-base volume correction based on manually drawn long-axis (2CH and 4CH) endo- and epicardial contours. Forward flow volume across the ascending aorta (AAo) was determined from 2D flow MRI (CAAS MR Flow version 1.1, Pie Medical Imaging) and Rvol was indirectly quantified by: $Rvol_{INDIRECT}$ = LVSV – AAo forward flow volume (**Figure 3.1**). $Rvol_{INDIRECT}$ was chosen as a reference standard because of its good prognostic value and reproducibility (4–8).

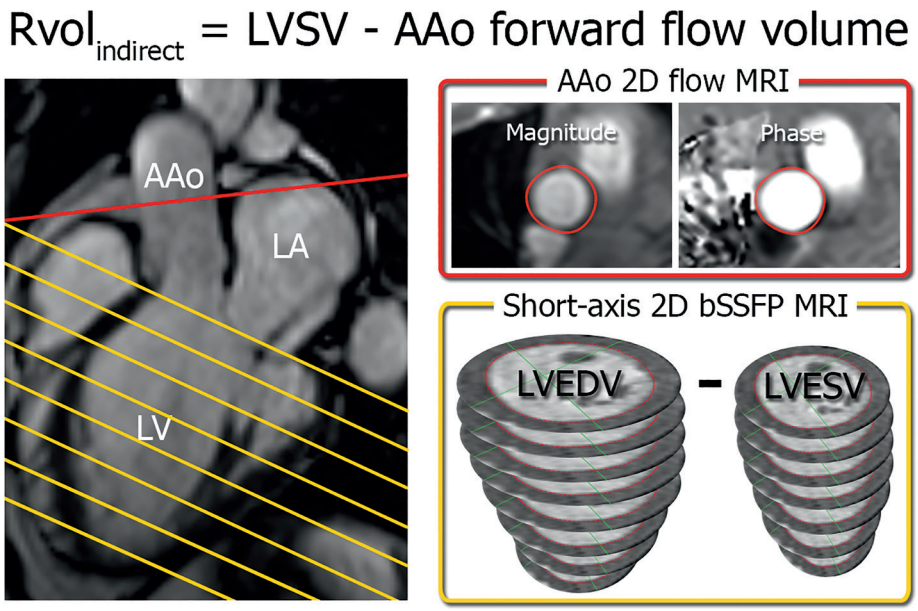

Figure 3.1: Indirect Rvol quantification by MRI, by short-axis bSSFP MRI in the left ventricle (yellow) and 2D flow MRI in the ascending aorta (AAo, red). Left: Slice locations are indicated on a three-chamber bSSFP image. Right: Semi-automated contouring of the aortic flow area (top) and the LV endocardial borders at end-diastole and end-systole (bottom) allows for quantification of the AAo forward flow volume and LVSV, and calculation of $Rvol_{INDIRECT}$. AAo = ascending aorta, LV = left ventricle, LA = left atrium, LVEDV = left ventricular end-diastolic volume, LVESV = left ventricular end-systolic volume, LVSV = left ventricular stroke volume.

3.2.3.2 Valve tracking

Valve tracking was performed on 2D cine bSSFP images (CAAS MR Solutions version 5.1 - 4D flow, Pie Medical Imaging). The MV was tracked on a 2CH and 4CH cine view. After manually identifying the location of the MV annulus by selecting two points in each view at a single phase, the motion of the valve was tracked automatically throughout the cardiac cycle. If correction was needed, the automated tracking was repeated starting from a different cardiac phase. Next, color-coded 4D flow MRI-derived in-plane velocities were projected onto the moving long-axis cine views to check for possible misalignment between the 4D flow MRI data and cine images, which could be corrected for by means of translation. Next, a time-resolved 3D plane was reconstructed and mapped to the 4D flow MRI data, and an initial four-point contour was generated automatically based on the landmark points that were used for tracking in the 2CH and 4CH cine views. Visual feedback was provided by a color-coded 4D flow MRI through-plane velocity overlay and used to make manual adjustments to the

contour. Finally, forward and backward blood flow were quantified in ml/heartbeat, corrected for through-plane valve motion based on the tracked valve. For every cardiac phase streamlines were generated from within the contour to allow 3D visualization superimposed on the long-axis cine views. Valve tracking-derived Rvol will be referred to as $Rvol_{VALVE}$.

In case of MV prolapse that caused the regurgitant orifice to be located in the atrium and not in the annular plane, an additional measurement was obtained in which the valve tracking plane was moved to the level of the regurgitant orifice during regurgitation. This correction was performed to anticipate for the possibility of Rvol underestimation merely due to a spatial mismatch between the location of measurement and the regurgitant orifice.

3.2.3.3 Flow tracking

Flow tracking was only performed when regurgitation was present, i.e. during systole. Color-coded 4D flow MRI-derived in-plane velocities were projected onto the moving long-axis cine views and served to identify the location of the MR jet on a 2CH and 4CH cine bSSFP image (CAAS MR Solutions version 5.1 - 4D flow, Pie Medical Imaging). By clicking in the MR jet, 1–2 cm distal to the regurgitant orifice inside the left atrium, a measurement plane was generated and automatically angulated perpendicular to the direction of the regurgitant jet. In the reformatted measurement plane, an initial four-point contour was generated automatically and manually adjusted where needed based on the 4D flow MRI velocity map. Flow tracking-derived Rvol will be referred to as $Rvol_{FLOW}$. Both tracking methods included automatic velocity aliasing correction and velocity offset correction, performed by fitting a linear plane through the intensities of automatically detected stationary tissue voxels in the phase contrast images. The phase contrast values of the linear plane were subsequently subtracted from the original images (22).

All three abovementioned methods to determine Rvol were repeated by a second observer J.J.M.W. with 15 years of experience in cardiac 4D flow MRI analysis, to test for reproducibility. For validation purposes, the first observer also quantified forward and backward flow across the AV by semi-automated valve tracking and when appropriate flow tracking, to test for intervalve consistency based on the principle of conservation of mass (MV forward flow volume – MV backward flow volume (referred

to as Rvol) = AV forward flow volume – AV backward flow volume). Valve tracking of the AV was performed on a coronal and 3CH cine bSSFP.

4D flow MRI-based severity grades were compared with echocardiography-based grades after applying pre-specified cutoff values (≥30 and ≥60 ml for moderate and severe MR, respectively) (2,20) to $Rvol_{FLOW}$ and $Rvol_{VALVE}$.

3.2.4 Statistical analysis

Statistical testing was performed using SPSS Statistics (v25.0, IBM Corp., Armonk, N.Y., USA) by C.P.S.B. Normality testing was performed using a Shapiro–Wilk test. Agreements between $Rvol_{INDIRECT,}$ $Rvol_{VALVE}$ and $Rvol_{FLOW}$ were evaluated using a Friedman test and post-hoc Wilcoxon signed-rank tests. The agreement between MV and AV net flow volume was assessed using a Wilcoxon signed-rank test. Orthogonal regression and Bland–Altman analysis were used to further assess the agreements between the observed variables and to evaluate interobserver agreements. Coefficients of variation (CV) were also determined, defined as the standard deviation of the interobserver differences in Rvol divided by the mean Rvol between both observers. Pearson correlation coefficient is denoted by r and a p-value of <0.05 was considered significant. 4D flow MRI- and echocardiography-based severity classifications were compared using categorical scatter plots and contingency tables.

3.3 Results

Semi-automated valve tracking and flow tracking allowed for quantification of Rvol in all MR patients. **Figure 3.2** shows a representative example. The results are shown in **Figure 3.3**, plotted against $Rvol_{INDIRECT}$ measurements. Significant differences were found among $Rvol_{INDIRECT,}$ $Rvol_{VALVE}$ and $Rvol_{FLOW}$ ($p < 0.001$). Overall, $Rvol_{FLOW}$ was higher (24.8 ml, IQR 14.3–45.7 ml) than $Rvol_{VALVE}$ (9.9 ml, IQR 6.0–16.9 ml, $p < 0.001$). Both $Rvol_{FLOW}$ and $Rvol_{VALVE}$ differed significantly from $Rvol_{INDIRECT}$ (19.1 ml, IQR 4.1–47.5 ml, $p = 0.03$ in both cases). Orthogonal regression revealed better agreement between $Rvol_{FLOW}$ and $Rvol_{INDIRECT}$ ($\hat{y} = 0.78x + 12$, $r = 0.88$) compared to $Rvol_{VALVE}$ and $Rvol_{INDIRECT}$ ($\hat{y} = 0.16x + 8.1$, $r = 0.53$). Bland–Altman analysis revealed a trend towards underestimation of $Rvol_{VALVE}$ in severe MR, see **Figure 3.3** - bottom.

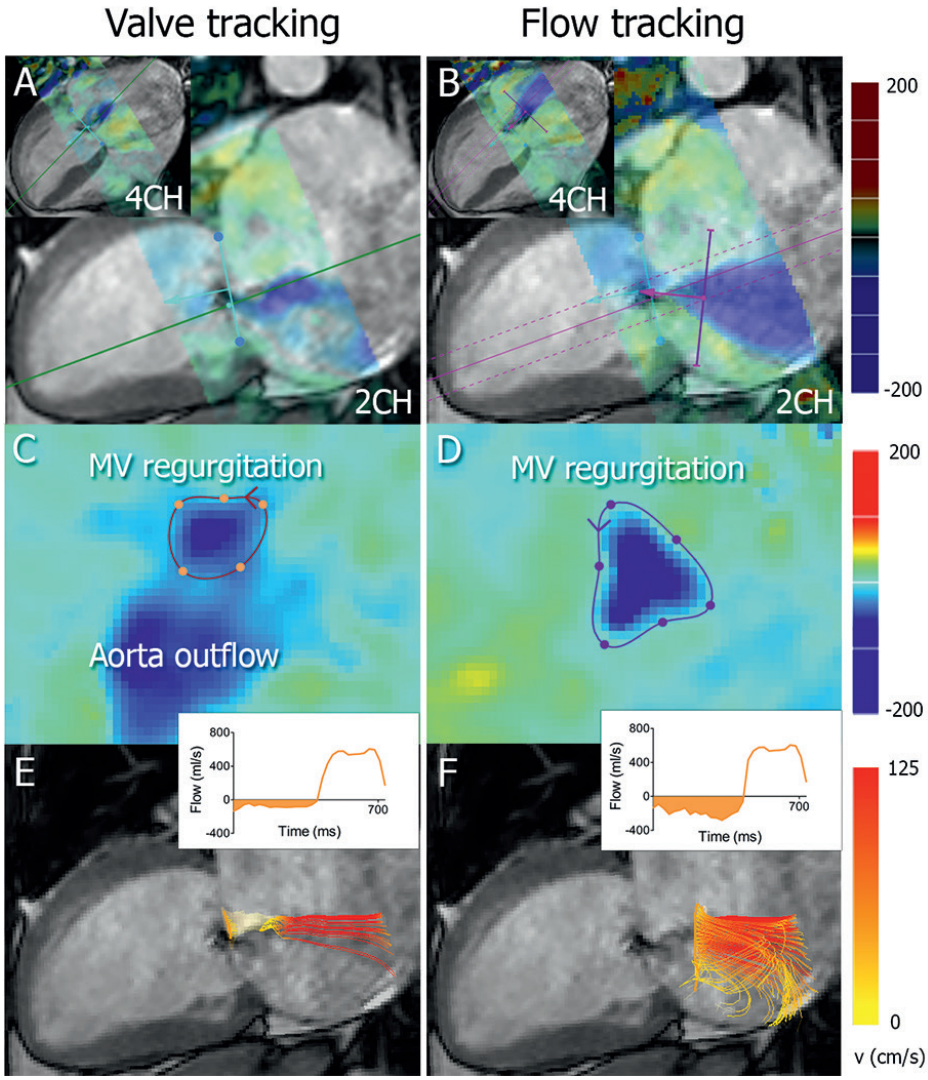

Figure 3.2: Rvol quantification from 4D flow MRI in a 38 y/o female with severe MR as diagnosed by echocardiography. **A–B)** The location of the MV annulus is identified on a 2-chamber (2CH) and 4-chamber (4CH) cine bSSFP image, followed by automatic valve tracking **(A)** throughout the cardiac cycle. During regurgitation, an additional plane is initialized to enable flow tracking **(B)**: at a distance of 1–2 cm from the regurgitant orifice and perpendicular to the direction of the regurgitant jet. Colors represent in-plane 4D flow MRI velocities projected onto the long-axis cine views. **C–D)** 4D flow MRI through-plane velocity measurements are projected onto the valve tracking or flow tracking plane, allowing for detailed contouring of the flow region of interest. **E–F)** Time-resolved streamlines are generated from within the contour and the flow is quantified (inset). MV = mitral valve.

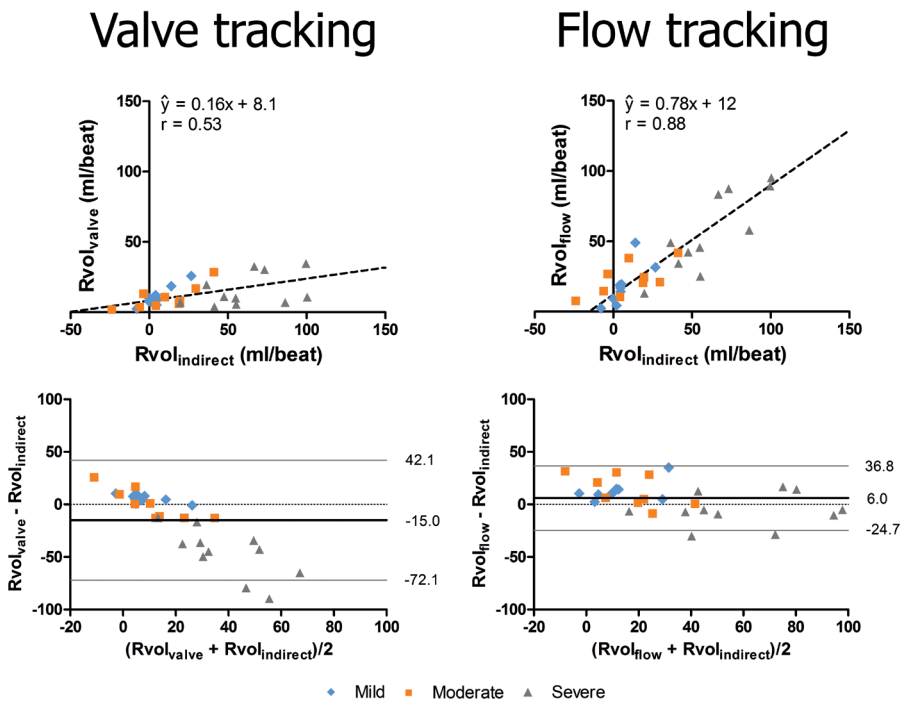

Figure 3.3: Orthogonal regression (top) and Bland–Altman plots (bottom) of Rvol measured with valve tracking ($Rvol_{VALVE}$, left) and flow tracking ($Rvol_{FLOW}$, right) versus indirectly quantified Rvol ($Rvol_{INDIRECT}$ = LVSV – AAo flow). Mean differences and 95% limits of agreement are indicated by the black and grey lines in the Bland–Altman plots. There is higher agreement between $Rvol_{FLOW}$ and $Rvol_{INDIRECT}$ than between $Rvol_{VALVE}$ and $Rvol_{INDIRECT}$.

According to orthogonal regression, interobserver agreement was excellent for $Rvol_{INDIRECT}$ (r = 0.91, CV = 48%), moderate for $Rvol_{VALVE}$ (r = 0.72, CV = 57%) and excellent for $Rvol_{FLOW}$ (r = 0.95, CV = 27%). Bland–Altman plots of the interobserver differences can be found in **Supplemental Figure 3.1**. Limits of agreement were widest for $Rvol_{INDIRECT}$. The largest mean difference was observed for $Rvol_{FLOW}$.

Initially, a large interobserver difference (64 mL) was seen in one patient with severe MV regurgitation. After discussing the analysis with the first observer, the second observer revised his findings. The reason for the initial discrepancy was the presence of multiple jets of which part was not identified by the second observer due to high angulation of the measurement plane close to the border of the FOV. After revision, a difference of 32 ml between the observers remained as a result of differently angulated

measurement planes with respect to the multiple jets. Videos of the analyses of the two observers can be found in **Supplemental Videos 3.1** and **3.2**.

Eight severe MR cases had MV prolapse that caused the regurgitant orifice to be located in the atrium and not in the annular plane. Moving the valve tracking plane to the level of the regurgitant orifice in these cases improved the agreement between $Rvol_{VALVE}$ and $Rvol_{INDIRECT}$, albeit only modestly ($\hat{y} = 0.28x + 7.6$, $r = 0.75$). Jet eccentricity was observed in 7 severe MR patients and 3 moderate MR patients, in whom jets impinged on the left atrial wall in all but 3 patients. Furthermore, 5 severe MR cases had multiple jets. In 2 of these, the jets left the regurgitant orifice in different directions and thus, it was not possible to place the measurement plane perpendicular to all jets.

Figure 3.4 demonstrates the forward flow measurements across the MV and AV which were used to test for intervalve consistency. Orthogonal regression demonstrated better intervalve consistency for flow tracking than for valve tracking in terms of the correlation coefficient r (0.82 vs. 0.67) and the slope being closer to 1 and the intercept to 0 (1.2 vs. 2.7 and –13.4 vs. –92.4, respectively), see **Figure 3.5**. There was a statistically significant difference (i.e. inconsistency) between MV net flow volume (i.e forward flow volume – Rvol) and AV net flow volume when Rvol was quantified using valve tracking (MV: 80.1 ml, IQR 70.2–121.3 ml, AV: 67.0 ml, IQR 52.3–84.0 ml, $p < 0.001$) but not when Rvol was quantified using flow tracking (MV: 69.4 ml, IQR 55.5–85.0 ml, AV: 67.0 ml, IQR 52.3–84.0 ml, $p = 0.85$). This finding was especially apparent in the severe MR group, as shown in the Bland–Altman plots (**Figure 3.5** - bottom), and can be explained by an underestimation of Rvol using valve tracking.

There was a substantial overlap of MRI-derived Rvol measurements between mild, moderate and severe MR as diagnosed by semi-quantitative echocardiography. In **Figure 3.6**, it is shown that neither flow tracking nor valve tracking or the indirect method provided a sharp distinction between the severity groups. Moreover, it is shown that adoption of absolute cutoff values used in quantitative echocardiography (2,20) would cause the majority of moderate and severe MR cases to be reclassified to a lower class (**Figure 3.6**).

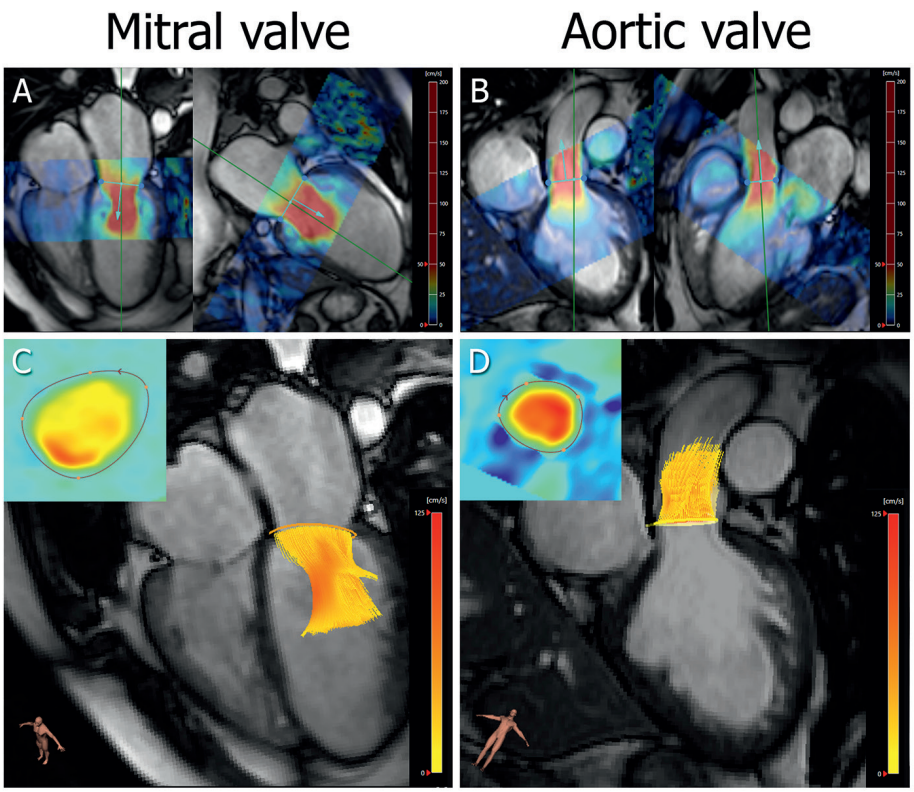

Figure 3.4: Forward flow quantification from 4D flow MRI across the MV and AV in a 45 y/o male with moderate MR as diagnosed by echocardiography. **A–B)** Semi-automated valve tracking on two orthogonal long-axis cine bSSFP images for each valve. Colors represent the in-plane velocity measured with 4D flow MRI. **C–D)** 4D flow MRI through-plane velocity measurements are projected onto the valve tracking plane (inset) and time-resolved streamlines are generated from within the contour.

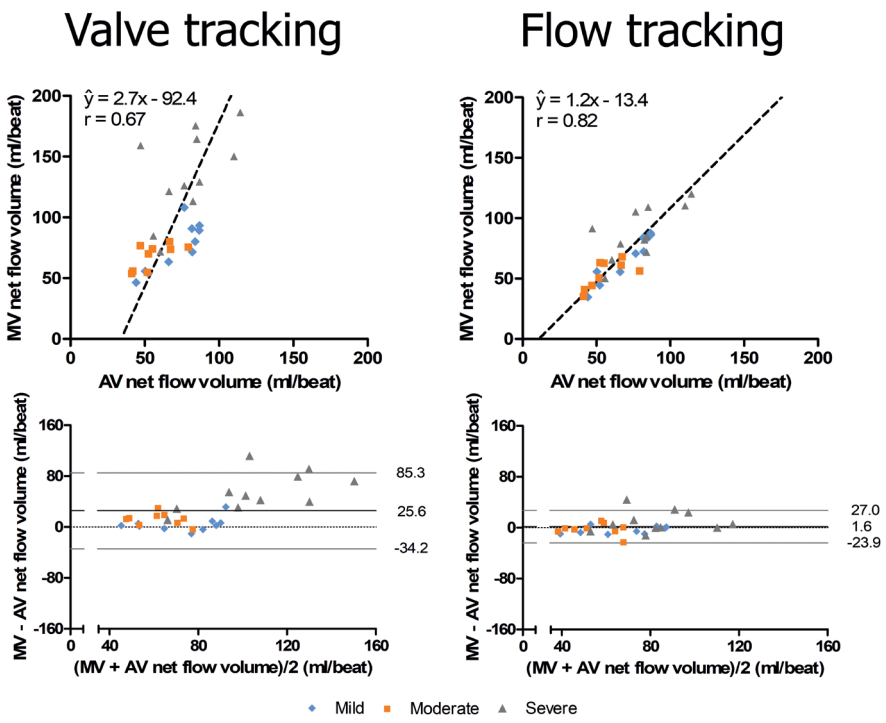

Figure 3.5: Orthogonal regression (top) and Bland–Altman plots (bottom) of MV net flow volume measured with valve tracking (left) and flow tracking (right) versus AV net flow volume measured with valve tracking. Mean differences and 95% limits of agreement are indicated by the black and grey lines in the Bland–Altman plots. Flow tracking demonstrates better agreement between MV net flow volume and AV net flow volume than valve tracking. MV = mitral valve, AV = aortic valve.

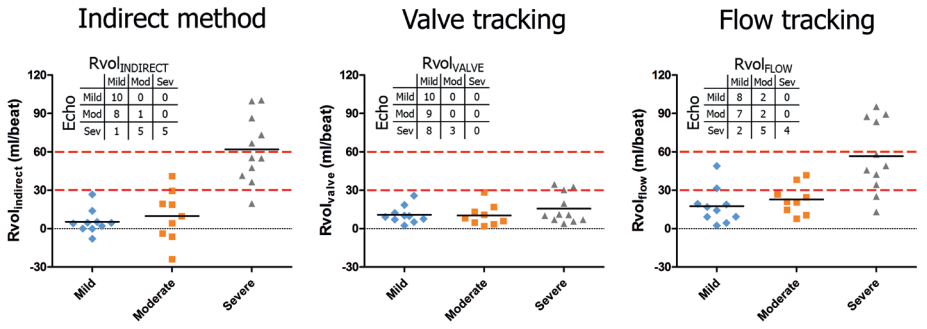

Figure 3.6: Rvol measured using the indirect method (left), 4D flow MRI in combination with valve tracking (middle) and 4D flow MRI in combination with flow tracking (right), divided into classes of severity based on semi-quantitative echocardiography. Black horizontal lines represent Rvol means per severity class. Dashed red lines indicate cut-off values for mild MR (Rvol < 30ml), moderate MR (Rvol 30–59 ml) and severe MR (Rvol ≥ 60ml) used in quantitative echocardiography. Adoption of these cutoff values would cause the majority of moderate and severe MR cases to be reclassified to a lower class. Inset contingency tables provide comparison of MRI-based severity classification resulting from cutoff values of 30 and 60 ml with echocardiography-based classification. Neither flow tracking nor valve tracking or the indirect method provide a sharp distinction between the severity groups.

3.4 Discussion

In this study, we quantified mitral valve regurgitation from clinical 4D flow MRI data by means of semi-automated flow tracking and semi-automated valve tracking. Flow tracking provided more accurate quantification of MR than valve tracking in terms of agreement with indirect quantification and consistency of net flow volumes over the MV and AV, in particular in severe MR. Interobserver analysis demonstrated excellent reproducibility for flow tracking and moderate reproducibility for valve tracking.

Several factors may underlie the observation that valve tracking did not allow for accurate Rvol measurements in severe MR whereas flow tracking did. Contributing factors may be valve morphology, dynamic jets or jet eccentricity, as well as high flow velocities leading to signal loss as a result of intravoxel phase dispersion and incoherent flow effects. By moving the measurement plane away from the valve to a region of more coherent flow and lower velocities we were able to minimize signal loss. Apart from signal loss, flow displacement effects might also explain why flow tracking captured severe regurgitation jets better than valve tracking. Flow displacement

occurs when relatively long echo times, like those used in EPI readout, cause spatial information to be encoded at a later time point during TR than velocity information. In high-velocity regurgitation jets, this effect may result in misregistration of velocities in the regurgitant orifice to a location more upstream along the regurgitant jet. Based on the VENC and echo time used in the severe MR group (180 cm/s and 4.0 ms in 9 out of 11 severe MR cases), this displacement can theoretically measure up to 0.7 cm. Considering the 0.35cm interslice distance and the 1–2 cm distance between the valve tracking and flow tracking plane, it is possible that flow displacement contributed to the difference between $Rvol_{VALVE}$ and $Rvol_{FLOW}$ in severe MR jets. Future studies with different 4D flow MRI acquisition strategies are warranted to provide more insight into the benefits of flow tracking in MR.

In the interobserver analysis, two measures of reproducibility can be discerned: systematic bias (which was largest for $Rvol_{FLOW}$) and overall variability (which was largest for $Rvol_{INDIRECT}$). The observed variability in $Rvol_{INDIRECT}$ can be attributed to variability in LVSV measurements. The systematic bias in $Rvol_{FLOW}$ measurements was, in retrospect, due to a systematic difference in how the observers contoured the regurgitant flow areas (the first observer contoured a wider area than the second observer). Semi-automatic contour definition based on e.g. velocity isolines may in the future resolve the systematic bias as observed in this study.

The presence of multiple regurgitation jets was found to introduce interobserver variability: the three largest interobserver differences in this study were observed in severe MR cases with multiple jets. These findings bring to light an important challenge in the accurate quantification of severe MR and multiple jets. Automatic detection of MR jets and multiple planes of measurement potentially further reduce this observer variation.

An advantage of flow tracking over valve tracking in the studied cohort is the fact that the region of interest could generally be better separated from the simultaneous aortic outflow. It is of note that although the through-plane spatial resolution was relatively high in the severe MR patient group (3.50 mm as opposed to 6.00 mm in the mild and moderate MR groups), the in-plane resolution was slightly poorer (3.43x3.63 mm^2 as opposed to 2.90x3.80 mm^2 in mild and moderate MR), which might have caused $Rvol_{VALVE}$ measurements in severe MR patients to be affected more by phase dispersion-induced signal loss. MV prolapse is another potential reason for

Rvol underestimation by valve tracking. However, in the current study we found that moving the valve tracking plane to the level of the regurgitant orifice only subtly improved the measurement.

Recent studies have reported discordance between MRI-based and echocardiography-based assessment of MR (4,6). In our study, MRI-based Rvol measurements did not relate well to echocardiography-based severity grades either. It should be considered that echocardiography- and MRI-based severity assessment relied on different parameters. Echocardiographic evaluation did not include quantification of Rvol which was in fact the only MRI parameter considered. However, a combination of MRI-derived parameters may have higher prognostic value than Rvol alone. Rvol has for instance been shown to strongly correlate with LV end-diastolic volume, as well as post-surgical decrease in LV end-diastolic volume (4,23). Also, LV end-systolic volume has been shown to improve specificity in MRI-based prognostication of severe MR patients in addition to (indirectly quantified) Rvol (6) and left atrial volume indexed to body surface ratio has been identified as a predictor of long-term outcome in primary organic MR (24,25). Other parameters that could be considered for prognostic purposes in addition to Rvol are systolic pulmonary flow reversal and regurgitant jet eccentricity, both taken into account in echocardiography-based grading. Finally, impaired left ventricular strain is a promising imaging biomarker of early myocardial dysfunction in patients with MR (26,27).

The higher prognostic power that MRI-derived Rvol was found to have over other MRI- or echocardiography-derived measures (4–6) underlines the importance of taking this parameter into account in surgical decision-making. Untreated severe MR is associated with poor survival while timely intervention results in improved outcome (6,28). Furthermore, the 2017 Euro Heart Survey and the Olmsted County study have shown that surgical treatment is being denied in up to 49% of symptomatic patients with severe MR, mainly as a result of too late referral for surgery, leading to increased morbidity and mortality (29,30). Timely Rvol quantification by MRI may improve surgical timing in MR, although it is not yet part of clinical guidelines. Compared to the indirect method which is still more widely available, 4D flow MRI in combination with flow tracking is advantageous in 1. the ability to not only quantify but also visualize the (regurgitant) blood flow, to get a better understanding of the cause of the regurgitation and 2. the ability to perform measurements across all heart valves, allowing for intervalve consistency testing. Further studies in large cohorts

with the correlation of clinical outcomes are important to strengthen the role of MRI-derived Rvol in clinical practice. We like to stress that we do not consider the indirect method to be the reference standard, although the best reference currently available.

Previous reports on 4D flow MRI-derived quantification of MR demonstrated its feasibility in mild and moderate MR with valve tracking, but not in severe MR (11,17). Our study shows that 4D flow MRI in combination with flow tracking enables accurate quantification even in severe MR. Due to the volumetric nature of the acquisition, eccentric and dynamic regurgitation jets can be captured without knowledge of the regurgitation pattern prior to image acquisition (which is required in 2D flow MRI) and without operator dependency or geometrical/directional restrictions during acquisition planning, unlike in echocardiography. The acquisition is less sensitive to physiological variability than the indirect method which requires multiple breathholds at different moments in time. In 4D flow MRI, measurements at different locations are all influenced equally by physiological variability, since the final image series are an average over all the measured cardiac cycles.

A number of limitations of our study should be noted. First of all, there was a difference in MR etiology between the patient groups: severe MR patients had primary, asymptomatic MR as a result of an intrinsically abnormal MV whereas mild and moderate patients had secondary MR. It is likely that complex valve morphology in primary MR complicated MR quantification due to consequent jet eccentricity and complexity. Future studies on quantification of primary MR of varying severity grades are warranted. Furthermore, the severe MR patients received MRI and echocardiography several days or weeks apart, whereas the mild and moderate MR patients received the exams on the same day. The accuracy of the flow measurements may have been limited by the relatively low spatial resolution and long echo time. Another limitation was the anisotropic voxel size of the 4D flow MRI acquisitions. This could have affected measurement accuracy in eccentric regurgitation jets angulated to the basal plane of the heart, to which the acquisition volume was planned parallel. With regard to the placement of the flow tracking plane – perpendicular to the regurgitant jet – it is important to note that in theory non-perpendicular placement should not result in different measurement results, as the decrease in through-plane velocities is compensated for by an increase in flow area. In practice, however, partial volume effects can cause errors and non-perpendicular measurement results in poorer definition of the flow area of interest due to more diffuse boundaries. The impact of

the plane angulation was not explored in our study, nor was the impact of the distance to the regurgitant orifice. In case of multiple jets, the measurement plane was as much as possible placed perpendicular to the largest jet. In case of impingement to the left atrial wall, the measurement was obtained before the area of impingement if possible and otherwise along the left atrial wall.

In conclusion, semi-automated flow tracking provides more accurate Rvol quantification in patients with MR than semi-automated valve tracking, in particular in severe MR. Whether the use of 4D flow MRI in combination with semi-automated flow tracking can improve prognostication in MR patients has to be investigated in future studies.

3.5 Supplemental material

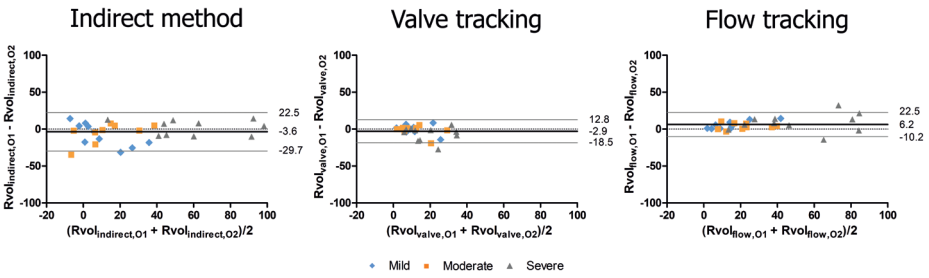

Supplemental Figure 3.1: Bland–Altman plots of Rvol measurements by two observers, for the indirect method, valve tracking and flow tracking. O1 = observer 1, O2 = observer 2. Mean differences and 95% limits of agreement are indicated by the black and grey lines.

Supplemental Video 3.1: Flow quantification from 4D flow MRI in a 59 y/o male with severe MR and multiple regurgitation jets by observer 1. Video can be found online: https://pubs.rsna.org/doi/suppl/10.1148/ryct.2020200004.

Supplemental Video 3.2: Flow quantification from 4D flow MRI in a 59 y/o male with severe MR and multiple regurgitation jets by observer 2. Video can be found online: https://pubs.rsna.org/doi/suppl/10.1148/ryct.2020200004.

3.6 References

1. Zamorano JL, Fernández-Golfín C, González-Gómez A. Quantification of mitral regurgitation by echocardiography. Heart. 2015;101(2):146–154.
2. Zoghbi WA, Adams D, Bonow RO, et al. Recommendations for Noninvasive Evaluation of Native Valvular Regurgitation: A Report from the American Society of Echocardiography Developed in Collaboration with the Society for Cardiovascular Magnetic Resonance. J Am Soc Echocardiogr. 2017;30(4):303–371.
3. Baumgartner H, Falk V, Bax JJ, et al. 2017 ESC/EACTS Guidelines for the management of valvular heart disease. Eur Heart J. 2017;38(36):2739–2786.
4. Uretsky S, Gillam L, Lang R, et al. Discordance between echocardiography and MRI in the assessment of mitral regurgitation severity: a prospective multicenter trial. J Am Coll Cardiol. 2015;65(11):1078–1088.
5. Myerson SG, D'Arcy J, Christiansen JP, et al. Determination of Clinical Outcome in Mitral Regurgitation With Cardiovascular Magnetic Resonance Quantification. Circulation. 2016;133(23):2287–2296.
6. Penicka M, Vecera J, Mirica DC, Kotrc M, Kockova R, Van Camp G. Prognostic Implications of Magnetic Resonance-Derived Quantification in Asymptomatic Patients With Organic Mitral Regurgitation: Comparison With Doppler Echocardiography-Derived Integrative Approach. Circulation. 2017;137(13):1349–1360.
7. Bellenger N, Burgess MI, Ray SG, et al. Comparison of left ventricular ejection fraction and volumes in heart failure by echocardiography, radionuclide ventriculography and cardiovascular magnetic resonance. Are they interchangeable? Eur Heart J. 2000;21(16):1387–1396.
8. Elliott PM, Anastasakis A, Borger MA, et al. 2014 ESC Guidelines on diagnosis and management of hypertrophic cardiomyopathy. Eur Heart J. 2014;35(39):2733–2779.
9. Biner S, Rafique A, Rafii F, et al. Reproducibility of proximal isovelocity surface area, vena contracta, and regurgitant jet area for assessment of mitral regurgitation severity. JACC Cardiovasc Imaging. 2010;3(3):235–243.
10. Westenberg JJM, Roes SD, Ajmone Marsan N, et al. Mitral Valve and Tricuspid Valve Blood Flow: Accurate Quantification with 3D Velocity-encoded MR Imaging with Retrospective Valve Tracking. Radiology. 2008;249(3):792–800.
11. Kamphuis VP, Roest AAW, Ajmone Marsan N, et al. Automated Cardiac Valve Tracking for Flow Quantification with Four-dimensional Flow MRI. Radiology. 2019;290(1):70–78.
12. Hsiao A, Tariq U, Alley MT, Lustig M, Vasanawala SS. Inlet and outlet valve flow and regurgitant volume may be directly and reliably quantified with accelerated, volumetric phase-contrast MRI. J Magn Reson Imaging. 2015;41(2):376–385.
13. Urchuk SN, Plewes DB. Mechanisms of flow-induced signal loss in MR angiography. J Magn Reson Imaging. 1992;2(4):453–462.
14. Gatenby JC, McCauley TR, Gore JC. Mechanisms of signal loss in magnetic resonance imaging of stenoses. Med Phys. 1993;20(4):1049–1057.
15. Westenberg JJ., van der Geest RJ, Wasser MNJ., et al. Objective stenosis quantification from post-stenotic signal loss in phase-contrast magnetic resonance angiographic datasets of flow phantoms and renal arteries. Magn Reson Imaging. 1998;16(3):249–260.
16. Ferreira PF, Gatehouse PD, Mohiaddin RH, Firmin DN. Cardiovascular magnetic resonance artefacts. J Cardiovasc Magn Reson. 2013;15(1):41.
17. Calkoen EE, Westenberg JJ, Kroft LJ, et al. Characterization and quantification of dynamic eccentric regurgitation of the left atrioventricular valve after atrioventricular septal defect correction with 4D Flow cardiovascular magnetic resonance and retrospective valve tracking. J Cardiovasc Magn Reson. 2015;17(1):18.

18. Myerson SG, Francis JM, Neubauer S. Direct and indirect quantification of mitral regurgitation with cardiovascular magnetic resonance, and the effect of heart rate variability. Magn Reson Mater Physics, Biol Med. 2010;23(4):243–249.
19. Marsan NA, Westenberg JJM, Ypenburg C, et al. Quantification of Functional Mitral Regurgitation by Real-Time 3D Echocardiography. Comparison With 3D Velocity-Encoded Cardiac Magnetic Resonance. JACC Cardiovasc Imaging. 2009;2(11):1245–1252.
20. Vahanian A, Baumgartner H, Bax J, et al. Guidelines on the management of valvular heart disease: The Task Force on the Management of Valvular Heart Disease of the European Society of Cardiology. Eur Heart J. 2007;28(2):230–268.
21. Jansen R, Hart EA, Peters M, et al. An easy-to-use scoring index to determine severity of mitral regurgitation by 2D echocardiography in clinical practice. Echocardiography. 2017;34(9):1275–1283.
22. Walker PG, Cranney GB, Scheidegger MB, Waseleski G, Pohost GM, Yoganathan AP. Semiautomated method for noise reduction and background phase error correction in MR phase velocity data. J Magn Reson Imaging. 1993;3(3):521–530.
23. Uretsky S, Supariwala A, Nidadovolu P, et al. Quantification of left ventricular remodeling in response to isolated aortic or mitral regurgitation. J Cardiovasc Magn Reson. 2010;12(1):32.
24. Le Tourneau T, Messika-Zeitoun D, Russo A, et al. Impact of left atrial volume on clinical outcome in organic mitral regurgitation. J Am Coll Cardiol. 2010;56(7):570–578.
25. Rusinaru D, Tribouilloy C, Grigioni F, et al. Left atrial size is a potent predictor of mortality in mitral regurgitation due to flail leaflets: results from a large international multicenter study. Circ Cardiovasc Imaging. 2011;4(5):473–481.
26. Schiros CG, Dell'Italia LJ, Gladden JD, et al. Magnetic resonance imaging with 3-dimensional analysis of left ventricular remodeling in isolated mitral regurgitation: Implications beyond dimensions. Circulation. 2012;125(19):2334–2342.
27. Ahmed MI, Gladden JD, Litovsky SH, et al. Increased oxidative stress and cardiomyocyte myofibrillar degeneration in patients with chronic isolated mitral regurgitation and ejection fraction >60%. J Am Coll Cardiol. 2010;55(7):671–679.
28. Suri RM, Vanoverschelde J-L, Grigioni F, et al. Association Between Early Surgical Intervention vs Watchful Waiting and Outcomes for Mitral Regurgitation Due to Flail Mitral Valve Leaflets. JAMA. 2013;310(6):609–616.
29. Dziadzko V, Clavel MA, Dziadzko M, et al. Outcome and undertreatment of mitral regurgitation: a community cohort study. Lancet. 2018;391(10124):960–969.
30. Mirabel M, Iung B, Baron G, et al. What are the characteristics of patients with severe, symptomatic, mitral regurgitation who are denied surgery? Eur Heart J. 2007;28(11):1358–1365.

4

Whole-Heart 4D Flow MRI for Evaluation of Normal and Regurgitant Valvular Flow: A Quantitative Comparison Between Pseudo-Spiral Sampling and EPI Readout

Carmen P.S. Blanken
Lukas M. Gottwald
Jos J.M. Westenberg
Eva S. Peper
Bram F. Coolen
Gustav J. Strijkers
Aart J. Nederveen
R. Nils Planken
Pim van Ooij

J. Magn. Reson. Imaging 2021.

Abstract

Background

Pseudo-spiral Cartesian sampling with random undersampling in time and compressed sensing reconstruction has facilitated highly accelerated 4D flow MRI in various cardiovascular structures. Whole-heart application of this technique requires separate validation. EPI-accelerated whole-heart 4D flow MRI has previously been validated.

Hypothesis

Pseudo-spiral sampling, referred to as PROUD, is comparable to EPI in robustness of valvular flow measurements and remains comparable for shorter scan times.

Study type

Prospective.

Population

Twelve healthy subjects and eight patients with valve regurgitation.

Field strength/sequence

3.0 T; PROUD and EPI whole-heart 4D flow MRI.

Assessment

Valvular blood flow was quantified using valve tracking. Measurements of aortic and pulmonary (AV and PV) flow volumes and left and right ventricular stroke volumes (LVSV and RVSV) were tested for agreement with 2D MRI-based measurements. PROUD acquisitions with undersampling factors R of 9, 14, 28 and 56 were tested for intervalve consistency and preservation of peak velocities and E/A ratios.

Statistical tests

Repeated measures ANOVA ($p < 0.05$ considered significant), Bland–Altman, Wilcoxon signed-rank test, intraclass correlation coefficients.

Results

No significant differences were found between PROUD and EPI intervalve consistencies, both in healthy subjects (mean difference [limits of agreement width]: 3.2 ± 0.8 [8.7 ± 1.1] ml/beat for PROUD, 5.5 ± 2.9 [13.7 ± 2.3] ml/beat for EPI) and in patients (2.3 ±

1.2 [15.3 ± 5.9] ml/beat for PROUD, 0.6 ± 0.6 [19.3 ± 2.9] ml/beat for EPI). Agreement between the 4D flow techniques was higher than between 4D flow (EPI or PROUD) and 2D MRI for forward flow, stroke volumes and regurgitant volumes. Up to R=28 in healthy subjects and R=14 in patients, PROUD intervalve consistency remained comparable to that of EPI. Peak velocities and E/A ratios were preserved up to R=9.

Conclusion

PROUD is a reliable technique for intracardiac flow quantification in <10 minutes that is comparable to EPI in terms of intervalve consistency. Our findings suggest that PROUD scan times may be shortened.

4.1 Introduction

4D flow MRI facilitates detailed evaluation of cardiac hemodynamics in various types of heart disease (1,2). Whole-heart coverage is desirable for the assessment of diseases that affect the blood flow not just locally but throughout the heart, like repaired transposition of the great arteries (TGA), repaired tetralogy of Fallot (ToF) and multiple or complex valvular heart disease. In this context, whole-heart 4D flow MRI has been used for identification of helical and vortical flow patterns, increased flow velocities, regions of elevated wall shear stress and valvular regurgitation (3–9).

Advanced acquisition strategies have enabled whole-heart coverage at scan times of ~10 minutes (7,9,10), such that the acquisition can be performed in addition to existing clinical protocols. A recently introduced pseudo-spiral Cartesian sampling strategy with random undersampling in time and compressed sensing (CS) reconstruction has facilitated accurate and repeatable 4D flow MRI in the aorta, carotid arteries and intracranial arteries (11–13). This technique allows for artifact-free image recovery up to high undersampling factors by exploiting image sparsity. Undersampling factors of 8 (aorta) to 30 (intracranial) have been achieved while maintaining good agreement in flow measurements with other accelerated 4D flow MRI techniques and 2D flow MRI measurements. These results encouraged us to investigate the application of pseudo-spiral sampling 4D flow MRI in a whole-heart setting.

In order to assess the robustness of intracardiac flow measurements, quantification of forward and regurgitant flow volumes across the heart valves can be performed using retrospective valve tracking. Various studies have demonstrated that this analysis technique has good interobserver agreement (8,9,14,15). These studies used an echo planar imaging (EPI) readout acquisition technique which has demonstrated good intervalve consistency of flow measurements, and superiority to 4D segmented spoiled gradient echo (SPGR) and 4D k-t BLAST in terms of image quality and accuracy of intracardiac flow and velocity measurements (8–10). Hence, we deemed EPI-accelerated whole-heart 4D flow MRI a meaningful reference technique for the interpretation of intervalve consistency results of pseudo-spiral sampling whole-heart 4D flow MRI.

Thus, the aim of this study was to investigate the performance of pseudo-spiral Cartesian whole-heart 4D flow MRI in healthy subjects and patients with valvular

regurgitation and to compare its performance to that of a clinically used EPI readout strategy (14) based on blood flow measurements across the heart valves. Specifically, the aim was to assess intervalve consistency and agreement with 2D MRI-based measurements. A further aim was to investigate the possibility of shortening the scan time further by increasing the undersampling factor (16,17).

4.2 Materials and methods

All healthy subjects gave written informed consent. The requirement for written informed consent from the patients was waived by our local medical ethical committee, as the study served as protocol validation and the data were fully anonymized.

4.2.1 Study population and data acquisition

Twelve healthy subjects (aged 25 ± 3y; 7 female, 5 male) and 8 patients with valvular regurgitation (aged 39 ± 18y; 3 female, 5 male) underwent cardiac MRI at 3T (Philips Ingenia) including two whole-heart 4D flow MRI acquisitions in the same exam: 1) EPI readout 4D flow MRI, and 2) pseudo-spiral Cartesian sampling 4D flow MRI with random undersampling in time and CS reconstruction aided by total variation regularization in time. The pseudo-spiral sampling results in incoherently sampled k-space in time, making it suitable for CS reconstruction. To enable pseudo-spiral ky/kz-plane acquisition, the scanner was equipped with an in-house developed software modification called "PROspective Undersampling in multiple Dimensions (PROUD)" (11,12). We will therefore refer to the pseudo-spiral acquisitions as PROUD 4D flow scans.

The healthy subjects were prospectively scanned from October to December 2018. Patient scans were collected consecutively from August to October 2020. All patients received PROUD 4D flow MRI as part of their routine clinical MRI exam and had moderate to severe valvular regurgitation as diagnosed by semi-quantitative echocardiography, and no intracardiac shunting. EPI 4D flow MRI was prospectively added to the clinical protocol for comparison. Apart from the two 4D flow MRI sequences, cine balanced steady state free precession (bSSFP) MRI was acquired (two-chamber left and right, three-chamber, four-chamber, coronal aorta view, and sagittal and coronal pulmonary view). In the patients, 2D flow MRI was acquired at the aortic and the pulmonary valve at a spatial resolution of 1.2x1.2x8.0 mm^3 in 40 cardiac phases.

EPI and PROUD 4D flow data were acquired in 30 cardiac phases during free breathing with retrospective electrocardiographic (ECG) gating. Acquired and reconstructed spatial resolutions were 3.0x3.0x3.0 mm^3 and 2.8x2.8x3.0 mm^3 in healthy subjects, and 2.5x2.5x2.5 mm^3 and 2.4x2.4x2.5 mm^3 in patients (higher than in the healthy subjects to better capture complex hemodynamics in pathological areas). Three-directional velocity-encoding sensitivity (VENC) was set to 150 cm/s in healthy subjects and 150 to 300 cm/s in patients, depending on the presence of velocity aliasing in 2D flow MRI scout images.

EPI 4D flow MRI was acquired with a flip angle of 10° and echo time/repetition time (TE/TR) of 4.8/8.7 ms in the healthy subject scans and 4.3–5.4/8.1–10.0 ms in the patient scans. EPI temporal resolutions were 30.9 (IQR: 26.6, 35.1) ms in the healthy subjects and 30.8 (IQR: 27.1, 33.4) ms in the patients. The EPI factor was set to 5 and a SENSE factor of 2 was used.

In the PROUD scans, the flip angle was set to 8° and TE/TR were 3.0/5.1 ms in the healthy subject scans and 1.9–2.6/3.8–4.0 ms in the patient scans. PROUD temporal resolutions were 31.6 (IQR: 27.0, 36.6) ms in the healthy subjects and 31.3 (IQR: 27.2, 32.9) ms in the patients. In the healthy subjects, the PROUD undersampling factor ranged from 5.6 to 8.2 to achieve equal scan times for both 4D flow scans (9:20 ± 1:04 minutes). The difference in acceleration factors between EPI and PROUD was needed because of different phase-encoding directions: right-left for EPI – to minimize respiration-induced intravoxel phase dispersion artifacts – and anterior-posterior for PROUD. Furthermore, the scan time depended on the subject's heart rate during the EPI scan. The patients were scanned with a fixed PROUD undersampling factor of 7 to adhere to the standard clinical protocol, and the field of view (FOV) of the EPI scan was cropped in the craniocaudal dimension to achieve equal scan times (9:00 ± 1:10 min).

PROUD-accelerated 4D flow scans were reconstructed offline using ReconFrame (Gyrotools) and the Berkeley Advanced Reconstruction Toolbox (BART) (5). A sparsifying total variation transform in time was used with a regularization parameter (r) of 0.001 and 20 iteration steps, as previously described (11,12).

Reconstructed 4D flow MRI data sets were inspected for velocity aliasing in the phase images, and, if needed, unwrapped by a 4D single-step Laplacian algorithm (18).

In all PROUD scans, additional reconstructions of the first 75%, 50%, 25% and 12.5% of the acquired data were made. These will be referred to by the corresponding undersampling factors (R) of 9, 14, 28 and 56, respectively. The temporal resolutions of these additional reconstructions were similar to those of the original (R=7) reconstructions.

4.2.2 Data analysis

Data were analyzed by C.P.S.B., who had 3.5 years of experience in cardiac 4D flow MRI analysis.

4.2.2.1 4D flow MRI

Blood flow across the aortic, pulmonary, mitral and tricuspid valves (AV, PV, MV and TV) was quantified using semi-automated retrospective valve tracking including automatic phase offset correction in CAAS MR Solutions version 5.1 - 4D Flow, Pie Medical Imaging. Valve tracking was performed on 2D cine bSSFP images as previously described (15). The aortic valve was tracked on a sagittal and coronal cine view of the aortic root; the pulmonary valve was tracked on a sagittal and coronal cine view of the pulmonary root. The mitral valve and tricuspid valve were both tracked on a two-chamber (2CH, left-sided or right-sided) and four-chamber (4CH) cine view. 4D flow MRI velocity data were superimposed on the moving valve tracking planes, and these color-coded images were used to contour the flow area in every cardiac phase. The EPI and PROUD data sets were analyzed based on the same valve tracking planes, but separately defined contours. The blood flow was quantified in milliliters per heartbeat, corrected for through-plane valve motion. Streamlines, originating from within the measurement contours, provided 3D visualization of measured blood flow patterns over time. Regurgitant volumes were quantified using semi-automated flow tracking, as previously described (15). PROUD 4D flow reconstructions with different undersampling factors were analyzed by loading these into the existing valve tracking analyses and modifying the measurement contours where needed.

Left ventricular stroke volume (LVSV) was determined by summing AV forward flow volume and MV regurgitant volume; right ventricular stroke volume (RVSV) by summing PV forward flow volume and TV regurgitant volume. Peak velocities across the AV and PV and early diastole/atrial contraction (E/A) ratios across the MV and TV were determined based on time-resolved peak velocity curves.

Image quality in terms of signal-to-noise ratio (SNR) and lung-liver edge (LLE) width was assessed across an 8x8x30 (RLxAPxFH) voxel region-of-interest containing the lung-liver interface at the highest point of the liver, as previously described (19). In short, SNR was determined by measuring the time-averaged mean signal intensity in an 8x8-voxel slice in the liver and dividing this by the time-averaged standard deviation of the noise in an 8x8-voxel slice in the lung. LLE width was determined by fitting a sigmoid function to all (64) line profiles between the liver and lung slice.

4.2.2.2 2D MRI

2D flow MRI-based blood flow quantification was performed in CAAS MR Solutions (version 5.1 - 2D Flow, Pie Medical Imaging) with semi-automated contour definition around the flow regions of interest. Contours were manually modified where needed.

LVSV and RVSV were quantified in CAAS MR Solutions (version 5.1 - MRV, Pie Medical Imaging) from short-axis bSSFP images in a semi-automated manner: upon marking end-systolic and end-diastolic time frames, endocardial contours were automatically generated. These were manually adapted where needed. Apex-to-base volume correction was performed based on manual delineation of the endocardial border on 2CH and 4CH cine views. All LVSV and RVSV measurements were checked by a radiologist (R.N.P.) with 13 years of experience in cardiac MRI.

A combination of 2D short-axis bSSFP MRI and 2D flow MRI was used to quantify MV and TV regurgitant volumes ($Rvol_{MV}$ = LVSV – AV forward flow volume, $Rvol_{TV}$ = RVSV – PV forward flow volume). AV and PV regurgitant volumes were quantified directly from 2D flow MRI.

4.2.3 Statistical analysis

Statistical testing was performed in SPSS Statistics (version 26; IBM). Valve tracking-based net flows were tested for normality using Shapiro–Wilk tests. Intervalve differences in net flow volumes were identified using repeated measures ANOVA. A p-value of <0.05 was considered statistically significant. For each valve, net flow volume measurements were compared with the average measurement over the other three valves, and Bland–Altman analysis was performed. Mean difference, 95% limits of agreement (LOA) and coefficient of variation (CV) were calculated. Bland–Altman analysis was used to evaluate intervalve and intertechnique (4D flow vs. 2D flow, and PROUD 4D flow vs. EPI 4D flow) means and differences of measured flow volumes.

The Wilcoxon signed-rank test was used to compare intervalve consistencies between PROUD and EPI. Net flow volumes, E/A ratios and peak velocity measurements were compared between the increasingly undersampled reconstructions and the original reconstruction using Bland–Altman analysis and intraclass correlation coefficients (ICC). ICC was determined based on absolute agreement and a two-way mixed-effects model. ICC was classified as: poor (<0.5), moderate (0.5–0.75), good (0.75–0.9) and excellent (>0.9) (20). A Student's t-test was used to compare SNR and LLE width – averaged over all subjects – between EPI and PROUD, and between the PROUD R=7 reconstruction and R=9, 14, 28 and 56 reconstructions.

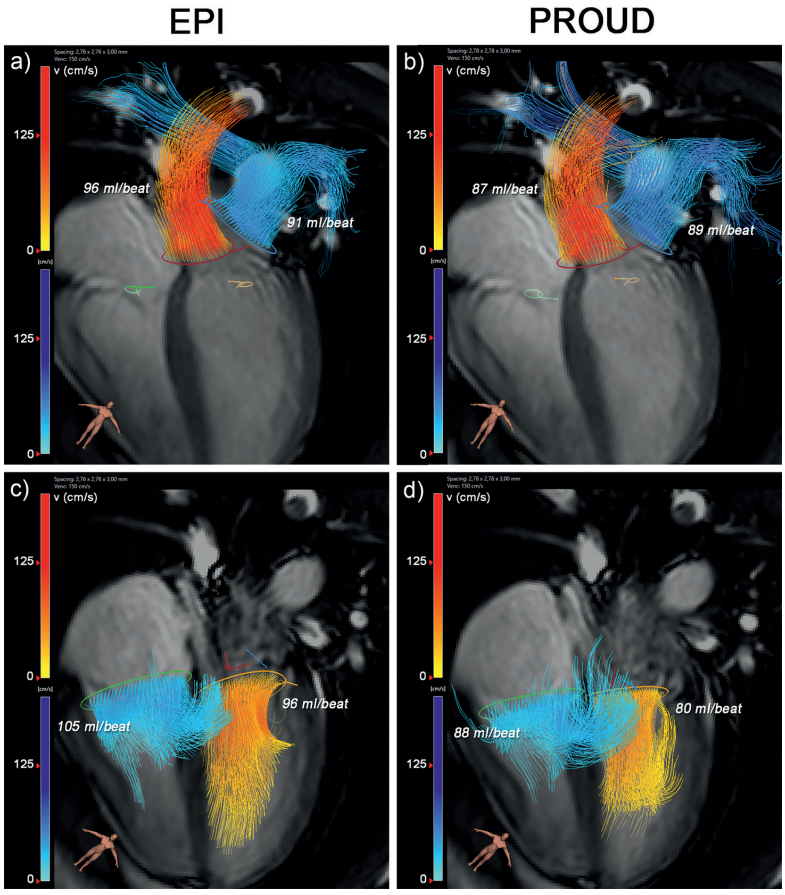

Figure 4.1: EPI and PROUD 4D flow MRI streamline visualizations of blood flow through the aortic valve (**a-b**, orange), pulmonary valve (**a–b**, blue), mitral valve (**c–d**, orange) and tricuspid valve (**c–d**, blue) in a 31-year-old healthy subject, resulting from semi-automated retrospective valve tracking. Measured flow volumes across the valves are listed in the figure. Valve tracking was performed on bSSFP cine images, on two orthogonal views for each heart valve. 4-chamber bSSFP view is visible in the background.

4.3 Results

Demographics and clinical information on the patient cohort are listed in **Supplemental Table 4.1**.

An example of an EPI and PROUD streamline visualization in a healthy subject, obtained by means of semi-automated retrospective valve tracking, is shown in **Figure 4.1**. This example is representative of a trend we observed in the healthy subject cohort. In the example, measured flow volumes are overall lower for PROUD (86.4 ± 4.2 ml/beat) than for EPI (97.1 ± 5.7 ml/beat, p = 0.05). Furthermore, in the EPI acquisition, the flow volume measured across the tricuspid valve is somewhat higher than across the other valves, whereas in the PROUD acquisition, the flow volume across the mitral valve is somewhat lower than across the other valves. **Figure 4.2** shows streamline visualizations in four different patients in whom valvular regurgitation was quantified. These examples reflect our overall findings of slightly lower regurgitant volume measurements by EPI (34.0 ± 17.6 ml/beat) than by PROUD (39.2 ± 20.1 ml/beat, p = 0.10). Valve tracking-based measurements of net flow volumes across the heart valves have been summarized in **Figure 4.3**. Group-averaged flow curves can be found in **Supplemental Figure 4.1**. In the healthy subject group, significant differences were found between EPI-based measurements of AV and TV net flow, and between PROUD-based measurements of PV and MV net flow. In the patient group, no statistically significant measurement differences were found (p = 1.00 for all valve combinations). Intervalve consistency analysis of net flow volume measurements revealed non-significant differences between PROUD and EPI in terms of CVs, both in healthy subjects (p = 0.07) and in patients (p = 0.47, **Table 4.1**). Comparing PV and AV forward flow volume quantification by 4D flow with 2D flow measurements, PROUD and EPI had similar mean differences and LOA (**Figure 4.4**). In the RVSV measurements, PROUD demonstrated slightly better agreement with 2D MRI than did EPI (**Figure 4.4**). Variability between 4D flow MRI- (EPI or PROUD) and 2D MRI-based LVSV measurements was relatively large, both in terms of mean differences and LOA (**Figure 4.4**). Mean differences and LOA between the two 4D flow techniques (**Figure 4.5**) were smaller than between 4D flow MRI (EPI or PROUD) and 2D MRI for all forward flow and stroke volume measurements (**Figure 4.4**). Likewise, regurgitant volume measurements demonstrated better agreement between the 4D flow techniques than between 4D flow and 2D MRI (**Figure 4.6**).

Table 4.1: Bland–Altman parameters of intervalve consistency in healthy subjects (top) and patients (bottom), based on valve tracking-based blood flow quantification from EPI (left) and PROUD (right) 4D flow MRI acquisitions. Results of the increasingly undersampled PROUD reconstructions are summarized below the results of the original reconstructions.

	EPI-based net flow volume			**PROUD-based net flow volume**		
Healthy subjects	**Mean diff. (ml/beat)**	**LOA width (ml/beat)**	**CV (%)**	**Mean diff. (ml/beat)**	**LOA width (ml/beat)**	**CV (%)**
AV vs. PV/MV/TV	-6.6	11.4	6.1	2.7	7.5	4.2
PV vs. AV/MV/TV	-4.5	14.8	7.9	3.7	8.2	4.6
MV vs. AV/PV/TV	2.2	12.3	6.4	-4.1	8.9	5.1
TV vs. AV/PV/MV	8.9	16.4	8.4	-2.3	10.1	5.7
Mean ± SD of absolute values	5.5±2.9	13.7±2.3	7.2±1.1	3.2±0.8	8.7±1.1	4.9±0.7
			R=9	1.9±0.8	8.6±1.6	4.8±0.9
			R=14	1.9±1.8	8.2±1.9	4.6±1.1
			R=28	5.3±1.1	13.7±4.3	7.5±2.3
			R=56	6.9±6.3	32.8±10.2	16.6±5.1
Patients						
AV vs. PV/MV/TV	0.0	15.4	10.2	-3.6	18.8	12.6
PV vs. AV/MV/TV	1.1	21.0	13.8	-1.0	13.6	9.0
MV vs. AV/PV/TV	-1.2	19.0	12.6	2.9	21.0	13.8
TV vs. AV/PV/MV	0.1	22.0	14.5	1.7	7.8	5.2
Mean ± SD of absolute values	0.6±0.6	19.3±2.9	12.8±1.9	2.3±1.2	15.3±5.9	10.2±3.9
			R=9	3.6±2.2	19.7±7.4	13.1±5.1
			R=14	2.9±2.5	20.7±9.9	13.8±6.7
			R=28	2.2±1.7	22.2±3.6	14.6±2.5
			R=56	4.3±1.4	42.9±11.0	30.0±8.1

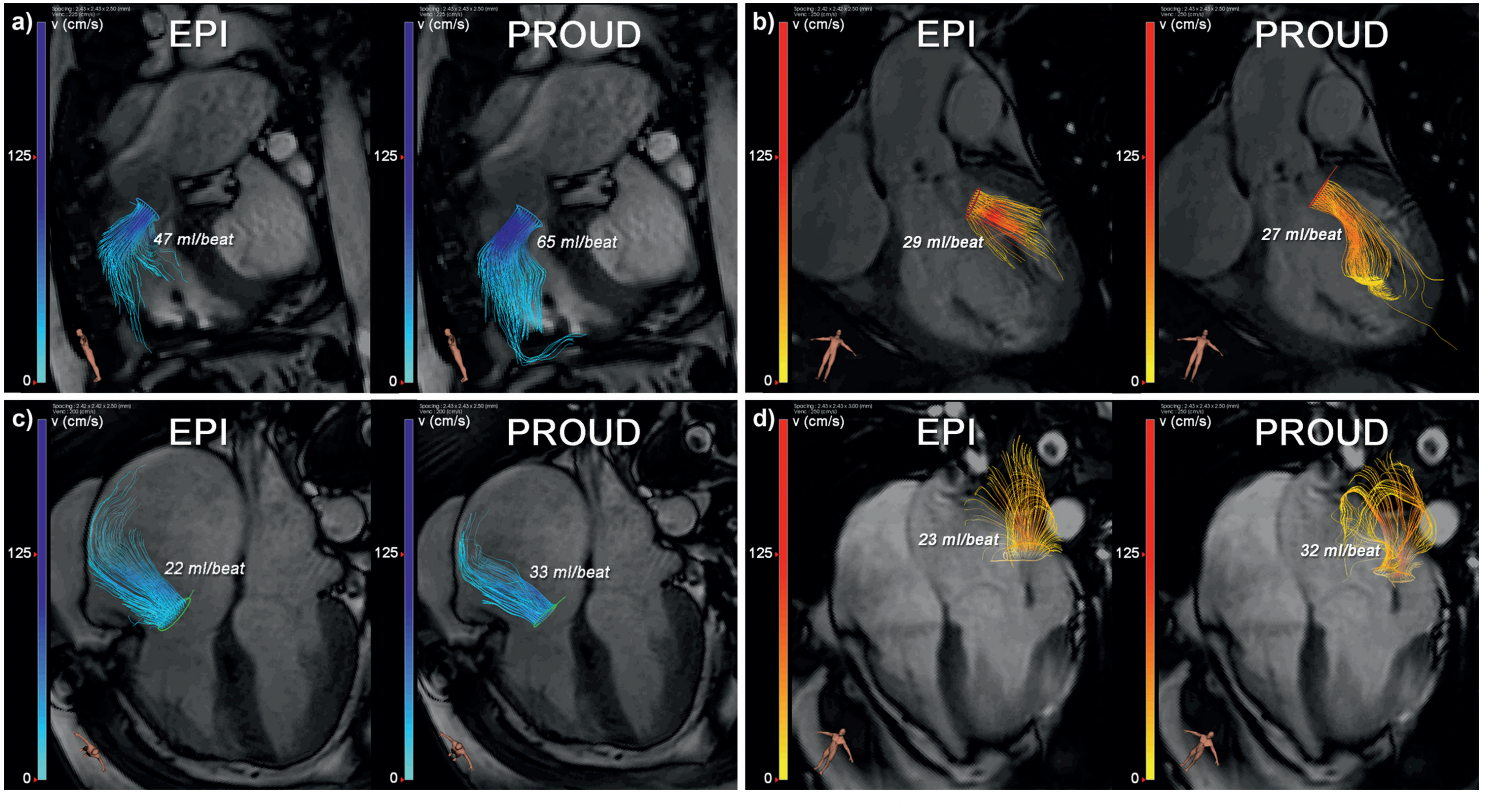

Figure 4.2: EPI and PROUD 4D flow MRI streamline visualizations in four different patients with **a)** pulmonary valve regurgitation, **b)** aortic valve regurgitation, **c)** tricuspid valve regurgitation, and **d)** mitral valve regurgitation. Semi-automated retrospective valve tracking was performed on bSSFP cine images, on two orthogonal views for each heart valve.

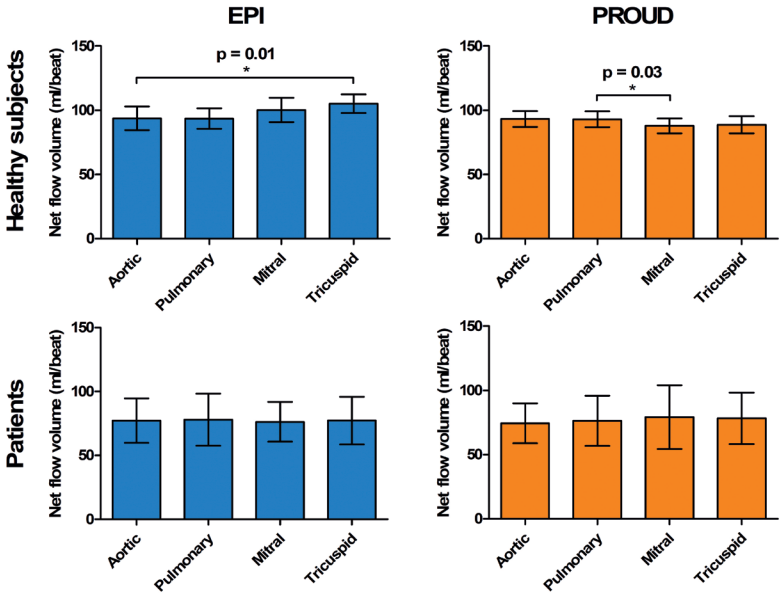

Figure 4.3: Measured net flow volume per heart valve resulting from valve tracking-based blood flow quantification from EPI (left) and PROUD (right) 4D flow MRI acquisitions, in 12 healthy subjects (top) and 8 patients with valvular regurgitation (bottom).

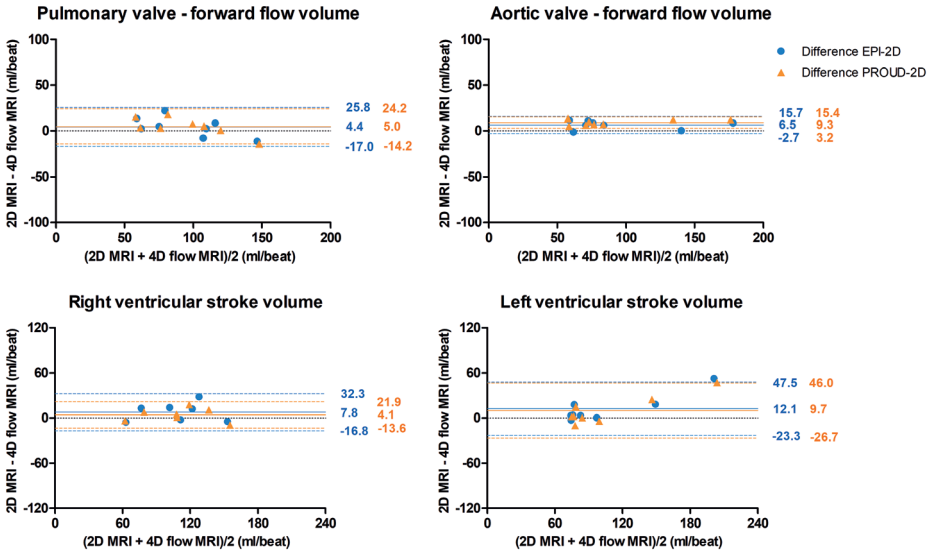

Figure 4.4: Bland–Altman comparison between 4D flow MRI (EPI = blue circles, PROUD = orange triangles) and 2D flow/bSSFP MRI measurements of PV and AV forward flow volumes (top) and RV and LV stroke volumes (bottom) in patients with valvular regurgitation.

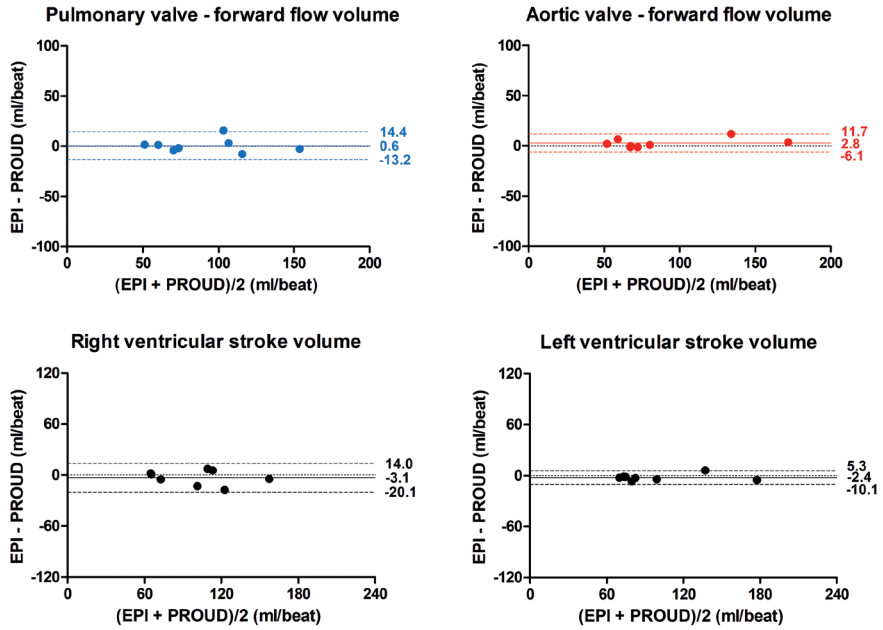

Figure 4.5: Bland–Altman comparison between EPI and PROUD 4D flow MRI measurements of PV and AV forward flow volumes (top) and RV and LV stroke volumes (bottom) in patients with valvular regurgitation.

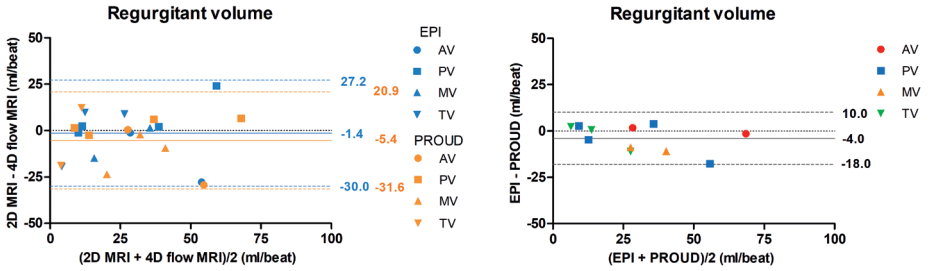

Figure 4.6: Bland–Altman comparison of regurgitant volume measurements: between 4D flow MRI (PROUD or EPI) and 2D MRI (left), and between PROUD and EPI 4D flow MRI (right). 2D MRI entailed a combination of 2D short-axis bSSFP MRI and 2D flow MRI for MV and TV regurgitant volume measurement ($Rvol_{MV}$ = LVSV – AV forward flow volume, $Rvol_{TV}$ = RVSV – PV forward flow volume). AV and PV regurgitant volumes were quantified from 2D flow MRI.

Net flow volume measurements obtained from the increasingly undersampled PROUD reconstructions demonstrated good agreement with the original reconstruction up to an undersampling factor of 14; mean differences stayed small and the coefficient of variation did not exceed 10% (**Figure 4.7**). The intervalve consistency remained

unaffected in the healthy subject group up to this undersampling factor of 14, and comparable to that of the EPI acquisition up to an undersampling factor of 28 (**Table 4.1**). In the patient group, the intervalve consistency remained comparable to that of EPI up to R=14. Valve-specific intervalve consistency parameters can be found in **Supplemental Table 4.2**. Preservation of peak velocities was excellent in the R=9 reconstructions (ICC_{PV}/ICC_{AV} = 0.94/0.96 [healthy subjects], 0.98/0.90 [patients]), and moderate to excellent in the R=14 reconstructions (ICC_{PV}/ICC_{AV} = 0.87/0.95 [healthy subjects], 0.94/0.71 [patients]) (**Figure 4.8**). Preservation of E/A ratios was good to excellent in the R=9 reconstructions (ICC_{TV}/ICC_{MV} = 0.95/0.81 [healthy subjects], 0.93/0.86 [patients]), and moderate to good in the R=14 reconstructions (ICC_{TV}/ICC_{MV} = 0.82/0.58 [healthy subjects], 0.78/0.68 [patients]) (**Figure 4.9**).

In four patients, image quality analysis was not possible because in these patients, the FOV did not contain the liver dome. In the remaining 16 subjects, significantly higher SNRs were found in the PROUD scans (14.9 ± 4.6) than in the EPI scans (11.1 ± 3.4). LLE widths were smaller for EPI (6.7 ± 3.5 voxels) than for PROUD (8.4 ± 2.2 voxels). Bland–Altman parameters of these comparisons and of those between the PROUD R=7 reconstruction and PROUD R=9, 14, 28 and 56 reconstructions can be found in **Supplemental Table 4.3**.

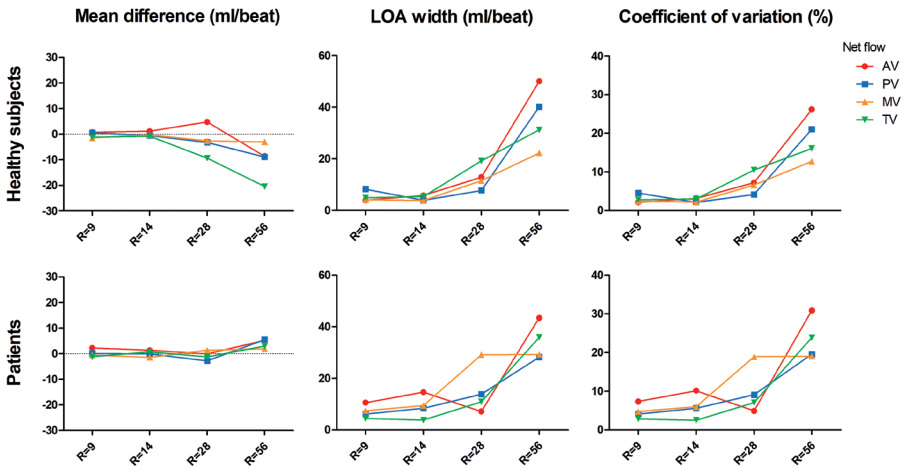

Figure 4.7: Comparison of net flow volume measurements across the aortic valve (red circles), pulmonary valve (blue squares), mitral valve (orange up-facing triangles) and tricuspid valve (green down-facing triangles) between increasingly undersampled reconstructions and the original reconstruction, based on Bland–Altman analysis.

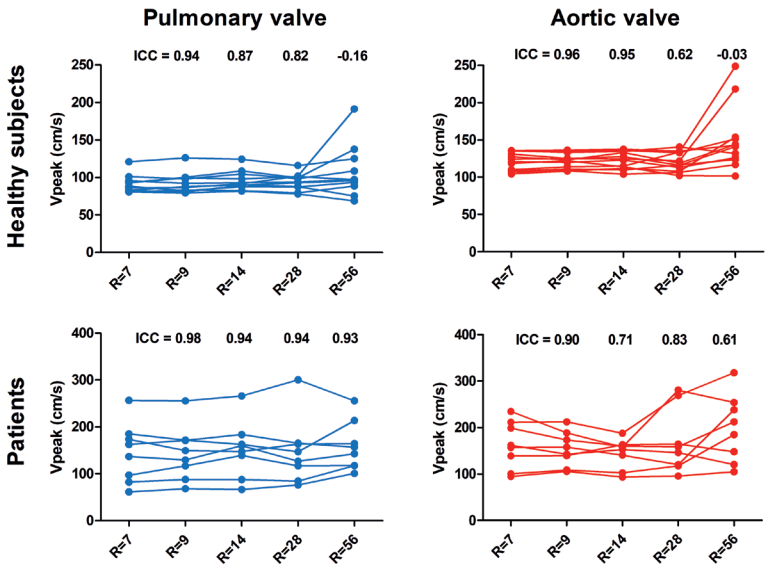

Figure 4.8: Peak velocities measured across the pulmonary (left) and aortic valve (right), in healthy subjects (top) and patients (bottom), plotted for increasing undersampling factors. Measurements in the same subject are connected by lines. Intraclass correlation coefficients (ICC) between each increasingly undersampled reconstruction and the original reconstruction are shown in the top of each plot.

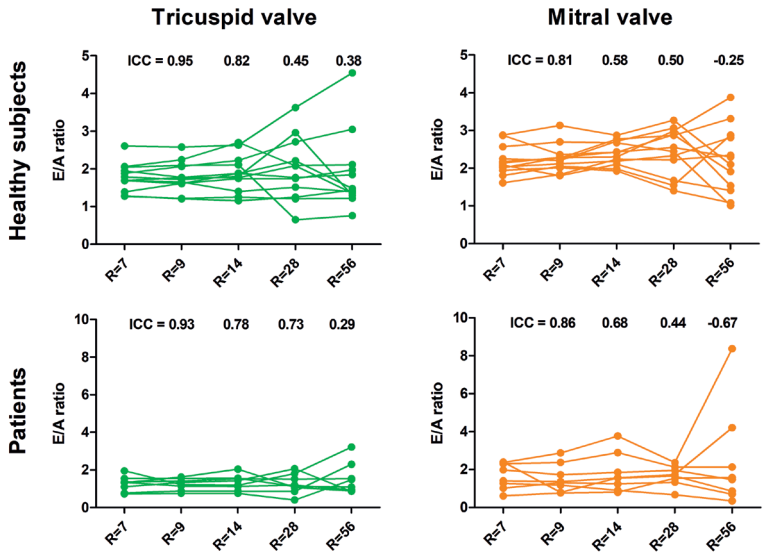

Figure 4.9: E/A ratios measured across the tricuspid (left) and mitral valve (right), in healthy subjects (top) and patients (bottom), plotted for increasing undersampling factors. Measurements in the same subject are connected by lines. Intraclass correlation coefficients (ICC) between each increasingly undersampled reconstruction and the original reconstruction are shown in the top of each plot.

4.4 Discussion

We compared pseudo-spiral undersampled whole-heart 4D flow MRI with an EPI readout sequence in a cohort of healthy subjects and patients with valvular regurgitation. Intervalve consistencies were comparable between PROUD and EPI. Agreement between the two 4D flow techniques was overall higher than between 4D flow MRI (EPI or PROUD) and 2D MRI in measurements of forward flow, stroke volumes and regurgitant volumes. The observation that increasing the undersampling factor from 7 to 14 (reducing the scan time by 50%) resulted in <10% measurement deviation from the original acquisition, and only slightly decreased intervalve consistencies, suggests that PROUD 4D flow scan times may be shortened substantially.

The finding of seemingly – although not significantly – higher intervalve consistency using PROUD 4D flow compared to EPI-based 4D flow is in line with findings of a recent multicenter study (9). The reason for this slight difference in performance can be sought in the limitations that EPI is known to have: flow displacement and phase accumulation resulting in velocity misregistration, and image distortion artefacts due to eddy currents (21,22). A detailed study on the former two limitations has shown that phase accumulation results in substantial local reductions of the effective spatial resolutions in frequency- and phase-encoding directions due to modulation of the point spread function (23). Furthermore, that study found that flow displacement in the order of several millimeters occurs in high-velocity regions. These limitations find their origin in the relatively long echo times, long readout times and unipolar phase-encoding blips that EPI requires. PROUD 4D flow is less sensitive to flow displacement than EPI because of shorter echo times, and less sensitive to phase accumulation because of a different readout strategy. Another advantage of PROUD compared to EPI is that it exploits the sparsity of the images, and can therefore recover images from highly undersampled k-space data without significant – i.e. only noise-like – artifacts (16).

Noteworthy is that the intervalve consistencies we found in the EPI and PROUD patient scans were less good than previously reported in a large-scale study using EPI (8), presumably because of a difference in severity of valvular regurgitation and valvular stenosis. The patients included in the current study had regurgitation fractions of 29.1 ± 9.6%, compared to <10% in the cited study.

Variability between 4D flow MRI- and 2D MRI-based intracardiac flow measurements has been studied before (7,10). Similar to what we observed, these studies reported that 2D flow MRI measurements of forward flow volumes were higher than those obtained with 4D flow MRI. In our study, but not in the cited studies, this may have been caused by a difference in frame rate: following the normal clinical scan protocol, 2D flow MRI was reconstructed into 40 cardiac frames as opposed to 30 in the 4D flow MRI acquisitions. In addition, the lower spatial resolutions of 4D flow MRI (2.5x2.5x2.5 mm versus 1.2x1.2x8.0 mm for 2D flow MRI) may have introduced underestimations in flow and peak velocity in patients with stenotic valves. The wide LOAs seen for the stroke volume and regurgitant volume measurements cannot be attributed to these resolution differences. We previously showed that 2D MRI-based mitral valve regurgitant volume measurements (which are based on LVSV and AV forward flow volume) are subject to substantial interobserver variability, because of differences in LVSV quantification (15), whereas 4D flow MRI-based valve tracking analysis has demonstrated good interobserver agreement (9). Furthermore, stroke volume quantification by a combination of short-axis bSSFP volumetry and 2D flow MRI is sensitive to physiological variability and the patient's ability to hold their breath. Although we had no reference standard available, the availability of four heart valves in a single whole-heart acquisition allowed for cross-comparisons that give a good idea of the overall robustness of the measurements.

In the PROUD reconstructions with different undersampling factors, peak velocities and E/A ratios were well preserved up to an undersampling factor of 9 (using 75% of the initially acquired data). These parameters contain important and clinically used hemodynamic information, and measurement accuracy should not be sacrificed in favor of a higher undersampling factor. Therefore, these parameters should be taken into account when deciding on the maximum undersampling factor in whole-heart 4D flow MRI.

The EPI acquisition had a higher total acceleration factor (10: EPI factor 5, SENSE factor 2) than the PROUD acquisition (factor 7) for approximately the same acquisition time. In some of the test scans we obtained with the EPI sequence – prior to data acquisition for this study – intravoxel phase dispersion artefacts were present at the borders of the ascending aorta and main pulmonary artery lumen. Changing the phase-encoding direction from anterior-posterior to right-left provided a solution, with the drawback of longer scan times for the same field of view, which is why the EPI acceleration factor

had to be set higher. One could argue that the acceleration factors should be equal for a fair comparison. However, since the scan time is ultimately decisive for clinical applicability, we decided to focus on scan times rather than on acceleration factors. Moreover, our results indicated that even for an undersampling factor of 28 in healthy subjects and 14 in patients, PROUD still had comparable intervalve consistency to EPI.

4.4.1 Limitations

The sample sizes of the healthy subject and patient groups were small and unequal. All results were presented for the two groups separately, but drawing conclusions on how the group-specific results relate to each other is difficult. In the intervalve consistency tests, smaller mean biases, but larger LOAs were observed in the patient group which can be partly explained by higher VENCs – and thus lower velocity-to-noise ratios. A difference in BMI may also have played a role: more surrounding tissue can lead to a lower signal-to-noise ratio. Moreover, irregular breathing such as apnoeas, hypopnoeas and variability in breathing frequency and depth are linked to volume overload heart failure and poor left ventricular function and cannot be ruled out as another reason for larger LOAs in the patient group (24,25). No respiratory compensation or correction was performed in the 4D flow MRI acquisitions, as this is standard for the use of EPI 4D flow for intracardiac flow quantification. Moreover, scan times had to be kept predictable at ~9 minutes to be able to perform both 4D flow scans within the allotted time. However, respiratory compensation has been shown to improve image sharpness in PROUD scans, and to have a small effect on flow measurements across the tricuspid and pulmonary valve compared to no respiratory gating (19).

Another limitation is that no short-axis bSSFP and 2D flow MRI were performed in the healthy subjects. Since the scans were not vital for the valve tracking analyses, they were omitted to save enough time for the two 4D flow MRI scans.

4.4.2 Conclusion

Our results indicate that whole-heart 4D flow MRI using pseudo-spiral Cartesian sampling with random undersampling in time (PROUD) and compressed sensing reconstruction is a reliable technique for intracardiac flow quantification in <10 minutes. Even for 75% shorter scan times in healthy subjects and 50% shorter scan times in patients with valvular regurgitation, PROUD intervalve consistencies of flow measurements across the heart valves remain comparable to those of EPI. The current study adds to previous studies that have demonstrated the robustness of PROUD-

accelerated 4D flow MRI in other cardiovascular structures (11–13). For application in different cardiac pathologies than valvular regurgitation, separate investigation is warranted.

4.5 Material availability statement

PROUD 4D flow data were acquired using our in-house developed Amsterdam UMC "PROspective Undersampling in multiple Dimensions" patch. A compiled version of this patch is available on reasonable request.

4.6 Supplemental material

Supplemental Table 4.1: Patient cohort demographics and clinical indications.

Cohort-averaged demographics	
Age (y)	39 ± 18
Sex (M/F)	5/3
Weight (kg), median [Q1; Q3]	74.0 [60.3; 92.8]
LVEF (%)	59.3 ± 8.2
RVEF (%)	59.4 ± 7.0
Regurgitation fraction (%)	29.1 ± 9.6

Subject-specific clinical indications for MRI scan
1. Loeys Dietz syndrome, mitral and tricuspid valve insufficiency
2. Aortic valve insufficiency
3. Corrected atrioventricular septal defect, mitral valve insufficiency
4. Tetralogy of Fallot, pulmonary valve stenosis and insufficiency
5. Pulmonary valve replacement and insufficiency, tricuspid valve replacement and insufficiency
6. Pulmonary valve insufficiency after balloon angioplasty
7. Aortic valve insufficiency
8. Pulmonary valve insufficiency after valvulotomy

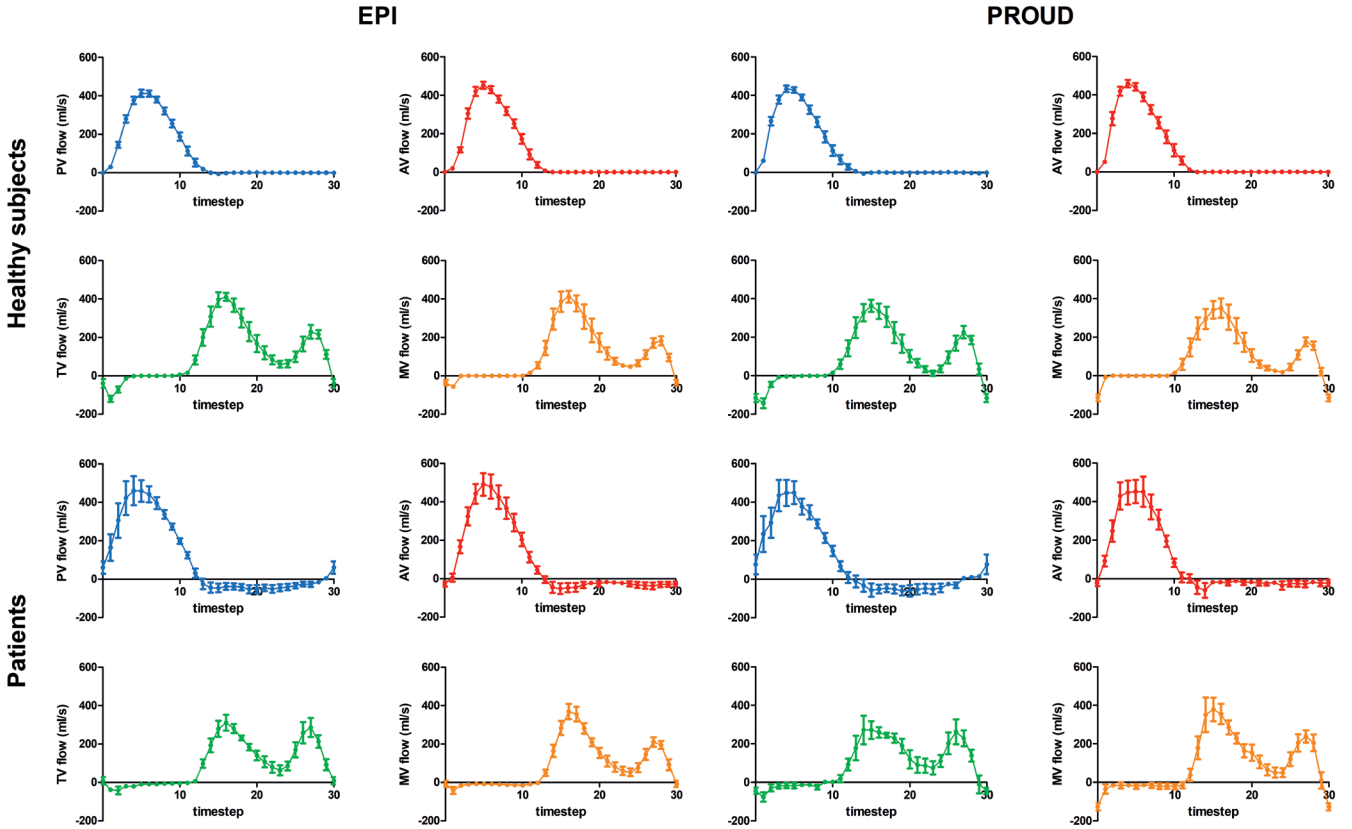

Supplemental Figure 4.1: Subject-averaged flow curves of valve tracking-based measurements across the pulmonary valve (blue), aortic valve (red), tricuspid valve (green) and mitral valve (orange), by EPI (left) and PROUD (right) 4D flow MRI in healthy subjects (top) and patients with valvular regurgitation (bottom).

Supplemental Table 4.2: Bland–Altman parameters of intervalve consistency based on PROUD net flow measurements from the increasingly undersampled reconstructions (R=9, 14, 28, 56).

	PROUD-based net flow volume, R=9			PROUD-based net flow volume, R=14		
Healthy subjects	**Mean diff. (ml/beat)**	**LOA width (ml/beat)**	**CV (%)**	**Mean diff. (ml/beat)**	**LOA width (ml/beat)**	**CV (%)**
AV vs. PV/MV/TV	1.1	6.3	3.6	0.3	6.0	3.4
PV vs. AV/MV/TV	2.6	10.1	5.7	3.6	7.9	4.4
MV vs. AV/PV/TV	-2.5	8.5	4.8	-3.3	8.3	4.7
TV vs. AV/PV/MV	-1.3	9.4	5.3	-0.6	10.7	6.0
Mean±SD of abs. values	1.9±0.8	8.6±1.6	4.8±0.9	1.9±1.8	8.2±1.9	4.6±1.1
Patients						
AV vs. PV/MV/TV	-6.4	29.4	19.9	-5.2	33.5	22.6
PV vs. AV/MV/TV	-0.9	19.3	12.8	-0.6	19.8	13.1
MV vs. AV/PV/TV	3.8	18.4	12.1	4.9	19.9	13.0
TV vs. AV/PV/MV	3.5	11.6	7.6	0.9	9.5	6.3
Mean±SD of abs. values	3.6±2.2	19.7±7.4	13.1±5.1	2.9±2.5	20.7±9.9	13.8±6.7

	PROUD-based net flow volume, R=28			PROUD-based net flow volume, R=56		
Healthy subjects	**Mean diff. (ml/beat)**	**LOA width (ml/beat)**	**CV (%)**	**Mean diff. (ml/beat)**	**LOA width (ml/beat)**	**CV (%)**
AV vs. PV/MV/TV	-6.2	15.2	8.5	2.6	47.9	24.0
PV vs. AV/MV/TV	4.2	10.0	5.4	0.8	26.4	13.3
MV vs. AV/PV/TV	-4.5	10.5	5.8	-13.9	30.5	15.9
TV vs. AV/PV/MV	6.4	19.1	10.3	10.5	26.5	13.0
Mean±SD of abs. values	5.3±1.1	13.7±4.3	7.5±2.3	6.9±6.3	32.8±10.2	16.6±5.1
Patients						
AV vs. PV/MV/TV	-4.3	26.5	17.7	-5.3	59.0	41.9
PV vs. AV/MV/TV	1.8	19.1	12.4	-3.2	35.0	24.7
MV vs. AV/PV/TV	0.1	23.7	15.6	5.6	40.6	27.8
TV vs. AV/PV/MV	2.4	19.5	12.7	2.9	37.0	25.5
Mean±SD of abs. values	2.2±1.7	22.2±3.6	14.6±2.5	4.3±1.4	42.9±11.0	30.0±8.1

Supplemental Table 4.3: Bland–Altman parameters of image quality comparisons between PROUD and EPI, and between PROUD R=9, 14, 28 and 56 and PROUD R=7, based on signal-to-noise ratio and lung-liver edge width. An asterisk indicates a statistical difference.

	Signal-to-noise ratio			Lung-liver edge width		
All subjects	**Mean diff.**	**LOA width**	**CV (%)**	**Mean diff. (voxels)**	**LOA width (voxels)**	**CV (%)**
PROUD vs. EPI	-3.8*	8.5	33.2	-1.8*	4.4	29.7
PROUD R=9 vs. R=7	0.2	2.7	9.2	-0.1	0.8	4.7
PROUD R=14 vs. R=7	1.7*	4.1	14.8	0.0	1.3	7.8
PROUD R=28 vs. R=7	3.8*	3.8	15.1	-0.1	2.1	12.6
PROUD R=56 vs. R=7	6.6*	6.2	27.2	-0.4	3.2	19.1

*. Indicates a significant difference at the .05 level

4.7 References

1. Markl M, Frydrychowicz A, Kozerke S, Hope M, Wieben O. 4D flow MRI. J Magn Reson Imaging. 2012;36(5):1015–1036.
2. Ha H, Kim GB, Kweon J, et al. Hemodynamic measurement using four-dimensional phase-contrast MRI: Quantification of hemodynamic parameters and clinical applications. Korean J Radiol. 2016;17(4):445–462.
3. Geiger J, Hirtler D, Bürk J, et al. Postoperative pulmonary and aortic 3D haemodynamics in patients after repair of transposition of the great arteries. Eur Radiol. 2014;24(1):200–208.
4. van der Palen RLF, Westenberg JJM, Hazekamp MG, Kuipers IM, Roest AAW. Four-dimensional flow cardiovascular magnetic resonance for the evaluation of the atrial baffle after Mustard repair. Eur Hear J – Cardiovasc Imaging. 2016;17(3):353–353.
5. Geiger J, Markl M, Jung B, et al. 4D-MR flow analysis in patients after repair for tetralogy of Fallot. Eur Radiol. 2011;21(8):1651–1657.
6. Sjöberg P, Bidhult S, Bock J, et al. Disturbed left and right ventricular kinetic energy in patients with repaired tetralogy of Fallot: pathophysiological insights using 4D-flow MRI. Eur Radiol. 2018;28(10):4066–4076.
7. Hsiao A, Tariq U, Alley MT, Lustig M, Vasanawala SS. Inlet and outlet valve flow and regurgitant volume may be directly and reliably quantified with accelerated, volumetric phase-contrast MRI. J Magn Reson Imaging. 2015;41(2):376–385.
8. Kamphuis VP, Roest AAW, Ajmone Marsan N, et al. Automated Cardiac Valve Tracking for Flow Quantification with Four-dimensional Flow MRI. Radiology. 2019;290(1):70–78.
9. Juffermans JF, Minderhoud SCS, Wittgren J, et al. Multicenter Consistency Assessment of Valvular Flow Quantification With Automated Valve Tracking in 4D Flow CMR. JACC Cardiovasc Imaging. 2021;14(7):1354–1366.
10. Garg P, Westenberg JJM, van den Boogaard PJ, et al. Comparison of fast acquisition strategies in whole-heart four-dimensional flow cardiac MR: Two-center, 1.5 Tesla, phantom and in vivo validation study. J Magn Reson Imaging. 2018;47(1):272–281.
11. Gottwald LM, Peper ES, Zhang Q, et al. Pseudo-spiral sampling and compressed sensing reconstruction provides flexibility of temporal resolution in accelerated aortic 4D flow MRI: A comparison with k-t principal component analysis. NMR Biomed. 2020;33(4):e4255.
12. Peper ES, Gottwald LM, Zhang Q, et al. Highly accelerated 4D flow cardiovascular magnetic resonance using a pseudo-spiral Cartesian acquisition and compressed sensing reconstruction for carotid flow and wall shear stress. J Cardiovasc Magn Reson. 2020;22(1):7.
13. Gottwald LM, Töger J, Markenroth Bloch K, et al. High Spatiotemporal Resolution 4D Flow MRI of Intracranial Aneurysms at 7T in 10 Minutes. Am J Neuroradiol. 2020;41(7):1201–1208.
14. Westenberg JJM, Roes SD, Ajmone Marsan N, et al. Mitral Valve and Tricuspid Valve Blood Flow: Accurate Quantification with 3D Velocity-encoded MR Imaging with Retrospective Valve Tracking. Radiology. 2008;249(3):792–800.
15. Blanken CPS, Westenberg JJM, Aben J-P, et al. Quantification of Mitral Valve Regurgitation from 4D Flow MRI Using Semiautomated Flow Tracking. Radiol Cardiothorac Imaging. 2020;2(5):e200004.
16. Lustig M, Donoho D, Pauly JM. Sparse MRI: The application of compressed sensing for rapid MR imaging. Magn Reson Med. 2007;58(6):1182–1195.
17. Jaspan ON, Fleysher R, Lipton ML. Compressed sensing MRI: a review of the clinical literature. Br J Radiol. 2015;88(1056):20150487.
18. Loecher M, Schrauben E, Johnson KM, Wieben O. Phase unwrapping in 4D MR flow with a 4D single-step laplacian algorithm. J Magn Reson Imaging. 2016;43(4):833–842.

19. Gottwald LM, Blanken CPS, Tourais J, et al. Retrospective Camera-Based Respiratory Gating in Clinical Whole-Heart 4D Flow MRI. J Magn Reson Imaging. 2021;54(2):440–451.
20. Koo TK, Li MY. A Guideline of Selecting and Reporting Intraclass Correlation Coefficients for Reliability Research. J Chiropr Med. 2016;15(2):155–163.
21. Butts K, Riederer SJ. Analysis of flow effects in echo-planar imaging. J Magn Reson Imaging. 1992;2(3):285–293.
22. Fischer H, Ladebeck R. Echo-Planar Imaging Image Artifacts. Echo-Planar Imaging. 1998;179–200.
23. Dillinger H, Walheim J, Kozerke S. On the limitations of echo planar 4D flow MRI. Magn Reson Med. 2020;84(4):1806–1816.
24. Feld H, Priest S. A cyclic breathing pattern in patients with poor left ventricular function and compensated heart failure: A mild form of cheyne-stokes respiration? J Am Coll Cardiol. 1993;21(4):971–974.
25. Toledo C, Andrade DC, Díaz HS, et al. Rostral ventrolateral medullary catecholaminergic neurones mediate irregular breathing pattern in volume overload heart failure rats. J Physiol. 2019;597(24):5799–5820.

Retrospective Camera-Based Respiratory Gating in Clinical Whole-Heart 4D Flow MRI

5

Lukas M. Gottwald
Carmen P.S. Blanken
João Tourais
Jouke Smink
R. Nils Planken
S. Matthijs Boekholdt
Lilian J. Meijboom
Bram F. Coolen
Gustav J. Strijkers
Aart J. Nederveen
Pim van Ooij

J. Magn. Reson. Imaging 2021; 54: 440-451.

Abstract

Background

Respiratory gating is generally recommended in 4D flow MRI of the heart to avoid blurring and motion artifacts. Recently, a novel automated contactless camera-based respiratory motion sensor was introduced.

Purpose

To compare camera-based respiratory gating (CAM) with lung-liver navigator-based gating (NAV) and no gating (NO) for whole-heart 4D flow MRI.

Study type

Retrospective.

Subjects

Thirty-two patients with a spectrum of cardiovascular diseases.

Field strength/sequence

A 3T, 3D-cine spoiled gradient-echo T1-weighted sequence with flow encoding in three spatial directions.

Assessment

Respiratory phases were derived and compared against each other by cross-correlation. Three radiologists/cardiologists scored images reconstructed with camera-based, navigator-based, and no respiratory gating with a 4-point Likert scale (qualitative analysis). Quantitative image quality analysis, in the form of signal-to-noise ratio (SNR) and lung-liver edge width (LLE) for sharpness and quantitative flow analysis of the valves were performed semi-automatically.

Statistical tests

One-way repeated measures analysis of variance (ANOVA) with Wilks' λ testing and follow-up pairwise comparisons. Significance level of $p \leq 0.05$. Krippendorff's alpha test for inter-rater reliability.

Results

The respiratory signal analysis revealed that CAM and NAV phases were highly correlated ($C = 0.93 \pm 0.09$, $p < 0.01$). Image scoring showed poor inter-rater reliability and no significant differences were observed ($p \geq 0.16$). The image quality comparison showed that NAV and CAM gating were superior to NO with higher SNR ($p = 0.02$) and smaller LLE ($p < 0.01$). The quantitative flow analysis showed significant differences between the three respiratory-gated reconstructions in the tricuspid and pulmonary valves ($p \leq 0.05$), but not in the mitral and aortic valves ($p > 0.05$). Pairwise comparisons showed that reconstructions without respiratory gating were different in flow measurements to either CAM or NAV or both, but no differences were found between CAM and NAV reconstructions.

Conclusions

Camera-based respiratory gating performed as well as conventional lung-liver navigator-based respiratory gating. Quantitative image quality analysis showed that both techniques were equivalent and superior to no-gating reconstructions. Quantitative flow analysis revealed local flow differences (tricuspid/pulmonary valves) in images of no-gating reconstructions, but no differences were found between images reconstructed with camera-based and navigator-based respiratory gating.

5.1 Introduction

Whole-heart 4D flow MRI is an emerging technique with important application in diagnosis and risk assessment of structural heart diseases via quantification of hemodynamic parameters and intracardiac flow visualization (1–6). To avoid blurring and motion artifacts, respiratory gating is generally recommended in 4D flow MRI (1,2,7).

Several methods have been developed to track patient breathing during image acquisition. The 4D flow consensus statement paper recommends the use of a belt or a navigator (1,8). The latter involves additional radiofrequency pulses to dynamically track the anatomic motion of usually the lung-liver boundary (1,8). Another option is self-navigation (9–12), in which the respiratory motion information is calculated from the MRI acquisition itself if the k-space sampling was performed in a certain order and a frequency high enough to capture the respiratory motion. However, this is not the case for standard Cartesian 4D flow sequences which are usually used in clinical practice, and, therefore, self-navigation cannot be applied there. In some cases, respiratory gating can be omitted with acceptable quantitative results and image quality (13–15). However, higher-resolution 4D flow MRI requires accurate and reliable respiratory gating (7).

Respiratory motion information can be used in a prospective or retrospective manner to acquire or accept data only during a time window of minimal respiration-induced motion, usually at end-expiration. Prospective gating has the drawback that the scan time is not exactly known *a priori* and may increase significantly in case of low respiratory gating efficiency (16). Retrospective gating requires sufficient oversampling of the data to ensure that enough k-space points are acquired for reconstruction. The need for oversampling can be reduced by employing efficient k-space acquisition strategies, including radial or spiral readouts and appropriate reconstruction techniques such as compressed sensing (10,17,18).

Recently, a novel automated contactless camera-based respiratory motion sensor has been introduced (19,20). The input video signal is divided into equal-sized rectangular blocks, then the blocks containing periodic respiratory motion are identified, weighted, and used to track respiratory motion. This gating technique is easy to use as it requires no additional manual steps such as belt placement or sequence planning and can be

used for prospective or retrospective triggering. Harder et al. have demonstrated improved image quality in abdominal MRI with prospective camera-based respiratory gating compared to belt-based respiratory gating (21), which evoked the question of how this technique performs in 4D flow MRI.

This study aimed to evaluate camera-based retrospective respiratory gating for whole-heart 4D flow MRI in patients with cardiovascular diseases.

5.2 Methods

5.2.1 Study cohort

The study cohort consisted of 32 patients (34 ± 18 years, range 9–73 years; 17 male/15 female). Included were all patients that underwent a whole-heart 4D flow MRI exam between September 2019 and March 2020. This group of patients had a spectrum of cardiovascular diseases, including valvular heart disease, aortic disease, and complex structural heart disease (see **Supplemental Table 5.1**). The study design was retrospective and data analysis was anonymous, so the requirement for written informed consent was waived by the local ethics committee. Exclusion criteria for quantitative flow analysis were: the field of view did not contain the entire heart, the standard clinical 2D cine images were missing or were of insufficient quality to contour the valves.

5.2.2 Data acquisition

All MRI data sets were acquired with a dStream Torso coil on a 3T MR system (Philips Ingenia ElitionX; Philips Medical Systems). In the standard clinical routine protocol of mainly 2D cine MRI scans, a pseudo-spiral compressed sensing accelerated 4D flow MRI scan was performed for each patient (17,22). All MRI scans were synchronized with the heartbeat by electrocardiography-based gating. 4D flow MRI scans were acquired with a gradient-echo sequence undersampled by a factor of 7.1. Scan parameters were echo time / repetition time / flip angle of 2.0 ms / 4.0 ms / 8, acquisition and reconstruction voxel size of 2.5 mm isotropic, and velocity encoding in the range of 150 to 250 cm/s. Acceleration factor, scan time as well as temporal resolution was calculated as a mean over the study cohort.

Respiratory motion was measured simultaneously by the conventional lung-liver navigator and a camera sensor (VitalEye, Philips Medical Systems) as shown in **Figure 5.1**. The navigator was placed on the lung-liver border. The MRI data acquisition was modified for this 4D flow protocol to acquire pencil beam navigators with a sampling frequency of 2 Hz regardless of the cardiac cycle. A built-in-the-bore camera (uEye, IDS Imaging Development Systems) targeted the upper body, and a fully automated algorithm derived the respiratory signal in real-time by identifying image blocks that contained the respiratory motion. The camera-based respiratory signal was streamed to the scanner with a sampling frequency of 20 Hz (19).

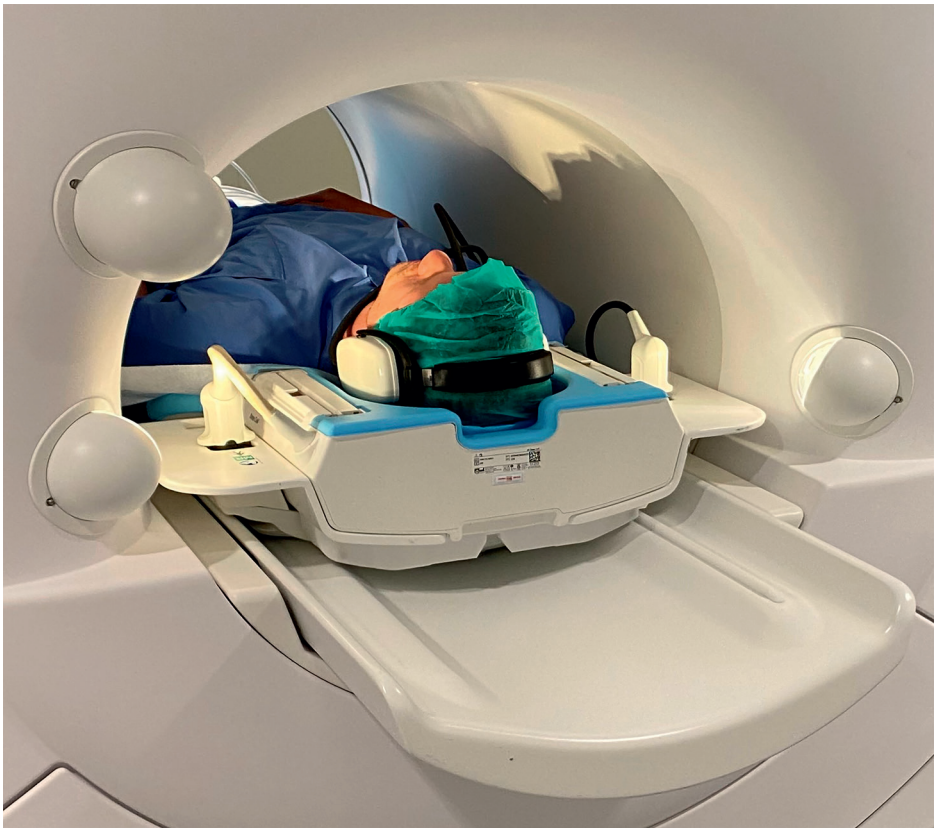

Figure 5.1: Impression of the built-in-the-bore vital sign camera (VitalEye, Philips Medical Systems). The camera is inside the top left plastic casing and focusses on the subject's upper body. The other two plastic casings on table height are spotlights. Usage of a head coil instead of a body coil was for demonstration purposes only.

5.2.3 Respiratory binning and data reconstruction

4D flow data were reconstructed offline using ReconFrame (Gyrotools) in MATLAB (MathWorks) together with the Berkeley Advanced Reconstruction Toolbox (23) for compressed sensing reconstruction with a sparsifying total variation transform in time (18,22). Apart from retrospective cardiac gating, camera-based respiratory gating (CAM) and navigator-based respiratory gating (NAV) of the raw data was performed with respiratory phase binning in inspiration and expiration. The phase binning algorithm is explained in detail in the Appendix. The expiration phase acceptance was defined at 60% (24). Additionally, all 4D flow data sets were also reconstructed with no respiratory gating (NO) representing 100% respiratory phase acceptance. The cardiac cycle was binned into 30 frames. After the reconstruction, phase unwrapping (velocity aliasing correction) of the 4D flow data was automatically performed with a 4D single-step Laplacian algorithm (25).

5.2.4 Respiratory signal analysis

After the respiratory binning in the reconstruction, the respiratory signals, as well as their corresponding respiratory phases, were extracted from both CAM and NAV. The cross-correlation of the respiratory phases per subject was calculated to evaluate their similarity. Furthermore, the time shift between the two phases (phase delay) was measured.

5.2.5 Qualitative image analysis

Qualitative image analysis was performed independently and blinded by a radiologist with 15 years (RNP), a cardiothoracic radiologist with 8 years (LJM), and a cardiologist with 10 years (SMB) of experience in cardiovascular imaging. Images were provided as transversal magnitude and phase-contrast cine images at two locations. One location was intersecting the heart chambers and the other was intersecting the great vessels. Image scoring was based on a 4-point Likert scale: 1 = unusable, 2 = fair, 3 = good, 4 = excellent. Rated were four categories: anatomical structure, flow signal, breathing artifacts, and flow artifacts.

5.2.6 Quantitative image analysis

Quantitative image analysis was performed using the phase-contrast magnitude images by calculating the signal-to-noise ratio (SNR) and the lung-liver edge width (LLE) from a 10x10x30 voxel region-of-interest (ROI). The ROI was manually drawn per patient at the lung-liver border at the expected location of the navigator. In this

ROI two transversal slices were selected: one in the liver and another in the lung. The slice in the liver was defined as the signal area and the slice in the lung was defined as the noise area. SNR was defined as the time-averaged mean signal intensity divided by the time-averaged standard deviation of the noise. Between the liver and the lung slice in the ROI, 100 line profiles in z-direction were extracted and fitted on a sigmoid function. LLE was defined by the mean width $\bar{d}$ of all sigmoid functions [voxels].

5.2.7 Quantitative flow analysis

The reconstructed velocity images were processed in Cardiovascular Angiographic Analysis Systems (CAAS; MR Solutions version 5.1 - 4D flow, Pie Medical Imaging) to analyze the blood flow across the tricuspid valve (TV), pulmonary valve (PV), mitral valve (MV), and aortic valve (AV). The 2D cine images were used to mark all cardiac valves and track their motion (26). The 2D cine and 4D flow MRI images were aligned, and contours were drawn to measure the blood flow across all four heart valves. As parameters of interest, forward flow volume [ml/beat], backward flow volume [ml/beat], regurgitation fraction (27), and velocity [cm/s] (mean of the contour per time point) per valve were chosen. Moreover, backward flow volumes and regurgitation fractions were compared of a mixed subgroup n_2 containing only valves diagnosed with regurgitation.

5.2.8 Statistical analysis

For each sub-analysis, a one-way repeated measures analysis of variance (ANOVA) was conducted to evaluate the null hypothesis that there is no change between the three different respiratory gating techniques (CAM, NAV, and NO). Level of significance was defined at $p < 0.05$. Pairwise comparisons were Bonferroni-corrected. The Krippendorff's alpha test for ordinal data was used to estimate the inter-rater reliability alpha (α) for the Likert scoring in the qualitative image analysis (28). Values were reported as mean ± standard deviation. Additionally, pairwise comparisons for the quantitative image and flow analyses were presented in the form of Bland–Altman plots.

5.3 Results

5.3.1 Study cohort and data acquisition

The average scan time was 586 ± 103 s, ranging from 397 to 757 s, depending on the field of view needed to cover the patient's heart. Retrospective cardiac binning into 30 frames resulted in a temporal resolution of 28.0 ± 4.7 ms, corresponding to acceleration factors of 10.73 ± 1.08 for CAM, 10.74 ± 1.07 for NAV, and 6.89 ± 0.81 for NO. Nine data sets were excluded from the quantitative flow analysis due to exclusion criteria. The remaining subset n_1 consisted of 23 patients (30 ± 16 years, range 9–73 years; 12 male/11 female). A detailed overview of the patient cohort is provided in **Supplemental Table 5.1**.

5.3.2 Respiratory signal analysis

The respiratory signal analysis revealed that the camera- and navigator-derived respiratory phases were highly correlated as their cross-correlation was C_{phase} = 0.93 ± 0.09 ($p < 0.01$). The significance was tested for the hypothesis that the cross-correlation is <0.5 (no strong correlation). The corresponding phase delay between the camera and navigator phase was d_{phase} = 0 ± 63 ms. In **Figure 5.2**, respiratory signal samples of two patients are shown for CAM and NAV. Both patients' CAM signals have similar ranges, but their NAV signal amplitude ranges differ approximately by a factor of 3. Zoomed regions of the respiratory signals are shown in the middle plots, and the corresponding respiratory phases show high correlation after binning on the bottom plots. **Supplemental Figure 5.1** contains both the CAM and NAV signals for all patients as well as signal boxplots over the entire cohort. Calculated in the boxplots were the inter-quartile ranges, upper and lower whiskers (W_{up}, W_{low}) as well as minima and maxima. While the ratio of $(W_{up}–W_{low})_{CAM}/(W_{up}–W_{low})_{NAV}$ was 87, the ratio of $(\text{maxima}–\text{minima})_{CAM}/(\text{maxima}–\text{minima})_{NAV}$ was 161, highlighting the signal amplitude differences from the outliers, which are not noticeable after phase binning.

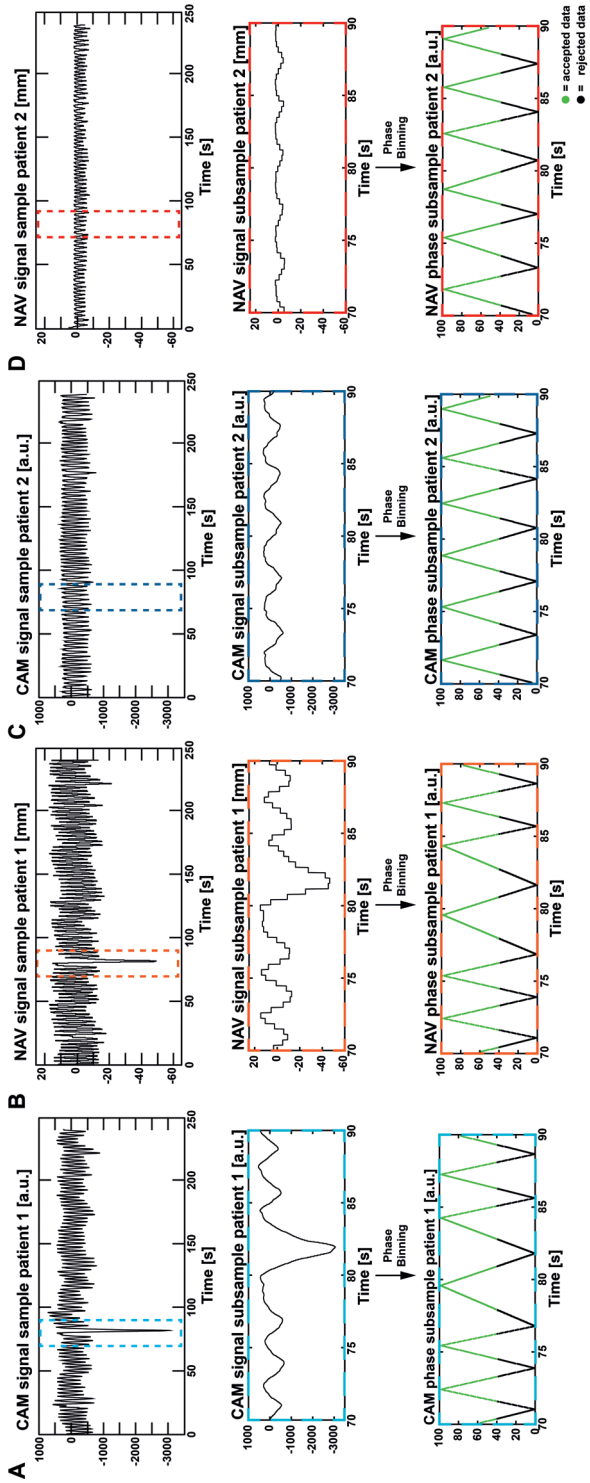

Figure 5.2: Respiratory signal samples (top) of two patients for both CAM (A, C) and NAV (B, D) are illustrated. Zoomed regions of the respiratory signals are shown in the middle with the corresponding respiratory phases after phase binning on the bottom. Green respiratory phases indicate accepted data points.

5.3.3 Qualitative image analysis

Image samples of 4D flow data sets reconstructed with NAV, CAM, and NO are shown in **Figure 5.3**. No significant differences between the three reconstructions could be found for anatomical structure (Wilks' $\lambda = 0.99$, $F(2,92) = 0.44$, $p = 0.65$, $\eta^2 = 0.01$), flow signal (Wilks' $\lambda = 0.96$, $F(2,92) = 1.86$, $p = 0.16$, $\eta^2 = 0.04$), breathing artifacts (Wilks' $\lambda = 1.00$, $F(2,92) = 0.50$, $p = 0.95$, $\eta^2 = 0.001$), and flow artifacts (Wilks' $\lambda = 0.99$, $F(2,92) = 0.41$, $p = 0.66$, $\eta^2 = 0.01$. Inter-rater reliability was low for all categories, i.e., anatomical structure with $\alpha = 0.46$, flow signal with $\alpha = 0.24$, breathing artifacts with $\alpha = 0.39$, and flow artifacts with $\alpha = 0.24$. All pairwise comparisons are listed in **Supplemental Table 5.2** and illustrated in **Supplemental Figure 5.2**.

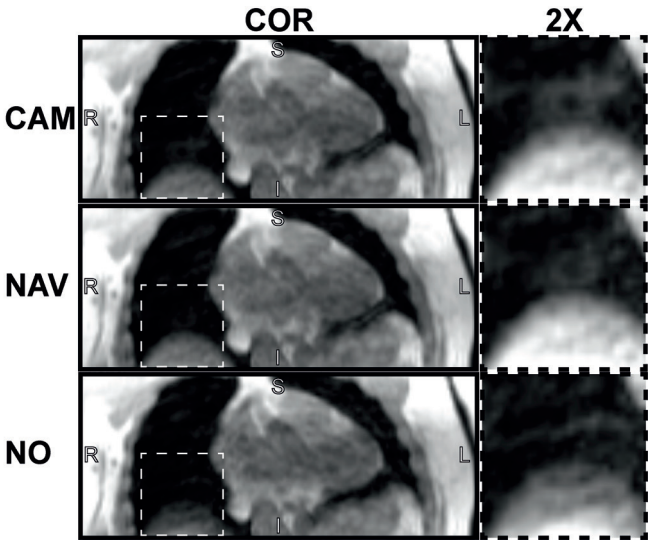

Figure 5.3: Samples of coronal images with camera-based (CAM), navigator-based (NAV), and no respiratory gating (NO). A region (dotted box) around the lung-liver border is two-fold magnified on the right.

5.3.4 Quantitative image analysis

The quantitative image quality comparison, illustrated in **Figure 5.4**, showed that reconstructions with NAV and CAM were superior to NO in terms of SNR (Wilks' $\lambda = 0.77$, $F(2,92) = 4.63$, $p = 0.02$, $\eta^2 = 0.24$), as well as LLE (Wilks' $\lambda = 0.40$, $F(2,92) = 22.31$, $p < 0.01$, $\eta^2 = 0.60$). Follow-up pairwise comparisons indicated no significant differences for NAV-vs-CAM in SNR ($p = 1.0$) and LLE ($p = 1.0$), whereas the comparison of CAM-vs-NO as well as NAV-vs-NO showed a significant difference for SNR of 1.69 ± 0.57 ($p = 0.02$) and 1.53 ± 0.51 ($p = 0.02$), and LLE of -1.82 ± 0.29 voxels

($p < 0.01$) and –1.80 ± 0.27 voxels ($p < 0.01$). An example of an increased LLE for NO compared to CAM and NAV is shown in **Figure 5.3**, in which the larger LLE is visible in the blurred lung-liver border. The SNR and LLE pairwise comparisons are listed in **Table 5.1** and illustrated in **Supplemental Figure 5.3**.

Table 5.1: Pairwise comparisons of quantitative image quality analysis.

X	Y	Mean Diff. (X-Y)	Standard Error	Significance[a]	95% Confidence Interval for Diff.[a]	
					Lower Bound	Upper Bound
SNR [ ], N = 32						
CAM	NAV	0.15	0.28	1.00	-0.56	0.87
	NO *	1.69	0.57	0.02	0.24	3.13
NAV	CAM	-0.15	0.28	1.00	-0.87	0.56
	NO *	1.53	0.51	0.02	0.25	2.82
NO	CAM *	-1.69	0.57	0.02	-3.13	-0.24
	NAV *	-1.53	0.51	0.02	-2.82	-0.25
LLE [voxels], N = 32						
CAM	NAV	-0.02	0.14	1.00	-0.37	0.33
	NO *	-1.82	0.29	<0.01	-2.55	-1.09
NAV	CAM	0.02	0.14	1.00	-0.33	0.37
	NO *	-1.80	0.27	<0.01	-2.48	-1.12
NO	CAM *	1.82	0.29	<0.01	1.09	2.55
	NAV *	1.80	0.27	<0.01	1.12	2.48

a. Adjustment for multiple comparisons: Bonferroni.
*. The mean difference is significant at the .05 level.

5.3.5 Quantitative flow analysis

The quantitative flow analysis for the TV showed no significant difference between the three respiratory-gated reconstructions for forward flow volume (Wilks' $\lambda = 0.82$, $F(2,21) = 2.34$, $p = 0.12$, $\eta^2 = 0.18$). However, a significant difference was found for backward flow volume (Wilks' $\lambda = 0.70$, $F(2,21) = 4.60$, $p = 0.02$, $\eta^2 = 0.30$), regurgitation fraction (Wilks' $\lambda = 0.66$, $F(2,21) = 5.54$, $p = 0.01$, $\eta^2 = 0.35$), and velocity (Wilks' $\lambda = 0.95$, $F(2,687) = 17.30$, $p < 0.01$, $\eta^2 = 0.48$). Follow-up pairwise comparisons indicated a significant difference only for CAM-vs-NO in backward flow volume –1.44 ± 0.48 ml ($p = 0.02$), CAM-vs-NO in regurgitation fraction –0.016 ± 0.005 ($p = 0.02$) and CAM-vs-NO in velocity 0.45 ± 0.12 cm/s ($p < 0.01$). Thus, NO data sets had higher backward flow volume, larger regurgitation fraction, and lower velocity compared to

CAM data sets. The TV pairwise comparisons are listed in **Table 5.2** and illustrated in **Supplemental Figure 5.4**.

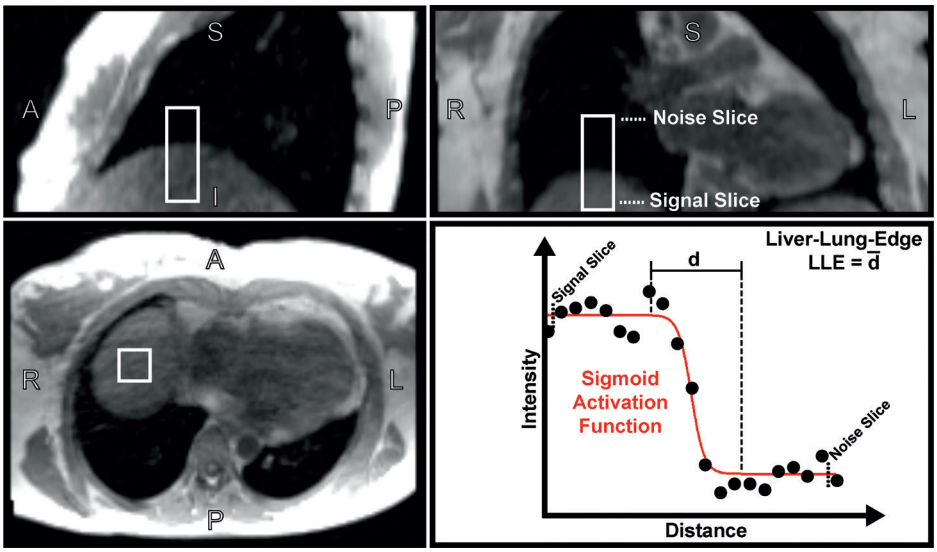

Figure 5.4: Quantitative image analysis illustration. The ROI (white box) of 10x10x30 voxels was manually defined per patient at the lung-liver border at the expected location of the navigator (see sagittal image, top left; and transversal image bottom left). In this ROI two slices were selected; one was entirely in the liver and the other entirely in the lung. The slice in the liver was defined as the signal area and the slice in the lung was defined as the noise area (see coronal image, top right). Between the liver and the lung slice in the ROI, 100 line profiles were extracted and fitted on a sigmoid function. Lung-liver edge (LLE) was defined by the mean width of the sigmoid activation functions.

For the PV, no significant difference was observed for backward flow volume (Wilks' $\lambda = 0.90$, $F(2,20) = 1.06$, $p = 0.36$, $\eta^2 = 0.01$) and regurgitation fraction (Wilks' $\lambda = 0.97$, $F(2,20) = 0.32$, $p = 0.73$, $\eta^2 = 0.03$). However, a significant difference was observed for forward flow volume (Wilks' $\lambda = 0.38$, $F(2,20) = 16.69$, $p < 0.01$, $\eta^2 = 0.63$) and velocity (Wilks' $\lambda = 0.97$, $F(2,657) = 11.07$, $p < 0.01$, $\eta^2 = 0.03$). Follow-up pairwise comparisons showed a significant difference in forward flow volume for NAV-vs-NO of –1.87 ± 0.32 ml/beat ($p < 0.01$) and CAM-vs-NO of –1.65 ± 0.57 ml/beat ($p = 0.03$), and velocity for CAM-vs-NO of –0.54 ± 0.17 cm/s ($p < 0.01$) and NAV-vs-NO of –0.58 ± 0.16 cm/s ($p < 0.01$). Thus, NO data sets had lower forward flow volume and lower velocity compared to CAM as well as NAV data sets. The PV pairwise comparisons are listed in **Table 5.3** and illustrated in **Supplemental Figure 5.5**.

For the MV, no significant difference was found in forward flow volume (Wilks' $\lambda = 0.89$, $F(2,21) = 1.32$, $p = 0.29$, $\eta^2 = 0.11$), backward flow volume (Wilks' $\lambda = 0.99$, $F(2,21) = 0.19$, $p = 0.83$, $\eta^2 = 0.02$), regurgitation fraction (Wilks' $\lambda = 0.99$, $F(2,21) = 0.15$, $p = 0.86$, $\eta^2 = 0.01$), and velocity (Wilks' $\lambda = 1.00$, $F(2,687) = 1.28$, $p = 0.28$, $\eta^2 = 0.04$). The MV pairwise comparisons are listed in **Supplemental Table 5.3** and illustrated in **Supplemental Figure 5.6**.

For the AV, no significant difference was observed in forward flow volume (Wilks' $\lambda = 0.93$, $F(2,21) = 0.74$, $p = 0.49$, $\eta^2 = 0.07$), backward flow volume (Wilks' $\lambda = 0.99$, $F(2,21) = 0.08$, $p = 0.92$, $\eta^2 = 0.01$), regurgitation fraction (Wilks' $\lambda = 0.92$, $F(2,21) = 0.97$, $p = 0.40$, $\eta^2 = 0.08$), and velocity (Wilks' $\lambda = 1.00$, $F(2,687) = 1.18$, $p = 0.31$, $\eta^2 = 0.03$). The AV pairwise comparisons are listed in **Supplemental Table 5.4** and illustrated in **Supplemental Figure 5.7**.

For the group with valvular regurgitation n_2, no significant difference was observed for backward flow volume (Wilks' $\lambda = 0.89$, $F(2,17) = 0.97$, $p = 0.40$, $\eta^2 = 0.10$) and regurgitation fraction (Wilks' $\lambda = 0.94$, $F(2,17) = 0.55$, $p = 0.59$, $\eta^2 = 0.61$). The n_2 pairwise comparisons are listed in **Supplemental Table 5.5** and illustrated in **Supplemental Figure 5.3**.

An example 4D flow analysis can be seen in **Figure 5.5** and **Supplemental Movie 5.1** showing the streamlines and regurgitation fraction for all three methods in a patient with mild PV and AV regurgitation.

Table 5.2: Pairwise comparisons of tricuspid valve (TV) quantitative flow analysis.

X	Y	Mean Diff. (X-Y)	Standard Error	Significance[a]	95% Confidence Interval for Diff.[a]	
					Lower Bound	Upper Bound
Forward flow volume (TV) [ml], N = 23						
CAM	NAV	-0.48	0.63	1.00	-2.11	1.15
	NO	0.93	0.52	0.26	-0.42	2.28
NAV	CAM	0.48	0.63	1.00	-1.15	2.11
	NO	1.41	0.70	0.17	-0.40	3.22
NO	CAM	-0.93	0.52	0.26	-2.28	0.42
	NAV	-1.41	0.70	0.17	-3.22	0.40
Backward flow volume (TV) [ml], N = 23						
CAM	NAV	-0.54	0.24	0.10	-1.15	0.07
	NO *	-1.44	0.48	0.02	-2.67	-0.20
NAV	CAM	0.54	0.24	0.10	-0.07	1.15
	NO	-0.90	0.39	0.09	-1.90	0.11
NO	CAM *	1.44	0.48	0.02	0.20	2.67
	NAV	0.90	0.39	0.09	-0.11	1.90
Regurgitation fraction (TV) [ ], N = 23						
CAM	NAV	-0.006	0.002	0.07	-0.013	0.000
	NO *	-0.016	0.005	0.02	-0.030	-0.002
NAV	CAM	0.006	0.002	0.07	0.000	0.013
	NO	-0.010	0.005	0.17	-0.023	0.003
NO	CAM *	0.016	0.005	0.02	0.002	0.030
	NAV	0.010	0.005	0.17	-0.003	0.023
Velocity (TV) [cm/s], N = 690						
CAM	NAV	0.23	0.10	0.09	-0.03	0.48
	NO *	0.45	0.12	0.00	0.16	0.74
NAV	CAM	-0.23	0.10	0.09	-0.48	0.03
	NO	0.22	0.12	0.21	-0.07	0.51
NO	CAM *	-0.45	0.12	<0.01	-0.74	-0.16
	NAV	-0.22	0.12	0.21	-0.51	0.07

a. Adjustment for multiple comparisons: Bonferroni.

*. The mean difference is significant at the .05 level.

Table 5.3: Pairwise comparisons of pulmonary valve (PV) quantitative flow analysis.

X	Y	Mean Diff. (X-Y)	Standard Error	Significance[a]	95% Confidence Interval for Diff.[a]	
					Lower Bound	Upper Bound
Forward flow volume (PV) [ml], N = 22						
CAM	NAV	0.21	0.55	1.00	-1.22	1.64
	NO *	-1.65	0.57	0.03	-3.14	-0.16
NAV	CAM	-0.21	0.55	1.00	-1.64	1.22
	NO *	-1.87	0.32	<0.01	-2.69	-1.04
NO	CAM *	1.65	0.57	0.03	0.16	3.14
	NAV *	1.87	0.32	<0.01	1.04	2.69
Backward flow volume (PV) [ml], N = 22						
CAM	NAV	-0.10	0.08	0.64	-0.29	0.10
	NO	-0.09	0.09	0.96	-0.32	0.14
NAV	CAM	0.10	0.08	0.64	-0.10	0.29
	NO	0.01	0.10	1.00	-0.26	0.28
NO	CAM	0.09	0.09	0.96	-0.14	0.32
	NAV	-0.01	0.10	1.00	-0.28	0.26
Regurgitation fraction (PV) [ ], N = 22						
CAM	NAV	-0.001	0.001	1.00	-0.004	0.002
	NO	0.000	0.001	1.00	-0.003	0.004
NAV	CAM	0.001	0.001	1.00	-0.002	0.004
	NO	0.001	0.002	1.00	-0.003	0.006
NO	CAM	0.000	0.001	1.00	-0.004	0.003
	NAV	-0.001	0.002	1.00	-0.006	0.003
Velocity (PV) [cm/s], N = 660						
CAM	NAV	0.04	0.14	1.00	-0.29	0.37
	NO *	-0.54	0.16	<0.01	-0.94	-0.15
NAV	CAM	-0.04	0.14	1.00	-0.37	0.29
	NO *	-0.58	0.16	<0.01	-0.97	-0.19
NO	CAM *	0.54	0.16	<0.01	0.15	0.94
	NAV *	0.58	0.16	<0.01	0.19	0.97

a. Adjustment for multiple comparisons: Bonferroni.
*. The mean difference is significant at the .05 level.

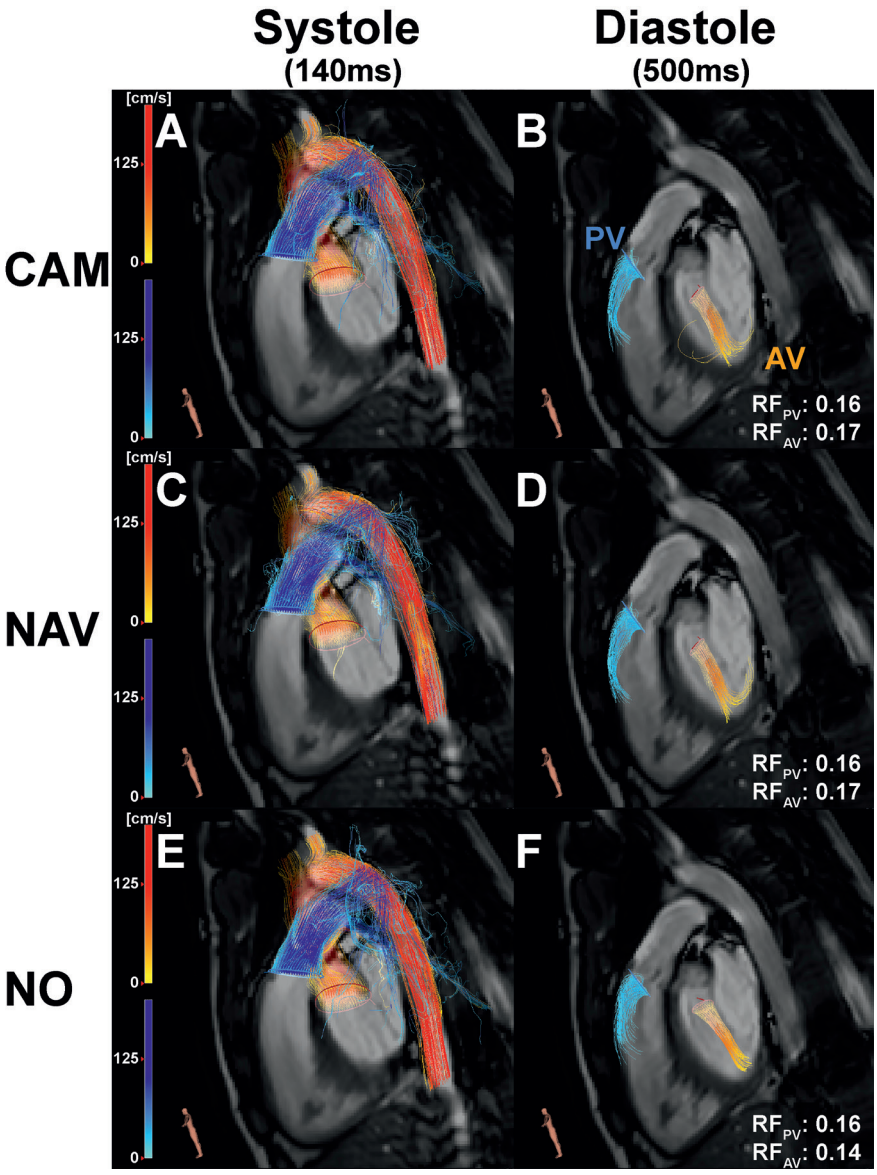

Figure 5.5: Whole-heart 4D flow analysis in CAAS. Shown are streamlines of CAM, NAV, and NO data sets for both systole **(A, C, E)** and diastole **(B, D, F)**. Regurgitation through the pulmonary valve (PV) and aortic valve (AV) can be seen during diastole. The corresponding regurgitation fractions (RF) are reported in **B, D, F**.

5.4 Discussion

This study compared whole-heart 4D flow MRI in patients with a spectrum of cardiovascular diseases using retrospective camera-based gating, navigator-based gating, and no gating. We observed that CAM and NAV data sets had similar image quality and flow measurement results. Compared to NO, both CAM and NAV showed improvements in quantitative image quality scores. However, no difference in qualitative image quality scoring was found between NAV, CAM, and NO. In a quantitative flow analysis, significant differences were measured in blood flow across two out of four valves for CAM-vs-NO and NAV-vs-NO.

The respiratory signals from CAM and NAV could not be directly compared by their amplitudes because of relative (CAM) vs. absolute (NAV) measurement of liver displacement. Those differences were noticeable in the different signal ranges or outlier peaks. Also, the signal amplitude range for CAM had a lower variation between patients compared to NAV, which did not allow for amplitude binning after prior rescaling of the signal. Therefore, although amplitude binning is superior to phase binning in terms of motion correction (for NAV) (29), only phase binning could be used in this study to enable a fair comparison with camera-based gating. In applications that require the information of absolute displacement in millimeters, as for instance in radiotherapy, the amplitude-binned NAV is superior to CAM with a motion signal in arbitrary units. However, in applications in which relative displacement is an option, such as 4D flow MRI, the derived respiratory phase is sufficient to compensate for respiratory motion, especially if the underlying signal amplitude is arbitrary, like for the respiratory belt, self-navigation, or camera signal.

Both methods performed equally well after phase binning, considering their strong correlation. The applied phase binning is robust for signal outliers and respiratory drifts (change of signal amplitude over time), which is highlighted in **Figure 5.2**. Furthermore, the reported phase delay was zero, which indicates no phase shift or different respiratory motion estimates between the two methods. Moreover, the reported phase delay standard deviation is acceptable. Even for the highest respiratory rates of 40 breaths per minute (breathing cycle duration of 1500 ms), which are typically only seen in newborns and elderlies (30,31), a difference of 63 ms would result in a mismatch of 4.2% and even decrease for lower respiratory rates (2.1% for 20 breaths per minute).

The qualitative image quality assessment did not reveal significant differences between the gating methods in any of the categories. However, the extremely low inter-rater reliability showed that the analysis itself had no significance and does not allow for a solid conclusion. Similarly, this result may indicate that the quality definitions were insufficient or that the raters were given poor instructions.

4D flow images are generally not high in contrast or rich in anatomical detail (1), which makes it challenging to identify subtle differences in a 4-point Likert-scale analysis. The quantitative image quality analysis with an objective measuring method showed that NAV and CAM data sets were superior to NO data sets in terms of SNR and LLE. Especially the decreased LLE (reduced blurring) for gated reconstruction underlined the benefit of respiratory gating.

The quantitative flow analysis supported the respiratory phase and image quality findings of a good overall agreement between CAM and NAV. Significant local differences were observed for NO in the valves of the right heart (TV and PV) showing that non-gated reconstructions likely lead to impaired flow measurements. However, this cannot be generalized as significant differences were only observed in TV backward flow volume, TV regurgitation fraction, PV forward flow volume as well as TV and PV mean velocity; and no significant differences were observed for the valves of the left heart (MV and AV). Moreover, the analysis of the valvular regurgitation subgroup n_2, showing no significant differences for backward flow volume and regurgitation fraction, indicates that diagnosis and risk assessment based on CAM, NAV, and NO image reconstructions will not differ. Altogether, no respiratory gating demonstrated noticeable flow measurement differences in valves of the right heart compared to CAM and NAV. No differences in flow measurement results were found between CAM and NAV. Three major questions might be raised when interpreting the results.

First, is respiratory gating needed, or is the expected motion perturbation without gating acceptable? In this study, a 60% expiration phase acceptance together with a spatial resolution of 2.5 mm isotropic was used and regional differences in transvalvular blood flow were observed for respiratory-gated data sets (CAM and NAV) compared to NO data sets. Although CAM and NAV data sets had fewer data points for image reconstruction, the respiratory gating resulted in superiority compared to NO data sets. Other studies (14,15) have shown that 100% respiratory

phase acceptance together with a 3.0 mm isotropic resolution, which is the largest voxel size recommended for whole heart 4D flow MRI (1), resulted in acceptable flow errors and preserved quantitative flow results. Dyverfeldt and Ebbers have shown that spatial resolutions finer than the degree of accepted respiratory motion do not result in improved data quality (7). Hence, the impact of respiratory motion depends on the anatomy under investigation and the used voxel size. In the current study, respiratory gating resulted in reduced LLE (less blurring) of about 2 voxels or 5 mm, which might be at the edge of a noticeable impact of respiratory gating as some categories showed an effect and others did not. When interested in accurate flow measurements for smaller voxel sizes (<2.5 mm), the impact of respiratory motion will likely be stronger.

Second, is the effect of respiratory gating of clinical relevance? Significant differences were observed for the TV and PV in the quantitative flow analysis, but those differences might still be clinically acceptable. For instance, the mean difference of TV backward flow volume measured with CAM compared to NO was around 1.4 ml/beat. In relation to the CAM mean backward flow volume of around 15.8 ml/beat, this is an 8.9% difference. Cases of larger net differences were also found; however, the relative differences are on a similar scale. Inaccuracies of 5–10% can in theory have an effect on severity assessment of for instance valve regurgitation, if the regurgitant volume is below a quantitative threshold with gating and above without, or vice versa. However, in practice, 4D flow MRI-based regurgitant flow measurement is just one of many indicators. Besides parameters derived from 4D flow MRI (e.g., regurgitant volume or fraction, peak velocity, flow eccentricity), 2D flow and multi-chamber cine images are also taken into consideration. Complete severity assessment with quantitative, qualitative, and semi-quantitative indicators might tolerate a 5–10% inaccuracy in determining the regurgitant flow volume. Nevertheless, any improvement of the regurgitant flow measurement should be considered if no trade-offs are required, which was the case in this study (i.e., the scan time stayed the same).

Third, if respiratory gating is preferred, which respiratory gating method should be chosen? Both methods do not require any patient interaction and, therefore, provide equal patient comfort. One clear advantage of the navigator is the respiratory motion measurement in absolute millimeters of displacement unlike the signal of the camera in arbitrary units. However, the navigator acquisition can disturb the image acquisition in the form of steady-state disruption or image sampling gaps that occur due to the navigator sampling. Therefore, CAM might be particularly useful in balanced steady-

state free precession imaging. Another important advantage of the camera is the higher sampling rate of 20 Hz compared to the 1–2 Hz of the navigator, which ensures sufficiently high sampling rates even for newborns or patients with shortness of breath (30,31). Yet another aspect might be the user-friendliness, in which the camera has an advantage as the contactless design facilitates a steady signal performance without any scan operator interaction like planning the navigator on the lung-liver border. Potential error sources for the camera in a clinical setup could be that the camera starts tracking another repetitive motion in the visual field like arm movement or a blanket flapping because of the air conditioning in the bore. Moreover, the visual field could be blocked or hindered by a head coil or other device. However, this is speculative, and the current study did not reveal performance differences between the camera and the lung-liver navigator. In addition, the usage of camera-based respiratory gating can be applied to other (imaging) modalities as well, e.g., home care vital sign monitoring (19).

Several studies have been published on contact-free physiological monitoring (32–37), but those did not involve cardiac 4D flow MRI. Harder et al. compared the same camera type and setup (abdominal imaging) to existing respiratory gating methods and reported that camera-based respiratory triggering (prospective gating) significantly improved image quality of 3D cholangiopancreatography images compared to conventional respiratory belt triggering (21).

5.4.1 Limitations

Firstly, due to the retrospective nature of this study, it did not include other respiratory gating techniques or flow measurement references as additional comparisons. Simultaneous signal acquisition by a respiratory belt or by self-navigation would have provided additional information on optimal respiratory gating. Unfortunately, both methods were not possible in this study as the k-space sampling was not optimized for self-navigation and no respiratory belt was used.

Furthermore, the origin of the different signal ranges and extrema remains unclear. Possible explanations could be body movement or abnormal breathing such as gasping or agonal respiration, and how the vendor-implemented algorithms deal with abnormal breathing. As those algorithms were not available, and no video recordings were made of patient breathing and movement, this matter should be investigated in future research.

5.4.2 Conclusion

Camera-based respiratory monitoring performs as well as conventional lung-liver navigator-based respiratory monitoring in retrospectively gated whole-heart 4D flow MRI. Respiratory phases of the two techniques were highly correlated. Quantitative image quality analysis revealed superiority of respiratory gating compared to no gating, and no differences between the two gating techniques. Quantitative flow analysis revealed local flow differences in the tricuspid and pulmonary valves in images reconstructed without respiratory gating compared to those with respiratory gating, but no differences were found between images reconstructed with camera-based and navigator-based respiratory gating.

5.5 Supplemental material

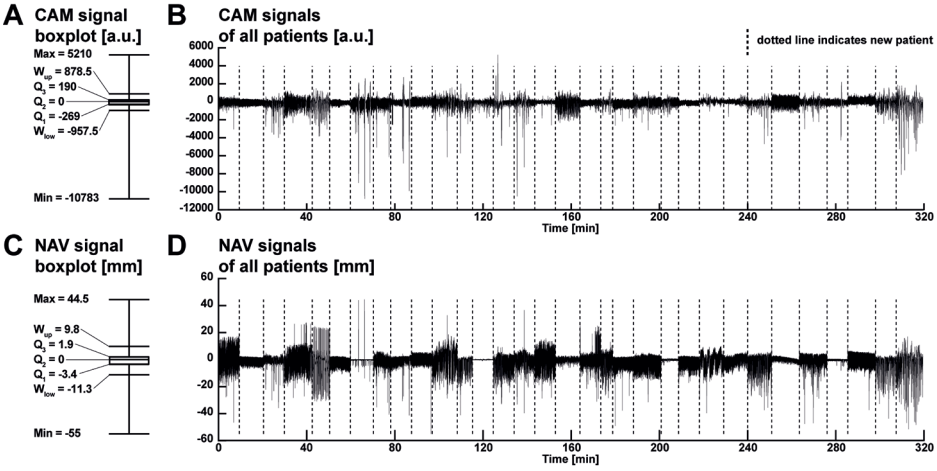

Supplemental Figure 5.1: Visualization of the CAM (A) and NAV (B) signal amplitudes of all patients. The signals, after zero mean shifting, were put behind each other in time. A vertical dotted line indicates a new patient.

Supplemental Figures 5.2 to **5.7**, **Supplemental Tables 5.1** to **5.5** and **Supplemental Movie 5.1** can be found online: https://onlinelibrary.wiley.com/doi/10.1002/jmri.27564, under Supporting Information.

5.6 Appendix

Phase binning algorithm:

1. Read in the raw signal.
2. Rescale the signal to zero median.
3. Smooth signal over 1s.
4. Define the minimal distance between same sign peaks to 45 breath per minute (highest expected breathing frequency).
5. Calculate extrema (minima/maxima) with minimal distance: islocalmax(signal, minimal distance) MATLAB function.
6. Calculate minimal peak prominence as 1/4 of the median maxima–minima distance.
7. Calculate extrema (minima/maxima) with minimal distance and minimal peak prominence: islocalmax(signal, minimal distance, minimal peak prominence) MATLAB function.
8. Correct for double extrema in case one minimum is followed by two maximums and vice versa.
9. Phase bin the respiratory signal in 100 bins.
10. Reject inspiration data (1 to 40) and accept expiration data (41 to 100).
11. Label the data according to the signal.

5.7 References

1. Dyverfeldt P, Bissell M, Barker AJ, et al. 4D flow cardiovascular magnetic resonance consensus statement. J Cardiovasc Magn Reson. 2015;17(1):1–19.
2. Zhong L, Schrauben EM, Garcia J, et al. Intracardiac 4D Flow MRI in Congenital Heart Disease: Recommendations on Behalf of the ISMRM Flow & Motion Study Group. J Magn Reson Imaging. 2019;50(3):677–681.
3. Vasanawala SS, Hanneman K, Alley MT, Hsiao A. Congenital heart disease assessment with 4D flow MRI. J Magn Reson Imaging. 2015;42(4):870–886.
4. Crandon S, Elbaz MSM, Westenberg JJM, van der Geest RJ, Plein S, Garg P. Clinical applications of intra-cardiac four-dimensional flow cardiovascular magnetic resonance: A systematic review. Int J Cardiol. 2017;249:486–493.
5. Garcia J, Markl M, Schnell S, et al. Evaluation of aortic stenosis severity using 4D flow jet shear layer detection for the measurement of valve effective orifice area. Magn Reson Imaging. 2014;32(7):891–898.
6. Hsiao A, Lustig M, Alley MT, Murphy MJ, Vasanawala SS. Evaluation of valvular insufficiency and shunts with parallel-imaging compressed-sensing 4D phase-contrast MR imaging with stereoscopic 3D velocity-fusion volume-rendered visualization. Radiology. 2012;265(1):87–95.
7. Dyverfeldt P, Ebbers T. Comparison of respiratory motion suppression techniques for 4D flow MRI. Magn Reson Med. 2017;78(5):1877–1882.
8. McClelland JR, Hawkes DJ, Schaeffter T, King AP. Respiratory motion models: A review. Med Image Anal. 2013;17(1):19–42.
9. Uribe S, Muthurangu V, Boubertakh R, et al. Whole-heart cine MRI using real-time respiratory self-gating. Magn Reson Med. 2007;57(3):606–613.
10. Walheim J, Dillinger H, Kozerke S. Multipoint 5D flow cardiovascular magnetic resonance - accelerated cardiac- and respiratory-motion resolved mapping of mean and turbulent velocities. J Cardiovasc Magn Reson. 2019;21(1):42.
11. Kolbitsch C, Bastkowski R, Schäffter T, et al. Respiratory motion corrected 4D flow using golden radial phase encoding. Magn Reson Med. 2020;83(2):635–644.
12. Bastkowski R, Weiss K, Maintz D, Giese D. Self-gated golden-angle spiral 4D flow MRI. Magn Reson Med. 2018;80(3):904–913.
13. Crandon S, Westenberg JJM, Swoboda PP, et al. Impact of Age and Diastolic Function on Novel, 4D flow CMR Biomarkers of Left Ventricular Blood Flow Kinetic Energy. Sci Rep. 2018;8(1):14436.
14. Garg P, Westenberg JJM, van den Boogaard PJ, et al. Comparison of fast acquisition strategies in whole-heart four-dimensional flow cardiac MR: Two-center, 1.5 Tesla, phantom and in vivo validation study. J Magn Reson Imaging. 2018;47(1):272–281.
15. Kanski M, Töger J, Steding-Ehrenborg K, et al. Whole-heart four-dimensional flow can be acquired with preserved quality without respiratory gating, facilitating clinical use: a head-to-head comparison. BMC Med Imaging. 2015;15(1):1–13.
16. Cerviño LI, Du J, Jiang SB. MRI-guided tumor tracking in lung cancer radiotherapy. Phys Med Biol. 2011;56(13):3773–3785.
17. Cheng JY, Zhang T, Alley MT, et al. Comprehensive Multi-Dimensional MRI for the Simultaneous Assessment of Cardiopulmonary Anatomy and Physiology. Sci Rep. 2017;7(1):5330.
18. Peper ES, Gottwald LM, Zhang Q, et al. Highly accelerated 4D flow cardiovascular magnetic resonance using a pseudo-spiral Cartesian acquisition and compressed sensing reconstruction for carotid flow and wall shear stress. J Cardiovasc Magn Reson. 2020;22(1):7.
19. Rocque M. Fully automated contactless respiration monitoring using a camera. IEEE Int Conf Consum Electron. 2016. p. 478–479.

20. Kruger MG, Springer RPW, Kersten GM, Bril RJ. Contactless Vital Sign Monitoring using a COTS Resource-Constrained Multi-Core System. IECON 2019 - 45th Annu Conf IEEE Ind Electron Soc. p. 3057–3062.
21. Harder F, Lohöfer FK, Kaissis GA, et al. Camera-based respiratory triggering improves the image quality of 3D magnetic resonance cholangiopancreatography. Eur J Radiol. 2019;120:108675.
22. Gottwald LM, Peper ES, Zhang Q, et al. Pseudo-spiral sampling and compressed sensing reconstruction provides flexibility of temporal resolution in accelerated aortic 4D flow MRI: A comparison with k-t principal component analysis. NMR Biomed. 2020;33(4):e4255.
23. Uecker M, Ong F, Tamir JI, et al. Berkeley Advanced Reconstruction Toolbox. Proc Intl Soc Mag Reson Med. 2015;23(1):2486.
24. van Ooij P, Semaan E, Schnell S, et al. Improved respiratory navigator gating for thoracic 4D flow MRI. Magn Reson Imaging. 2015;33(8):992–999.
25. Loecher M, Schrauben E, Johnson KM, Wieben O. Phase unwrapping in 4D MR flow with a 4D single-step laplacian algorithm. J Magn Reson Imaging. 2016;43(4):833–842.
26. Kamphuis VP, Roest AAW, Ajmone Marsan N, et al. Automated Cardiac Valve Tracking for Flow Quantification with Four-dimensional Flow MRI. Radiology. 2019;290(1):70–78.
27. Blanken CPS, Westenberg JJM, Aben J-P, et al. Quantification of Mitral Valve Regurgitation from 4D Flow MRI Using Semiautomated Flow Tracking. Radiol Cardiothorac Imaging. 2020;2(5):e200004.
28. Hayes AF, Krippendorff K. Answering the Call for a Standard Reliability Measure for Coding Data. Commun Methods Meas. 2007;1(1):77–89.
29. van Kesteren Z, van der Horst A, Gurney-Champion OJ, et al. A novel amplitude binning strategy to handle irregular breathing during 4D MRI acquisition: improved imaging for radiotherapy purposes. Radiat Oncol. 2019;14(1):80.
30. Hermansen CL, Mahajan A. Newborn Respiratory Distress. Am Fam Physician. 2015;92(11):994–1002.
31. Rodríguez-Molinero A, Narvaiza L, Ruiz J, Gálvez-Barrón C. Normal Respiratory Rate and Peripheral Blood Oxygen Saturation in the Elderly Population. J Am Geriatr Soc. 2013;61(12):2238–2240.
32. Lange T, Maclaren J, Herbst M, Lovell-Smith C, Izadpanah K, Zaitsev M. Knee cartilage MRI with in situ mechanical loading using prospective motion correction. Magn Reson Med. 2014;71(2):516–523.
33. Todd N, Josephs O, Callaghan MF, Lutti A, Weiskopf N. Prospective motion correction of 3D echo-planar imaging data for functional MRI using optical tracking. Neuroimage. 2015;113:1–12.
34. Maziero D, Velasco TR, Hunt N, et al. Towards motion insensitive EEG-fMRI: Correcting motion-induced voltages and gradient artefact instability in EEG using an fMRI prospective motion correction (PMC) system. Neuroimage. 2016;138:13–27.
35. Frost R, Wighton P, Karahanoğlu FI, et al. Markerless high-frequency prospective motion correction for neuroanatomical MRI. Magn Reson Med. 2019;82(1):126–144.
36. Chikop SA, Anchan ABS, Koulagi G, Honnedevasthana AA, Imam S, Geethanath S. Automatic motion correction of musculoskeletal MRI using DSLR camera. Magn Reson Imaging. 2018;48:74–79.
37. DiGiacomo P, Maclaren J, Aksoy M, et al. A within-coil optical prospective motion-correction system for brain imaging at 7T. Magn Reson Med. 2020;84(3):1661–1671.

Coronary Flow Assessment using Accelerated 4D Flow MRI with Respiratory Motion Correction

6

Carmen P.S. Blanken
Eric M. Schrauben
Eva S. Peper
Lukas M. Gottwald
Bram F. Coolen
Diederik F. van Wijk
Jan J. Piek
Gustav J. Strijkers
R. Nils Planken
Pim van Ooij
Aart J. Nederveen

Front. Bioeng. Biotechnol. 2021; 9: 729.

Abstract

Magnetic resonance imaging (MRI) can potentially be used for non-invasive screening of patients with stable angina pectoris to identify probable obstructive coronary artery disease. MRI-based coronary blood flow quantification has to date only been performed in a 2D fashion, limiting its clinical applicability. In this study, we propose a framework for coronary blood flow quantification using accelerated 4D flow MRI with respiratory motion correction and compressed sensing image reconstruction. We investigate its feasibility and reproducibility in healthy subjects at rest. Fourteen healthy subjects received 8 times-accelerated 4D flow MRI covering the left coronary artery (LCA) with an isotropic spatial resolution of 1.0 mm^3. Respiratory motion correction was performed based on 1) lung-liver navigator signal, 2) real-time monitoring of foot-head motion of the liver and LCA by a separate acquisition, and 3) rigid image registration to correct for anterior-posterior motion. Time-averaged diastolic LCA flow was determined, as well as time-averaged diastolic maximal velocity (V_{MAX}) and diastolic peak velocity (V_{PEAK}). 2D flow MRI scans of the LCA were acquired for reference. Scan-rescan reproducibility and agreement between 4D flow MRI and 2D flow MRI were assessed in terms of concordance correlation coefficient (CCC) and coefficient of variation (CV). The protocol resulted in good visibility of the LCA in 11 out of 14 subjects (6 female, 5 male, aged 28 ± 4 years). The other 3 subjects were excluded from analysis. Time-averaged diastolic LCA flow measured by 4D flow MRI was 1.30 ± 0.39 ml/s and demonstrated good scan-rescan reproducibility (CCC/CV = 0.79/20.4%). Time-averaged diastolic V_{MAX} (17.2 ± 3.0 cm/s) and diastolic V_{PEAK} (24.4 ± 6.5 cm/s) demonstrated moderate reproducibility (CCC/CV = 0.52/19.0% and 0.68/23.0%, respectively). 4D flow- and 2D flow-based diastolic LCA flow agreed well (CCC/CV = 0.75/20.1%). Agreement between 4D flow MRI and 2D flow MRI was moderate for both diastolic V_{MAX} and V_{PEAK} (CCC/CV = 0.68/20.3% and 0.53/27.0%, respectively). In conclusion, the proposed framework of accelerated 4D flow MRI equipped with respiratory motion correction and compressed sensing image reconstruction enables repeatable diastolic LCA flow quantification that agrees well with 2D flow MRI.

6.1 Introduction

The clinical evaluation of obstructive coronary artery disease (CAD) relies on a combined approach of catheter-based coronary artery angiography (CAG) and physiological testing with for example fractional flow reserve (FFR) or instantaneous wave-free ratio (iFR). Current guidelines recommend non-invasive testing in patients with stable angina pectoris (SAP) to identify probable obstructive CAD before performing invasive CAG (1,2).

MRI is a non-invasive, non-ionizing imaging technique that can reliably provide prognostic information in patients with CAD using stress-induced perfusion imaging (3). In fact, MRI provides detailed anatomical information (4–6) and can also measure coronary flow (7–11), potentially enabling assessment of the coronary flow reserve (CFR). The CFR is a measure for the adaptive capacity of the coronary vascular bed to meet the myocardial oxygen demand during increased oxygen consumption of the myocardium. Large-scale studies have shown that a CFR of less than 2.0 is an independent predictor of cardiac mortality and major adverse cardiac events and has greater prognostic value than FFR (12–14). The potential of MRI to concurrently assess coronary anatomy, CFR and myocardial perfusion makes it a potential screening modality for accurate selection and planning of patients with SAP for percutaneous coronary intervention (PCI).

To date, MRI-based coronary flow quantification has only been reported using 2D flow MRI (7–10), which has limitations for clinical use. It requires prior knowledge of the desired measurement location(s) and its accuracy depends highly on correct planning of the imaging slice, i.e. perpendicular to the vessel, distal to the stenosis of interest. In contrast, 4D flow MRI (time-resolved three-dimensional three-directional phase-contrast MRI) provides volumetric coverage (15). Therefore, the acquisition is easy to plan, analysis planes can be placed after image acquisition and the flow can be quantified at multiple locations from a single data set. Yet, coronary flow quantification using 4D flow MRI has never been reported, presumably because the small size of the coronary arteries necessitates the use of a high spatial resolution (~1 mm^3), leading to unrealistically long scan times that make it nearly impossible to avoid patient movement causing image deterioration.

High spatial resolution 4D flow MRI at clinically feasible scan times requires sparse sampling. Pseudo-spiral Cartesian undersampling with compressed sensing image reconstruction has previously made intracranial flow quantification possible with good accuracy and reproducibility (16). Application of this technique to the coronary arteries is promising, provided that we can correct for respiratory motion.

In the current study, we therefore investigate the feasibility and reproducibility of accelerated, high spatial resolution 4D flow MRI with respiratory motion correction for flow quantification in the left coronary artery (LCA) of healthy subjects at rest. We hypothesize that respiratory motion correction results in improved visibility of the LCA compared to non-corrected data, and that 4D flow MRI-based measurements of LCA flow agree well with 2D flow MRI-based measurements.

6.2 Materials and methods

6.2.1 Image acquisition

Fourteen healthy subjects (8 female, 6 male, aged 28 ± 4 years) underwent cardiac MRI at 3T (Ingenia Philips, Best, the Netherlands). The study was approved by the local institutional review board (METC) of Amsterdam UMC and all participants gave written informed consent. A Dixon cardiac angiogram with isotropic spatial resolution of 1.5 mm^3 was acquired for planning purposes using electrocardiographic (ECG) gating to mid-diastole and respiratory gating using a lung-liver navigator with an end-expiration acceptance window of 7 mm. Next, a 4D flow MRI acquisition was performed with an isotropic spatial resolution of 1.0 mm^3, covering the LCA in a 30-mm-thick transversal slab. This acquisition was directly followed by a 2D flow MRI acquisition planned perpendicular to the LCA, with a spatial resolution of 1.0x1.0 mm^2 and 6.0 mm slice thickness. For the purpose of reproducibility testing, the sequence of the aforementioned 4D and 2D acquisitions was performed once more with identical settings.

4D flow MRI was acquired using 8 times-accelerated pseudo-spiral undersampling (17,18). Three-directional velocity-encoding sensitivity (VENC) was set to 50 cm/s and retrospective ECG-gating enabled cardiac binning into 24 phases. A pencil beam navigator was played out on the lung-liver interface to monitor respiratory motion at a sampling frequency of 2 Hz. To reject outliers caused by deep inspiration, an acceptance window of 20 mm was employed. Breathheld 2D flow MRI was acquired

using parallel imaging with a SENSE factor of 2. Through-plane VENC was set to 35 cm/s (lower than for the 4D flow MRI, since the larger slice thickness causes spatial velocity averaging which in our experience conceals local peak velocities observed in the 4D flow MRI acquisition).

Lastly, a real-time coronal balanced steady state free precession (bSSFP) series was run for ~50 seconds to monitor foot-head respiratory motion of the LCA with respect to the motion of the liver. This scan was ECG-triggered to mid-diastole and had a spatial resolution of 2.0x2.0 mm^2 and slice thickness of 8.0 mm.

6.2.2 Respiratory motion correction and image reconstruction

Prior to reconstruction of the final images, respiration-induced motion of the LCA was corrected in both the foot-head (FH) and anterior-posterior (AP) directions. The methodology is schematically depicted in **Figure 6.1**.

6.2.2.1 Motion correction in foot-head direction

FH motion correction was based on the 4D flow respiratory navigator signal in combination with the real-time coronal scan. In short, the real-time scan was used to determine the ratio ρ between the motion of LCA and liver motion in FH direction, to be able to estimate LCA motion at every k-space readout and correct for it prior to image reconstruction. LCA and liver motion curves were determined by rigid image registration on two separate regions of interest, and their end-expiration heights were aligned. LCA and liver positions were plotted against each other and a linear fit was made, the slope of which is equal to ρ. Next, the lung-liver navigator positions were interpolated to give a position at the time of every imaging readout. The resulting navigator positions will be referred to as $\boldsymbol{NAV}(t)$. Offsets from end-expiration were determined and converted into LCA position offsets by multiplication with ρ. To correct for these offsets, readout-specific phase shifts were calculated by multiplying the normalized k-space coordinate in the FH direction $\boldsymbol{k}_z(t)$ with the corresponding LCA offset. The complex raw k-space data $K(t)$ was then multiplied with these phase shifts.

6.2.2.2 Motion correction in anterior-posterior direction

After sorting $\boldsymbol{NAV}(t)$ into 8 independent respiratory phase bins with equal amounts of data, bin-specific, time-averaged images were reconstructed from the FH motion-corrected raw 4D flow data, using only k-space samples that were acquired during mid-diastole. From each reconstruction, five central slices were averaged to remove

any remaining unresolved FH motion, and rigid image registration of bins 2–8 to bin 1 (end-expiration) was performed over a central region including the LCA. This produced AP offsets per bin, which were corrected in the complex raw k-space data in a similar manner as described for the FH offsets. Right-left offsets were expected to be small and were thus ignored.

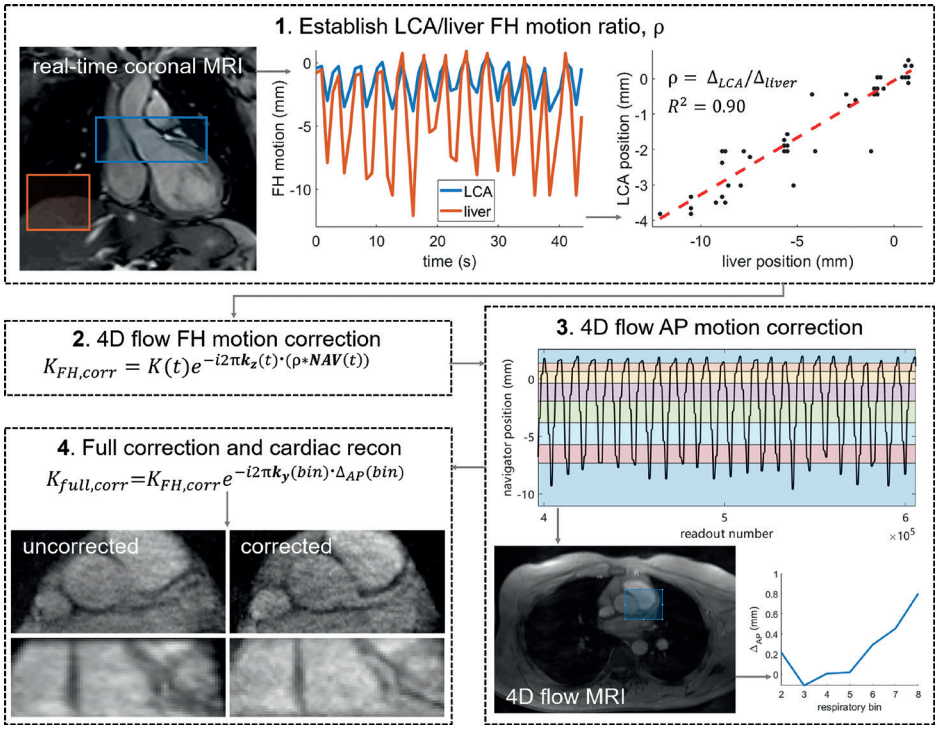

Figure 6.1: Post-processing pipeline used to correct for respiratory motion in the 4D flow MRI acquisitions. **1)** a real-time ECG-triggered scan was used to determine the ratio ρ between the motion of LCA and liver motion in foot-head (FH) direction. Motion curves were determined by rigid image registration on two separate regions of interest: over the LCA (blue) and over the liver (red). LCA and liver positions were plotted against each other and a linear fit was made, the slope of which is equal to ρ. **2)** LCA offsets, calculated by multiplying liver offsets ***NAV***(t) with ρ, were converted into time-dependent phase shifts by multiplying the normalized k-space coordinate in the FH direction $\boldsymbol{k}_z$(t) with the corresponding LCA offset. The complex raw k-space data *K*(t) was then multiplied with these phase shifts. **3)** ***NAV***(t) was binned into 8 respiratory phases with equal amounts of data and bin-specific images (time-averaged over mid-diastolic time frames) were reconstructed from the FH motion-corrected raw data. Rigid image registration of bins 2–8 to bin 1 (end-expiration) was performed over a central region including the LCA, producing AP offsets per bin. **4)** AP offsets were corrected in the complex raw k-space data and final image reconstruction was performed.

6.2.2.3 Image reconstruction

Compressed sensing image reconstruction was performed in MATLAB R2019b (The MathWorks, Inc., Natick, MA), making use of a sparsifying total variation transform in time with a regularization parameter = 0.001 and 20 iteration steps using MRecon (Gyrotools, Zürich, Switzerland) and the Berkeley Advanced Reconstruction Toolbox (BART) (19). To assess the effect of the respiratory motion correction on the images, non-corrected images were reconstructed as well.

6.2.3 Data analysis

Data analysis was performed in GTFlow V3.2.15 (Gyrotools, Zürich, Switzerland). 4D flow MRI magnitude images were used to localize the LCA branching off from the aorta in a mid-diastolic time frame and to make a longitudinal cross-section, see **Figure 6.2**. The longitudinal view was used to place 5 equidistant analysis planes perpendicular to the LCA, approximately 1.5 mm apart, to be able to check for consistency of the measurements over the length of the LCA. Next, the LCA was visually identified in each plane and measurement contours were drawn around the lumen. Additional reference contours were drawn in the adjacent pericardial fat to verify that the measurements would amount to zero flow here, see **Figure 6.2**.

Both the LCA and the reference contours were copied to all mid-diastolic time frames and onto the corresponding velocity images. Other time frames in which the LCA could not be identified because of blurring due to myocardial contraction and relaxation were discarded. Diastolic flow curves were calculated for each contour, as well as streamlines for visualization. Contour-averaged flow curves were calculated for each subject and averaged over all subjects. For comparison with velocities reported in echocardiographic and 2D flow MRI studies, maximal velocity (V_{MAX}) was determined for each contour and each time frame by selecting the voxel with the highest signal within the contour. Next, time-averaged diastolic V_{MAX} and diastolic peak velocity (V_{PEAK}) were determined for each subject.

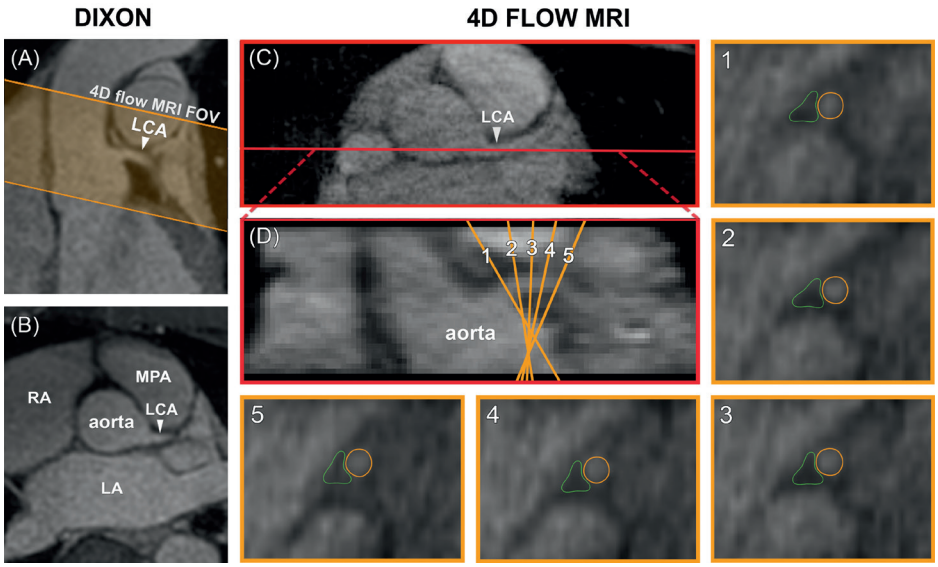

Figure 6.2: A) Planning of the 4D flow MRI field of view (orange) on the Dixon water image. **B)** Transversal view of the Dixon water image. **C)** The LCA is identified on a transversal 4D flow MRI magnitude image and a longitudinal cross-section is made (shown in red). **D)** The resulting coronal view is used to place five analysis planes perpendicular to the LCA. **1–5)** In these planes, measurement contours are placed around the LCA lumen and in adjacent pericardial fat. FOV = field of view, LCA = left coronary artery, LA = left atrium, RA = right atrium, MPA = main pulmonary artery.

Scan-rescan reproducibility of time-averaged diastolic flow, time-averaged diastolic V_{MAX} and diastolic V_{PEAK} was evaluated by means of Bland–Altman analysis, coefficient of variation (CV) and smallest detectable difference. Furthermore, concordance correlation coefficients (CCC) were determined based on absolute agreement and a two-way mixed-effects model (20). CCC was classified as: poor (<0.5), moderate (0.5–0.75), good (0.75–0.9) and excellent (>0.9) (21). CV was defined as the standard deviation of the scan-rescan differences divided by the mean of all scan and rescan measurements. The smallest detectable difference was defined as 1.96 times the standard deviation of the scan-rescan differences. A paired t-test was used to compare measured flows and velocities with 2D flow MRI and pericardial fat control measurements. Flow values will be presented as mean ± SD.

6.3 Results

6.3.1 4D flow MRI

Median scan time was 12:20 min per 4D flow MRI scan (IQR: 11:30–13:15 min) with a respiratory gating efficiency of approximately 90%. Three subjects were excluded because of insufficient visibility of the LCA in both the original and motion corrected reconstructions. In these subjects, a pattern of relatively long inspiration phases and no clear skewness towards end-expiration was observed. In the remaining eleven subjects (6 female, 5 male, aged 28 ± 4 years), the LCA was identified in the magnitude images and velocity signal in the phase images. An overview of all original and corrected reconstructions can be found in **Supplemental Figure 6.1**.

Figure 6.3 shows example images of phase-contrast magnitude and velocity in right-left direction. **Figure 6.4** shows streamlines in the LCA, splitting into left anterior descending (LAD) and left circumflex (LCX) coronary artery. A video of the streamlines can be found in **Supplemental Video 6.1**. Flow curves from this acquisition are presented in **Figure 6.5** (top). Seven out of 24 time frames were examined in this subject. In the other subjects, the number of examined cardiac frames ranged from 5 to 8.

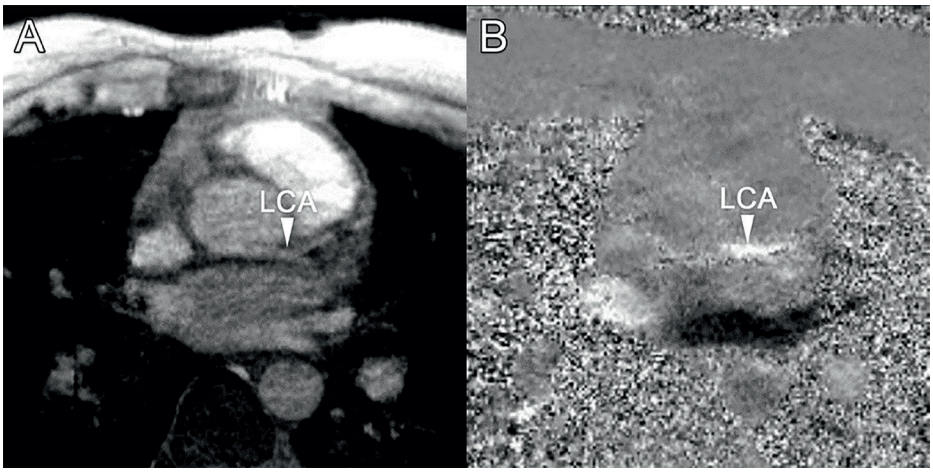

Figure 6.3: A) Transversal 4D flow MRI magnitude image and **B)** phase image showing velocities in right-left direction during mid-diastole. Arrows indicate the location of the left coronary artery, where velocity signal can be observed.

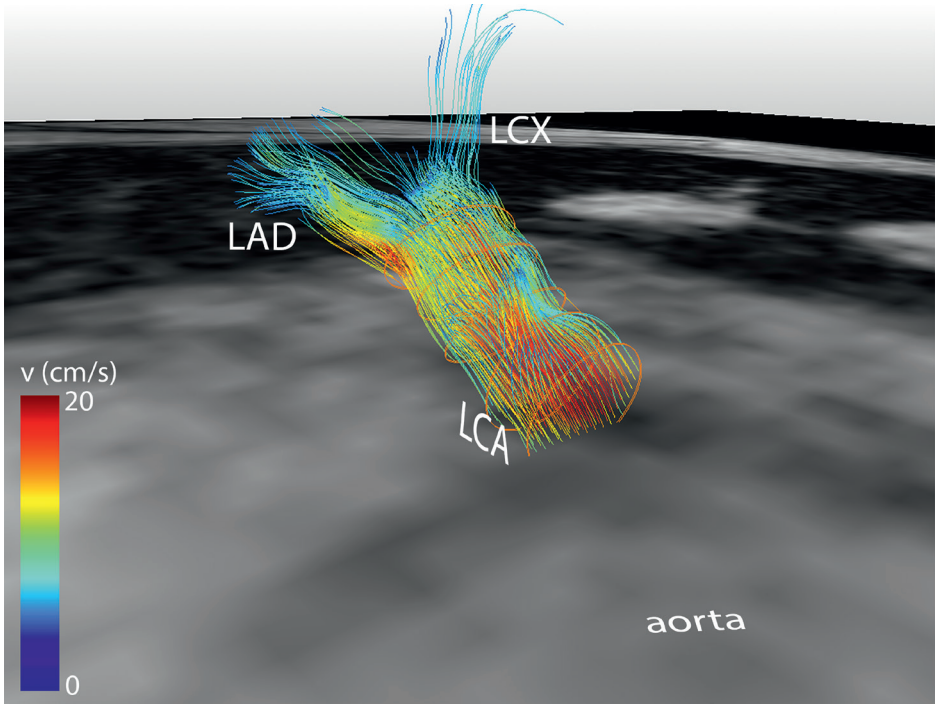

Figure 6.4: Streamline reconstruction of 4D flow MRI-derived velocities in the LCA for a mid-diastolic time frame. Streamlines initiate from five contours placed in the LCA and split into LAD and LCX. Velocity color-coding shows that the measured velocities in the LAD and LCX are lower than in the LCA.

Averaged over all subjects, time-averaged diastolic flows of 1.30 ± 0.39 ml/s in the LCA and 0.11 ± 0.14 ml/s in adjacent pericardial fat were measured, see **Figure 6.5** (bottom). Mean scan-rescan difference and limits of agreement were –0.05 [–0.57; 0.47] ml/s in the LCA – resulting in a smallest detectable difference of 0.52 ml/s – and –0.04 [–0.59; 0.51] ml/s in the pericardial fat (**Figure 6.6**). LCA and pericardial fat control measurements of diastolic flow differed significantly ($P < 0.001$). Averaged over all subjects, time-averaged diastolic V_{MAX} in the LCA was 17.2 ± 3.0 cm/s and diastolic V_{PEAK} was 24.4 ± 6.5 cm/s. Statistical results regarding reproducibility and agreement between 4D flow MRI and 2D flow MRI are summarized in **Table 6.1**. 4D flow-based diastolic LCA flow measurements had good scan-rescan reproducibility (CCC = 0.79, CV = 20.4%). Time-averaged diastolic V_{MAX} measurements were moderately repeatable (CCC = 0.52, CV = 19.0%), as were diastolic V_{PEAK} measurements (CCC = 0.68, CV = 23.0%).

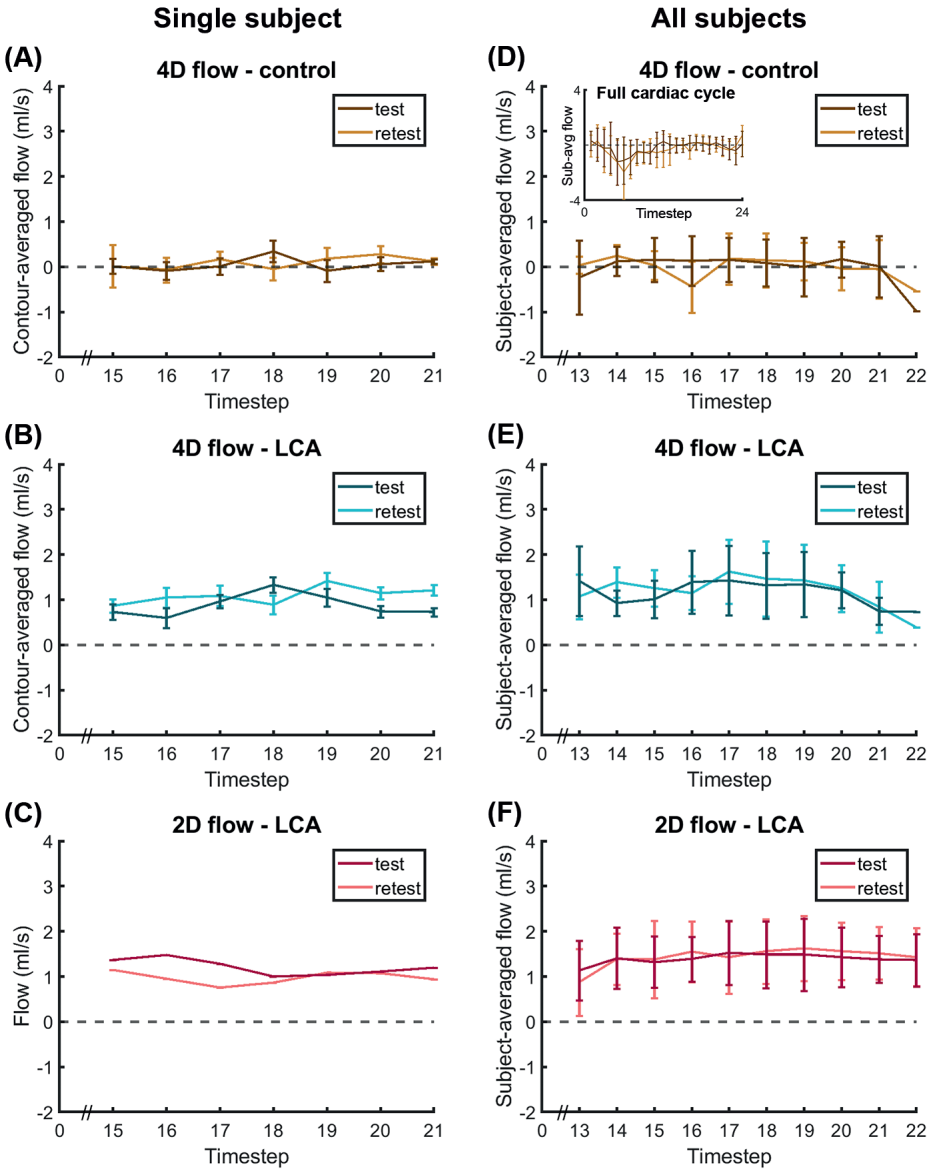

Figure 6.5: Diastolic flow measured by 4D flow MRI and 2D flow MRI in the LCA and by 4D flow MRI in the adjacent pericardial fat ("4D flow - control") in a single subject (**A–C**, same subject as in **Figure 6.4**) and averaged over all subjects **(D–F)**, displayed for scan and rescan 4D flow MRI acquisitions. Single-subject flow curves are the result of averaging over all five measurement contours. All-subjects flow curves are the average over all eleven subject-specific (contour-averaged) flow curves.

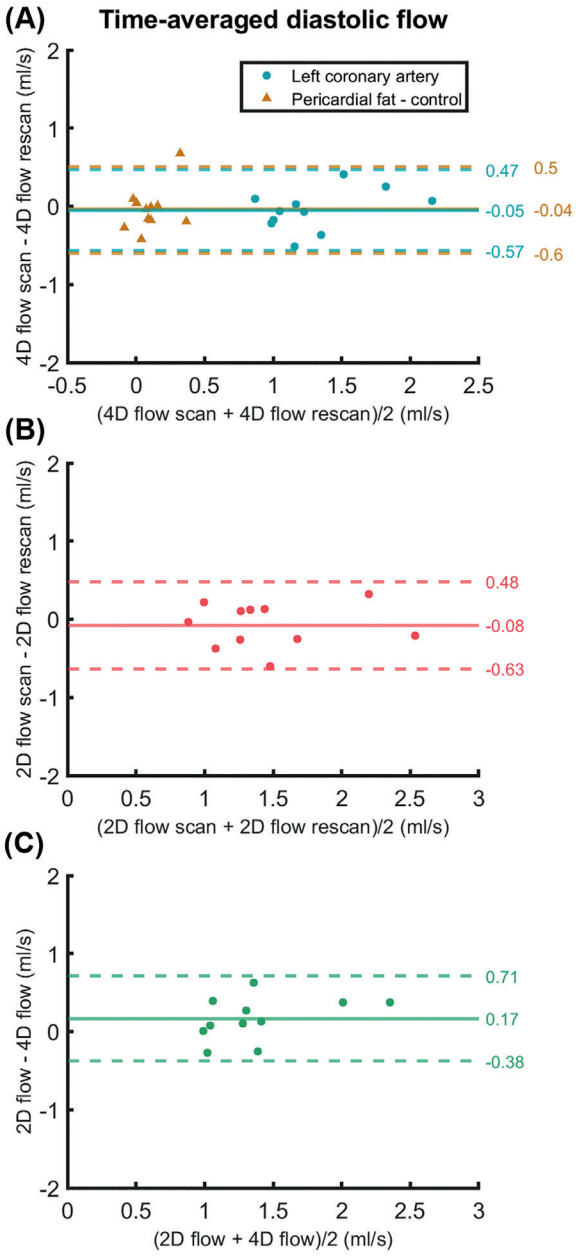

Figure 6.6: Bland–Altman plots of flow measurements of scan and rescan 4D flow MRI measurements **(A)**, scan and rescan 2D flow MRI measurements **(B)** and 4D flow MRI and 2D flow MRI scan-rescan-averaged measurements **(C)** of diastolic LCA flow. Data points are subject-specific. Mean differences and 95% limits of agreement are indicated on the right.

Table 6.1: Statistical results regarding scan-rescan reproducibility and agreement between 4D flow MRI and 2D flow MRI.

	4D flow - LCA		2D flow - LCA		LCA		4D flow - control	
Statistic	**Scan**	**Rescan**	**Scan**	**Rescan**	**4D flow**	**2D flow**	**Scan**	**Rescan**
Time-averaged diastolic flow (ml/s)								
Mean ± SD [ml/s]	1.27±0.46	1.32±0.36	1.43±0.53	1.51±0.52	1.30±0.39	1.47±0.50	0.09±0.23	0.12±0.15
Mean diff. [ml/s]	−0.05		−0.08		0.17		−0.04	
LOA [ml/s]	−0.57; 0.47		−0.63; 0.48		−0.38; 0.71		−0.59; 0.51	
CV [%]	20.4		19.4		20.1		n/a	
CCC	0.79		0.84		0.75		n/a	
SDD [ml/s]	0.52		0.56		n/a		n/a	
Time-averaged diastolic V_{MAX} (cm/s)								
Mean ± SD [cm/s]	17.6±4.0	16.8±2.6	17.3±5.4	18.3±5.9	17.2±3.0	17.8±5.6		
Mean diff. [cm/s]	0.83		−1.03		0.58			
LOA [cm/s]	−5.56; 7.22		−4.92; 2.86		−6.38; 7.54			
CV [%]	19.0		11.2		20.3			
CCC	0.52		0.92		0.68			
SDD [cm/s]	6.39		3.89		n/a			
Diastolic V_{PEAK} (cm/s)								
Mean ± SD [cm/s]	24.8±6.7	24.1±7.5	21.9±7.3	22.4±7.4	24.4±6.5	22.1±7.0		
Mean diff. [cm/s]	0.66		−0.50		−2.33			
LOA [cm/s]	−10.37; 11.69		−9.37; 8.38		−14.66; 10.0			
CV [%]	23.0		20.5		27.0			
CCC	0.68		0.81		0.53			
SDD [cm/s]	11.0		8.9		n/a			

LOA = limits of agreement, CV = coefficient of variation, CCC = concordance correlation coefficient, SDD = smallest detectable difference, control = pericardial fat reference measurements.

6.3.2 2D flow MRI

Time-averaged diastolic LCA flow as measured by 2D flow MRI was 1.47 ± 0.50 ml/s (**Figure 6.5**). Mean scan-rescan difference and limits of agreement were –0.08 [–0.63; 0.48] ml/s (**Figure 6.6**), resulting in a smallest detectable difference of 0.56 ml/s. Time-averaged diastolic V_{MAX} in the LCA was 17.8 ± 5.6 cm/s and diastolic V_{PEAK} was 22.1 ± 7.0 cm/s. 2D flow-based diastolic LCA flow measurements had good scan-rescan reproducibility (CCC = 0.84, CV = 19.4%), time-averaged diastolic V_{MAX} measurements were excellently repeatable (CCC = 0.92, CV = 11.2%) and diastolic V_{PEAK} measurements demonstrated good reproducibility (CCC = 0.81, CV = 20.5%) (**Table 6.1**).

4D flow- and 2D flow-based diastolic LCA flow agreed well (CCC = 0.75, CV = 20.1%) and did not significantly differ (p = 0.07), despite a trend towards higher measurements by 2D flow MRI as compared to 4D flow MRI (mean difference and limits of agreement: 0.17 [–0.38; 0.71] ml/s). Moderate agreement and no significant differences between 4D flow MRI and 2D flow MRI were found in measurements of time-averaged diastolic V_{MAX} (CCC = 0.68, CV = 20.3%, p = 0.60) and diastolic V_{PEAK} (CCC = 0.53, CV = 27.0%, p = 0.25).

6.4 Discussion

In this study, we investigated the feasibility and reproducibility of accelerated 4D flow MRI for blood flow quantification in the LCA of healthy subjects at rest. Prospective 8-fold undersampling, respiratory motion correction and compressed sensing image reconstruction facilitated 4D flow MRI-based LCA flow quantification during mid-diastolic time frames. Flow measurements were repeatable and agreed well with 2D flow MRI-based measurements.

CFR assessment is a possible application of the non-invasive LCA flow measurement performed in the current study. Based on the scan-rescan reproducibility found in this study, the difference of baseline flow and hyperemic flow should at least be 0.52 ml/s to be detected using the current MRI protocol. Given that the CFR is 4–5 (i.e. an increase from roughly 1.5 ml/s to 6.5 ml/s in the LCA) in healthy subjects and around 2 in patients (i.e. an increase from roughly 1.5 ml/s to 3.0 ml/s in the LCA), the actual difference will be well above the detection threshold of the presented method.

The observation that 4D flow MRI demonstrates lower reproducibility in maximal velocity measurement than 2D flow MRI may be explained by the inherently lower signal-to-noise ratio of the 4D flow MRI acquisition due to smaller voxel size along the length of the LCA (1 mm vs 6 mm for 2D flow MRI). Furthermore, unlike 2D flow MRI, 4D flow MRI does not benefit from the slice in-flow effect. The measured velocities were also less repeatable than has been reported for Doppler echocardiography (22–25).

Literature on healthy LCA diastolic peak velocities is limited. In the early 90's, studies appeared using transesophageal echocardiography for LCA flow quantification. These studies report baseline values – under general anesthesia – of 29 ± 12 cm/s, 34 ± 8 cm/s and 71 ± 19 cm/s in patients without left main coronary artery stenosis (25–27). More recent studies focus on the LAD using transthoracic echocardiography (22–24,28) or LAD, LCX and RCA using intracoronary Doppler (29–31) and no longer report LCA velocities. The 24.4 ± 6.5 cm/s (4D flow MRI) and 22.1 ± 7.0 cm/s (2D flow MRI) peak velocities we measured in the LCA are lower than previously reported in studies using transesophageal echocardiography (25–27), but similar to values measured using 2D flow MRI (32).

Studies using 2D flow MRI that measured LAD – as opposed to LCA – flow have reported time-averaged values of 0.5–1.4 ml/s (8–11). Other studies measured LAD peak flow velocities with 2D flow MRI to determine the CFR and found good correlations with CFR obtained by Doppler guide wire (in patients) and by PET (in healthy subjects) (33–37). Interestingly, measured peak velocities were significantly lower by 2D flow MRI than by Doppler guide wire, despite the good correlation between CFRs by the two techniques (35–38). These differences were probably a result of the different nature of the two measurements: Doppler guide wire measures velocities along a line whereas in phase-contrast MRI, velocity profiles are spatially smoothed when averaged over the volume of a voxel. Other MRI studies have focused on global CFR assessment based on velocity or flow measurement in the coronary sinus or based on myocardial perfusion by contrast-enhanced MRI (14,39–41). In short, a variety of studies has reported on coronary flows and velocities, but differences in modalities and anatomical locations of measurement complicate meaningful comparison between studies.

We quantified LCA flow at rest only. For CFR assessment, the flow should also be quantified in the hyperemic state, which may introduce more blurring due to a higher heart rate and heavier breathing, but may also result in higher SNR due to higher

velocities and a larger luminal area. Hyperemia can be induced in different ways, the most common being administration of a vasodilatory drug. Another possibility is physical exercise testing with the use of an MRI-compatible ergometer, but this introduces subject motion and has a smaller effect on the myocardial blood flow than a vasodilatory drug. Furthermore, inducing hypercapnia, an increased arterial CO2-pressure, with the use of a gas control breathing mask has been shown to have an effect similar to physical exercise (42).

Not only MRI, but also CT, PET-CT, and myocardial perfusion scintigraphy are potentially available non-invasive techniques to investigate different and sometimes overlapping characteristics of coronary artery disease (CAD) (43–45). PET-CT is a powerful technique because it can combine anatomical evaluation and corresponding functional status including coronary flow velocity (reserve) and the assessment of microvascular resistance. However, the limited availability, use of ionizing radiation and costs of PET-CT has prevented its widespread application in clinical practice. MRI may provide a more accessible alternative.

Recent developments in the field of cardiac MRI have enabled whole-heart 5D (4D + a respiratory motion dimension) flow imaging, 5D anatomical imaging of the heart including the coronary arteries, and high-resolution coronary angiography (5,46,47). The current study is the first to combine and implement high spatial resolution imaging, 3D time-resolved velocity encoding, and 2D respiratory motion correction to achieve coronary flow quantification. Vital to the successful combination of these assets are a number of design elements of the proposed framework. First, the use of pseudo-spiral Cartesian k-space sampling allows for a targeted FH field of view to enable 1.0 mm^3 resolution at a scan time of approximately 12 minutes. In contrast, Ma et al. (46) and Feng et al. (47) employ a radial phyllotaxis sampling scheme which requires a cubic field of view. This sampling strategy is relatively efficient for high-resolution respiratory motion-resolved whole-heart application (2.5 mm^3 at a scan time of 8 minutes, or 1.15 mm^3 at a scan time of 14 minutes with the aid of MR contrast), but would require impractically long scan times for 1.0 mm^3 resolution coronary application. For coronary angiography, Bustin et al. (5) employed a k-space sampling scheme similar to the current one, however their approach was optimized for diastolic vessel depiction instead of time-resolved flow measurement. Another important design element is the two-dimensional respiratory motion correction based on a one-dimensional navigator in combination with rigid image registration. Multi-dimensional motion correction or resolution is typically achieved

using self-navigation (5,46,47), which requires frequent sampling of the k-space center making it not readily compatible with non-radial sequences. A disadvantage of the 1D navigator-based approach we introduced is the necessary acquisition of an extra scan, prolonging the total scan time by approximately 1 minute. Furthermore, our motion correction pipeline is not fully automated and AP motion correction based on image registration requires interim image reconstruction. These aspects further prolong reconstruction time.

The current proof of concept study has a couple of limitations. First, we performed measurements in the LCA only. For meaningful clinical measurements, the approach should be extended to also encompass the LAD and LCX, as well as the right coronary artery (RCA). However, the spatial resolution employed in our study does not allow for accurate measurements in these smaller diameter (2.9–3.9 mm) vessels considering the fact that the luminal area should contain at least 16 voxels to keep the measurement error below 10% (48,49). An average LCA has a lumen diameter of 4.5 ± 0.5 mm and fits exactly 16 voxels of the size we used in this study (48). Hence, a higher spatial resolution has to be achieved for clinical application.

Secondly, we only considered diastolic time frames because of the presence of myocardial contraction- and relaxation-induced blurring of the LCA in the systolic images. To resolve this issue, a higher temporal resolution must be achieved while maintaining high spatial resolution. To date, this has only been achieved in single slice through-plane flow imaging with an efficient k-space sampling scheme (11). Nevertheless, for CFR assessment, diastolic flow values should suffice to determine the ratio between resting flow and hyperemic flow.

Lastly, we tested for reproducibility by performing two 4D flow MRI acquisitions in direct succession, without repositioning the subject. Consequently, differences in patient position or acquisition planning were not accounted for.

In general, the main difficulty with high-resolution 4D flow MRI applied to small diameter vessels is that it is prone to motion artifacts, due to the long acquisition time needed. The acquisitions may contain (involuntary) patient movement resulting in image blurring, and breathing motion may induce blurring or ghosting despite respiratory motion compensation, as opposed to single breathhold acquisition used in 2D flow MRI (50). A recent advancement, called focused navigation, enables non-rigid image

registration in 3D, and can in the future potentially be applied to flow imaging (6). Non-Cartesian k-space sampling, in combination with a high temporal resolution, might make the acquisition more robust against motion in general (51). This way, systolic time frames might be taken into account as well and flow curves over the entire cardiac cycle can be obtained.

6.5 Conclusion

The proposed framework of accelerated 4D flow MRI with respiratory motion correction and compressed sensing image reconstruction enables non-invasive, diastolic LCA flow quantification that agrees well with 2D flow MRI. Important assets of the developed methodology are the use of pseudo-spiral k-space sampling which allows for a targeted FH field of view, and the 2D respiratory motion correction based on a 1D navigator. Opportunities for further optimization exist in enhancing the temporal resolution, automating the entire reconstruction pipeline, and improving robustness for atypical breathing patterns using more advanced k-space sampling and motion correction schemes. The observed scan-rescan reproducibility justifies future experiments on quantification of hyperemic LCA flow, to investigate whether the current acquisition can be used to determine CFR.

6.6 Acknowledgements

We thank Pit Spee, BSc, for his assistance in setting up the scan protocol and data analysis protocol.

6.7 Material availability statement

All 4D flow data were acquired using our in-house developed AMC “PROspective Undersampling in multiple Dimensions” (PROUD) patch. A compiled version of this patch is available on reasonable request.

6.8 Supplemental material

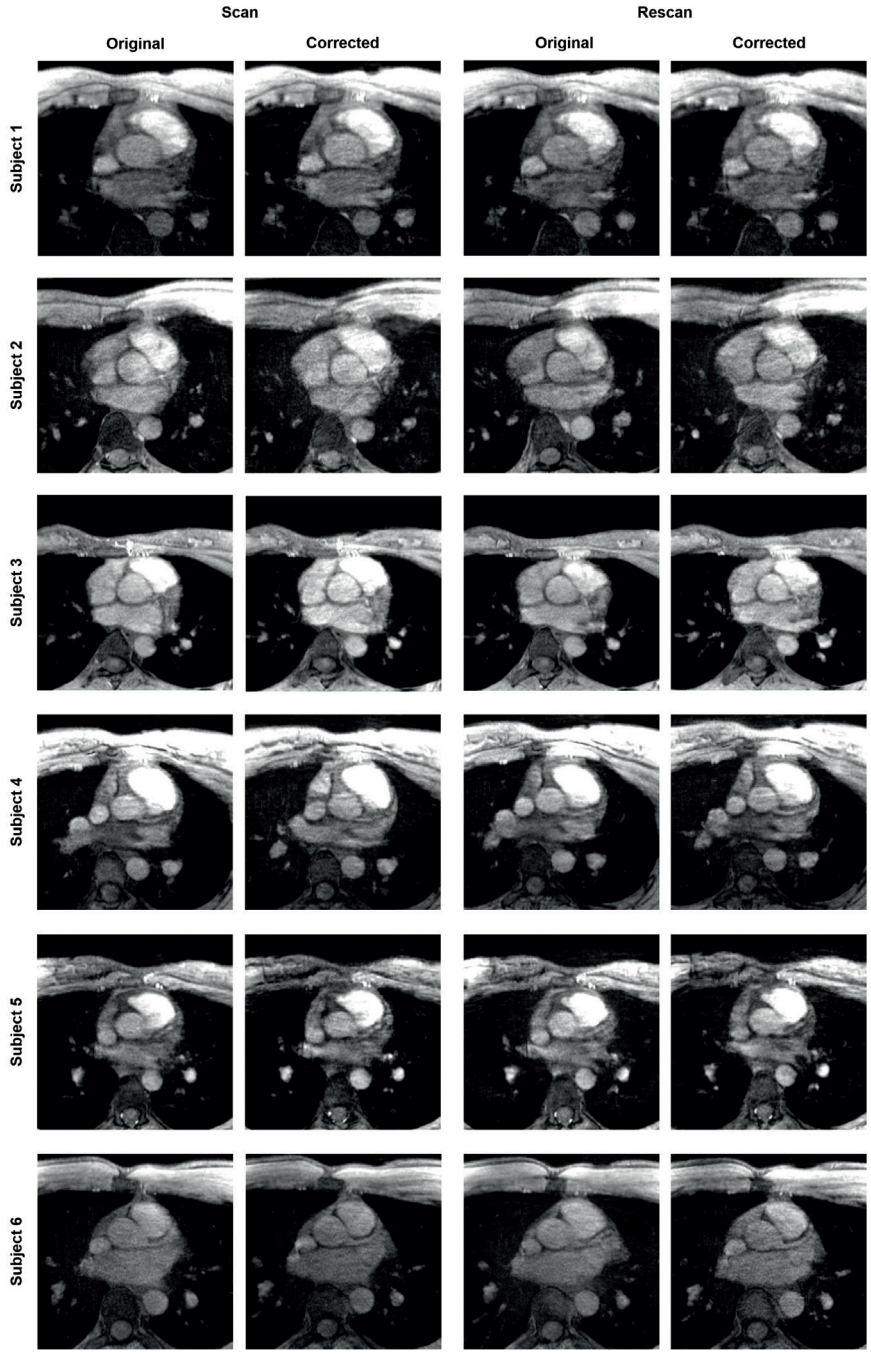

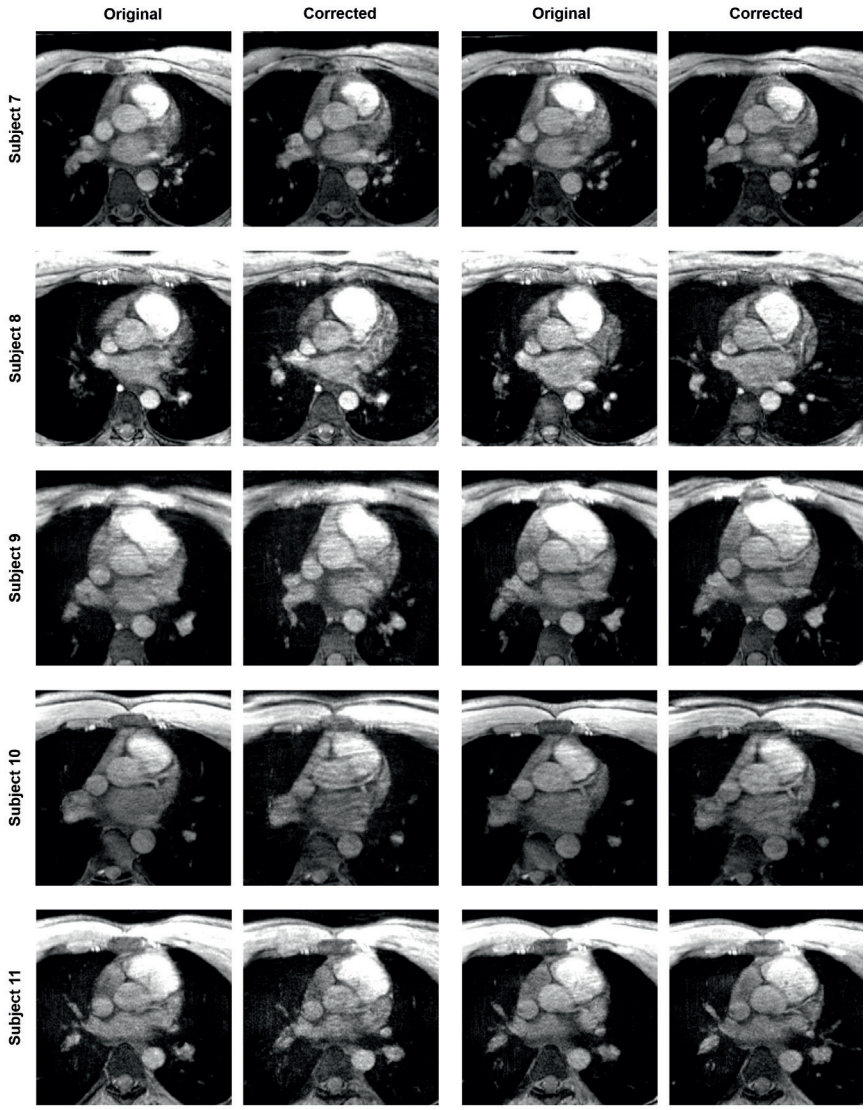

Supplemental Figure 6.1: overview of 4D flow MRI magnitude images, with and without correction for respiratory motion.

Supplemental Video 6.1 can be found online: https://www.frontiersin.org/articles/10.3389/fbioe.2021.725833/full#supplementary-material.

6.9 References

1. Fihn SD, Gardin JM, Abrams J, et al. 2012 ACCF/AHA/ACP/AATS/PCNA/SCAI/STS Guideline for the Diagnosis and Management of Patients With Stable Ischemic Heart Disease. J Am Coll Cardiol. 2012;60(24):e44–e164.
2. Montalescot G, Sechtem U, Achenbach S, et al. 2013 ESC guidelines on the management of stable coronary artery disease. Eur Heart J. 2013;34(38):2949–3003.
3. Motwani M, Swoboda PP, Plein S, Greenwood JP. Role of cardiovascular magnetic resonance in the management of patients with stable coronary artery disease. Heart. 2018;104(11):888–894.
4. Albrecht MH, Varga-Szemes A, Schoepf UJ, et al. Coronary artery assessment using self-navigated free-breathing radial whole-heart magnetic resonance angiography in patients with congenital heart disease. Eur Radiol. 2018;28(3):1267–1275.
5. Bustin A, Ginami G, Cruz G, et al. Five-minute whole-heart coronary MRA with sub-millimeter isotropic resolution, 100% respiratory scan efficiency, and 3D-PROST reconstruction. Magn Reson Med. 2019;81(1):102–115.
6. Roy CW, Heerfordt J, Piccini D, et al. Motion compensated whole-heart coronary cardiovascular magnetic resonance angiography using focused navigation (fNAV). J Cardiovasc Magn Reson. 2021;23(1):33.
7. Hofman MBM, van Rossum AC, Sprenger M, Westerhof N. Assessment of flow in the right human coronary artery by magnetic resonance phase contrast velocity measurement: Effects of cardiac and respiratory motion. Magn Reson Med. 1996;35(4):521–531.
8. Davis CP, Liu P-F, Hauser M, Göhde SC, Von Schulthess GK, Debatin JF. Coronary flow and coronary flow reserve measurements in humans with breath-held magnetic resonance phase contrast velocity mapping. Magn Reson Med. 1997;37(4):537–544.
9. Marcus JT, Smeenk HG, Kuijer JP, Van der Geest RJ, Heethaar RM, Van Rossum AC. Flow profiles in the left anterior descending and the right coronary artery assessed by MR velocity quantification: effects of through-plane and in-plane motion of the heart. J Comput Assist Tomogr. 1999;23(4):567–576.
10. Johnson K, Sharma P, Oshinski J. Coronary artery flow measurement using navigator echo gated phase contrast magnetic resonance velocity mapping at 3.0T. J Biomech. 2008;41(3):595–602.
11. Zhu D, Bonanno G, Hays AG, Weiss RG, Schär M. Phase contrast coronary blood velocity mapping with both high temporal and spatial resolution using triggered Golden Angle rotated Spiral k-t Sparse Parallel imaging (GASSP) with shifted binning. Magn Reson Med. 2021;86(4):1929-1943.
12. van de Hoef TP, van Lavieren MA, Damman P, et al. Physiological Basis and Long-Term Clinical Outcome of Discordance Between Fractional Flow Reserve and Coronary Flow Velocity Reserve in Coronary Stenoses of Intermediate Severity. Circ Cardiovasc Interv. 2014;7(3):301–311.
13. Murthy VL, Naya M, Foster CR, et al. Improved Cardiac Risk Assessment With Noninvasive Measures of Coronary Flow Reserve. Circulation. 2011;124(20):2215–2224.
14. Kato S, Saito N, Nakachi T, et al. Stress Perfusion Coronary Flow Reserve Versus Cardiac Magnetic Resonance for Known or Suspected CAD. J Am Coll Cardiol. 2017;70(7):869–879.
15. Markl M, Frydrychowicz A, Kozerke S, Hope M, Wieben O. 4D flow MRI. J Magn Reson Imaging. 2012;36(5):1015–1036.
16. Gottwald LM, Töger J, Markenroth Bloch K, et al. High Spatiotemporal Resolution 4D Flow MRI of Intracranial Aneurysms at 7T in 10 Minutes. Am J Neuroradiol. 2020;41(7):1201–1208.
17. Peper ES, Gottwald LM, Zhang Q, et al. Highly accelerated 4D flow cardiovascular magnetic resonance using a pseudo-spiral Cartesian acquisition and compressed sensing reconstruction for carotid flow and wall shear stress. J Cardiovasc Magn Reson. 2020;22(1):7.

18. Gottwald LM, Peper ES, Zhang Q, et al. Pseudo-spiral sampling and compressed sensing reconstruction provides flexibility of temporal resolution in accelerated aortic 4D flow MRI: A comparison with k-t principal component analysis. NMR Biomed. 2020;33(4):e4255.
19. Uecker M, Ong F, Tamir JI, et al. Berkeley Advanced Reconstruction Toolbox. Proc Intl Soc Mag Reson Med. 2015;23(1):2486.
20. Chen CC, Barnhart HX. Assessing agreement with intraclass correlation coefficient and concordance correlation coefficient for data with repeated measures. Comput Stat Data Anal. 2013;60(1):132–145.
21. Koo TK, Li MY. A Guideline of Selecting and Reporting Intraclass Correlation Coefficients for Reliability Research. J Chiropr Med. 2016;15(2):155–163.
22. Pizzuto F, Voci P, Mariano E, Emilio Puddu P, Sardella G, Nigri A. Assessment of flow velocity reserve by transthoracic Doppler echocardiography and venous adenosine infusion before and after left anterior descending coronary artery stenting. J Am Coll Cardiol. 2001;38(1):155–162.
23. Hozumi T, Yoshida K, Ogata Y, et al. Noninvasive Assessment of Significant Left Anterior Descending Coronary Artery Stenosis by Coronary Flow Velocity Reserve With Transthoracic Color Doppler Echocardiography. Circulation. 1998;97(16):1557–1562.
24. Ciampi Q, Zagatina A, Cortigiani L, et al. Functional, Anatomical, and Prognostic Correlates of Coronary Flow Velocity Reserve During Stress Echocardiography. J Am Coll Cardiol. 2019;74(18):2278–2291.
25. Kasprzak JD, Drozdz J, Peruga J, Rafalska K, Krzemińska-Pakuła M. Definition of Flow Parameters in Proximal Nonstenotic Coronary Arteries Using Transesophageal Doppler Echocardiography. Echocardiography. 2000;17(2):141–150.
26. Yamagishi M, Yasu T, Ohara K, Kuro M, Miyatake K. Detection of coronary blood flow associated with left main coronary artery stenosis by transesophageal doppler color flow echocardiography. J Am Coll Cardiol. 1991;17(1):87–93.
27. Yasu T, Yamagishi M, Shintaro Beppu, Nagata S, Kunio Miyatake. Left Main Coronary Flow Velocity Associated With Stenosis. Chest. 1993;104(3):690–693.
28. Wittfeldt A, Jeppsson A, Gan L-M. Effects of nitroglycerine on coronary flow velocity before and during adenosine provocation. Cardiovasc Ultrasound. 2016;14(1):48.
29. Ofili EO, Labovitz AJ, Kern MJ. Coronary flow velocity dynamics in normal and diseased arteries. Am J Cardiol. 1993;71(14):D3–D9.
30. Anderson HV, Stokes MJ, Leon M, Abu-Halawa SA, Stuart Y, Kirkeeide RL. Coronary Artery Flow Velocity Is Related To Lumen Area and Regional Left Ventricular Mass. Circulation. 2000;102(1):48–54.
31. van de Hoef TP, Echavarría-Pinto M, van Lavieren MA, et al. Diagnostic and Prognostic Implications of Coronary Flow Capacity. JACC Cardiovasc Interv. 2015;8(13):1670–1680.
32. Schiemann M, Bakhtiary F, Hietschold V, et al. MR-based coronary artery blood velocity measurements in patients without coronary artery disease. Eur Radiol. 2006;16(5):1124–1130.
33. Hundley WG, Lange RA, Clarke GD, et al. Assessment of Coronary Arterial Flow and Flow Reserve in Humans With Magnetic Resonance Imaging. Circulation. 1996;93(8):1502–1508.
34. Sakuma H, Koskenvuo JW, Niemi P, et al. Assessment of Coronary Flow Reserve Using Fast Velocity-Encoded Cine MR Imaging. Am J Roentgenol. 2000;175(4):1029–1033.
35. Shibata M, Sakuma H, Isaka N, Takeda K, Higgins CB, Nakano T. Assessment of coronary flow reserve with fast cine phase contrast magnetic resonance imaging: Comparison with measurement by Doppler guide wire. J Magn Reson Imaging. 1999;10(4):563–568.
36. Bedaux WLF, Hofman MBM, de Cock CC, Stoel MG, Visser CA, van Rossum AC. Magnetic resonance imaging versus Doppler guide wire in the assessment of coronary flow reserve in patients with coronary artery disease. Coron Artery Dis. 2002;13(7):365–372.

37. Nagel E, Thouet T, Klein C, et al. Noninvasive Determination of Coronary Blood Flow Velocity With Cardiovascular Magnetic Resonance in Patients After Stent Deployment. Circulation. 2003;107(13):1738–1743.
38. Keegan J, Raphael CE, Parker K, et al. Validation of high temporal resolution spiral phase velocity mapping of temporal patterns of left and right coronary artery blood flow against Doppler guidewire. J Cardiovasc Magn Reson. 2015;17:85.
39. Ibrahim T, Nekolla SG, Schreiber K, et al. Assessment of coronary flow reserve: Comparison between contrast-enhanced magnetic resonance imaging and positron emission tomography. J Am Coll Cardiol. 2002;39(5):864–870.
40. Lund GK, Watzinger N, Saeed M, et al. Chronic Heart Failure: Global Left Ventricular Perfusion and Coronary Flow Reserve with Velocity-Encoded Cine MR Imaging: Initial Results. Radiology. 2003;227(1):209–215.
41. Aras A, Anik Y, Demirci A, et al. Magnetic resonance imaging measurement of left ventricular blood flow and coronary flow reserve in patients with chronic heart failure due to coronary artery disease. Acta Radiol. 2007;48(10):1092–1100.
42. Pelletier-Galarneau M, DeKemp RA, Hunter CRRN, et al. Effects of Hypercapnia on Myocardial Blood Flow in Healthy Human Subjects. J Nucl Med. 2018;59(1):100–106.
43. Heo R, Nakazato R, Kalra D, Min JK. Noninvasive imaging in coronary artery disease. Semin Nucl Med. 2014;44(5):398–409.
44. Alexanderson-Rosas E, Guinto-Nishimura GY, Cruz-Mendoza JR, et al. Current and future trends in multimodality imaging of coronary artery disease. Expert Rev Cardiovasc Ther. 2015;13(6):715–731.
45. Smulders MW, Jaarsma C, Nelemans PJ, et al. Comparison of the prognostic value of negative non-invasive cardiac investigations in patients with suspected or known coronary artery disease–a meta-analysis. Eur Hear J - Cardiovasc Imaging. 2017;18(9):980–987.
46. Ma L, Yerly J, Piccini D, et al. 5D flow MRI: a fully self-gated, free-running framework for cardiac and respiratory motion–resolved 3D hemodynamics. Radiology: Cardiothoracic Imaging. 2020;2:e200219.
47. Feng L, Coppo S, Piccini D, et al. 5D whole-heart sparse MRI. Magn Reson Med. 2018;79:826–838.
48. Dodge JTJ, Brown BG, Bolson EL, Dodge HT. Lumen diameter of normal human coronary arteries. Influence of age, sex, anatomic variation, and left ventricular hypertrophy or dilation. Circulation. 1992;86(1):232–246.
49. Tang C, Blatter DD, Parker DL. Accuracy of phase-contrast flow measurements in the presence of partial-volume effects. J Magn Reson Imaging. 1993;3(2):377–385.
50. Dyverfeldt P, Ebbers T. Comparison of respiratory motion suppression techniques for 4D flow MRI. Magn Reson Med. 2017;78(5):1877–1882.
51. Glover GH, Pauly JM. Projection Reconstruction Techniques for Reduction of Motion Effects in MRI. Magn Reson Med. 1992;28(2):275–289.

General discussion and summaries

7

7.1 General discussion

In this thesis, we have seen that cardiac 4D flow MRI has much to offer for evaluation of valvular heart disease and coronary artery disease. Yet, its value should not be overstated, nor taken for granted. In the following, I will address various technical, scientific and clinical aspects that together shape the success of cardiac 4D flow MRI. In doing so, I will touch upon hurdles and opportunities in its innovation, validation and clinical use.

Een goed begin is het halve werk...

7.1.1 Acquisition-related considerations

There's no such thing as a standard cardiac 4D flow MRI acquisition. Possibilities are endless, especially when it comes to k-space trajectories. Different sampling strategies each have their own advantages and disadvantages. One could for instance argue that EPI is not to be advised for the characterization of high-velocity regions because of its long echo times and, thus, susceptibility to velocity misregistration. On the other hand, PROUD is more prone to errors during image reconstruction, as it uses incomplete measurement data. To what extent the latter affects the soundness of the final results has been a subject of research in studies applying PROUD to the aorta, carotid arteries and intracranial arteries (1–3). Those studies suggest that undersampling factors of 20 to 30 can be reached without significant image degradation compared to only minimally accelerated 2D flow MRI. Yet, caution is advised when one is interested in local details like peak velocities (1–4).

Important considerations in choosing an acquisition strategy also include the size of the anatomical region of interest relative to the degree of respiratory motion, and the dimensions of the field of view. While radial sampling might make coronary 4D flow MRI more robust against respiratory motion, it requires the field of view to be cubic, which would add scan time to the already lengthy acquisitions in Chapter 6. EPI readout would not suit that coronary 4D flow MRI framework either: the image registration-based respiratory motion correction we performed relies on reconstructions of each one eighth of the acquired data. Using EPI, these images would contain severe artifacts, as in EPI image reconstruction image sparsity is not exploited.

Once settled on a k-space sampling pattern, settings like spatial resolution, temporal resolution or frame rate, and VENC may vary depending on what pathology and hemodynamic parameters are studied (5). While choosing a spatial and temporal resolution is not rocket science, the VENC often turns out to be a stumbling block. Setting the VENC too high results in poor velocity contrast; setting it too low results in phase wrapping, but knowing what is "too high" or "too low" requires a-priori knowledge of the patient-specific peak velocity. 2D flow MRI scout scans are helpful, but only when positioned correctly. Moreover, as a result of larger slice thickness (typically 8 mm) in 2D flow MRI, local peak velocities can appear lower due to averaging with surrounding velocities. One way of dealing with this issue is to accept some phase wrapping and correct for it during post-processing. In Chapter 4 and 5, this is done by enforcing spatiotemporal continuity on the velocity fields using a Laplacian-based algorithm (6). A recently introduced weighted least-squares method with a divergence-free constraint is even capable of resolving double wraps, and can denoise the data to improve the velocity-to-noise ratio (7). Another way of avoiding phase wrapping in high-velocity regions while maintaining good contrast in low-velocity regions is offered by dual-VENC or even triple-VENC acquisition, albeit at the cost of 75% longer scan time (8,9). A variation on dual-VENC acquisition, using different VENCs for systole and diastole, does not add extra scan time (10).

Last but not least, respiratory motion compensation is particularly important for high-spatial resolution acquisitions (11). Whereas it can be omitted in whole-heart 4D flow MRI to save scan time (12–14), it is absolutely necessary in coronary 4D flow MRI (15). Nevertheless, in Chapter 5, respiratory gating with 60% acceptance was shown to have an effect on whole-heart 4D flow MRI image quality and valvular flow measurement results. Perhaps the most elegant way to correct for respiratory motion is to apply self-navigation with 100% acceptance. This however requires frequent sampling of the center of k-space, which the Cartesian sequences we used do not allow.

... maar een goed begin is maar de helft.

7.1.2 Analysis-related considerations

Having your acquisition strategy in order is one thing, but how you proceed with the acquired data is at least as important: without the right post-processing and data analysis methods you will never get to meaningful results, or you may even end up with incorrect results. The only difference between flow tracking and valve tracking

in the quantification of MV regurgitation is the positioning of the analysis plane along the regurgitant jet. Yet, those one or two centimeters can make a clinically meaningful difference, as we have seen in Chapter 3. Hence, in setting up an analysis protocol, it is important to be aware of the limitations of the acquisition – in this case the spatial resolution – to minimize their impact on the results.

No matter how detailed an analysis protocol is, manual steps will always introduce inter- and intra-observer variability. Chapter 3 showed that a more reproducible method is needed for the quantification of severe mitral valve regurgitation with multiple jets. This method should prevent jets from being overlooked, provide standardized placement of the analysis plane and offer reproducible contouring of the flow area. To that end, automatic jet detection by three-dimensional mapping of turbulent kinetic energy or velocity direction could prove useful (16,17). Plane placement could perhaps be standardized or even be automated based on a minimal jet diameter and maximal velocity (gradient). An isoline representation of the phase image might facilitate (semi)automatic contouring of the flow area. Not only would these refinements help to reduce human error, they would also save analysis time.

7.1.3 Sequence validation

Throughout this thesis, two main methods were used to evaluate measurement results for their correctness: comparison with 2D (flow) MRI results and intervalve consistency testing. The latter gives an indication of the overall robustness of the measurements and can serve as a guide even *during* the analysis – for instance, to discover undiagnosed valve regurgitation. On the other hand, being led too much by interim results can cause actual measurement inaccuracies to be concealed. In Chapter 4, a trend was observed of lower flow volumes across the aortic and pulmonary valve than across the atrioventricular valves when using EPI. During data analysis, we observed that these differences tend to diminish when shifting the analysis plane more downstream. Should we have done so, the results would not have reflected the soundness of the data, but rather our ability to tweak the analysis such that the results match our expectations. It is our responsibility to question why the results *don't* match our expectations: in this specific example, this was likely due to velocity misregistration caused by EPI readout (18). At the same time, in Chapter 3, we also shifted the analysis plane to achieve better results. We did so to avoid intravoxel phase dispersion and turbulence effects, but cannot deny that velocity misregistration may have played a role as well. Hence, in evaluating the robustness of a cardiac 4D flow

MRI acquisition, one should always take into account the intervalve consistency but not blindly rely on it.

In the absence of a gold standard measurement technique in vivo, phantom experiments provide a way to validate 4D flow MRI sequences in vitro (14,19–21). The PROUD sequence used in this thesis was validated in a pulsatile flow phantom mimicking carotid artery hemodynamics (2). A whole-heart flow phantom is yet to be developed, possibly by 3D printing (22,23), although an ex-vivo resuscitated pig heart setup offers a promising alternative (24,25).

7.1.4 Computational fluid dynamics and data assimilation

A completely different take on the characterization of blood flow patterns is offered by the field of computational fluid dynamics (CFD). Instead of *measuring* the blood's behavior, CFD *models* it, based on physical laws of fluid dynamics like the Navier-Stokes equations. As such, it can be used to predict the hemodynamic impact of surgical intervention (26–28). CFD is also used for wall shear stress estimation in arterial aneurysms (29), as it offers higher spatial and temporal resolution than 4D flow MRI. A limitation to CFD is that it requires highly accurate anatomical information and in- and outflow profiles, which are hard to acquire in vivo.

An approach called data assimilation combines the best of both worlds. By fusing in-vivo measured data with an underlying mathematical model, it provides a way to reconstruct physics-abiding flow fields from low-resolution, noisy data (30). Originating from climatology, data assimilation is rapidly gaining ground in other fields (31,32). Its application to intracranial 4D flow MRI (33–36) suggests it could prove useful for denoising and enhancing the resolution of coronary 4D flow MRI too.

7.1.5 Outlook

In the past two decades, 4D flow MRI research has evolved from a mostly preclinical to a more clinical setting. Still, 4D flow MRI has not appeared in many clinical guidelines yet (37). Its added value over current diagnostic methods remains to be more thoroughly assessed in longitudinal studies. It is only by linking clinical outcomes to measured parameters that the prognostic value of 4D flow MRI can reliably be assessed. This clinical test phase can eventually lead to widespread clinical adaptation, if collective efforts are made to 1) make the scattered landscape of different vendors, sequences and software tools easier to navigate for centers without expertise in 4D flow MRI, and

to 2) get validated sequences and software tools approved for clinical use. Individual centers will have to get the necessary IT infrastructure in place to handle the large amounts of data (38), and have personnel trained for its analysis.

To lower the threshold for routine clinical application of 4D flow MRI, time-consuming data analysis procedures could be automated or be assisted by machine learning methods (39–41). Furthermore, 2D cine bSSFP could eventually be replaced by a single 3D cine bSSFP scan (42,43), shortening cardiac MRI protocols and leaving space for a 4D flow MRI scan to be added.

7.1.6 References

1. Gottwald LM, Peper ES, Zhang Q, et al. Pseudo-spiral sampling and compressed sensing reconstruction provides flexibility of temporal resolution in accelerated aortic 4D flow MRI: A comparison with k-t principal component analysis. NMR Biomed. 2020;33(4):e4255.
2. Peper ES, Gottwald LM, Zhang Q, et al. Highly accelerated 4D flow cardiovascular magnetic resonance using a pseudo-spiral Cartesian acquisition and compressed sensing reconstruction for carotid flow and wall shear stress. J Cardiovasc Magn Reson. 2020;22(1):7.
3. Gottwald LM, Töger J, Markenroth Bloch K, et al. High Spatiotemporal Resolution 4D Flow MRI of Intracranial Aneurysms at 7T in 10 Minutes. Am J Neuroradiol. 2020;41(7):1201–1208.
4. Blanken CPS, Gottwald LM, Westenberg JJM, et al. Whole-Heart 4D Flow MRI for Evaluation of Normal and Regurgitant Valvular Flow: A Quantitative Comparison Between Pseudo-Spiral Sampling and EPI Readout. J. Magn. Reson. Imaging. 2021.
5. Dyverfeldt P, Bissell M, Barker AJ, et al. 4D flow cardiovascular magnetic resonance consensus statement. J Cardiovasc Magn Reson. 2015;17(1):72.
6. Loecher M, Schrauben E, Johnson KM, Wieben O. Phase unwrapping in 4D MR flow with a 4D single-step Laplacian algorithm. J Magn Reson Imaging. 2016;43(4):833–842.
7. Zhang J, Rothenberger SM, Brindise MC, et al. Divergence-Free Constrained Phase Unwrapping and Denoising for 4D Flow MRI Using Weighted Least-Squares. IEEE Trans. Med. Imaging. 2021.
8. Schnell S, Ansari SA, Wu C, et al. Accelerated dual-venc 4D flow MRI for neurovascular applications. J Magn Reson Imaging. 2017;46(1):102–114.
9. Ma LE, Markl M, Chow K, Vali A, Wu C, Schnell S. Efficient triple-VENC phase-contrast MRI for improved velocity dynamic range. Magn Reson Med. 2020;83(2):505–520.
10. Callahan S, Singam NS, Kendrick M, et al. Dual-VENC acquisition for 4D flow MRI in aortic stenosis with spiral readouts. J Magn Reson Imaging. 2020;52(1):117–128.
11. Dyverfeldt P, Ebbers T. Comparison of respiratory motion suppression techniques for 4D flow MRI. Magn Reson Med. 2017;78(5):1877–1882.
12. Kanski M, Töger J, Steding-Ehrenborg K, et al. Whole-heart four-dimensional flow can be acquired with preserved quality without respiratory gating, facilitating clinical use: a head-to-head comparison. BMC Med Imaging. 2015;15(1):1–13.
13. Garg P, Westenberg JJM, van den Boogaard PJ, et al. Comparison of fast acquisition strategies in whole-heart four-dimensional flow cardiac MR: Two-center, 1.5 Tesla, phantom and in vivo validation study. J Magn Reson Imaging. 2018;47(1):272–281.
14. Bock J, Töger J, Bidhult S, et al. Validation and reproducibility of cardiovascular 4D-flow MRI from two vendors using 2 × 2 parallel imaging acceleration in pulsatile flow phantom and in vivo with and without respiratory gating. Acta radiol. 2019;60(3):327–337.
15. Blanken CPS, Schrauben EM, Peper ES, et al. Coronary Flow Assessment Using Accelerated 4D Flow MRI With Respiratory Motion Correction. Front Bioeng Biotechnol. 2021;9:729.
16. Dyverfeldt P, Kvitting J-PE, Carlhäll CJ, et al. Hemodynamic aspects of mitral regurgitation assessed by generalized phase-contrast MRI. J Magn Reson Imaging. 2011;33(3):582–588.
17. van Ooij P, Farag ES, Blanken CPS, et al. Fully quantitative mapping of abnormal aortic velocity and wall shear stress direction in patients with bicuspid aortic valves and repaired coarctation using 4D flow cardiovascular magnetic resonance. J Cardiovasc Magn Reson. 2021;23(1):9.
18. Dillinger H, Walheim J, Kozerke S. On the limitations of echo planar 4D flow MRI. Magn Reson Med. 2020;84(4):1806–1816.
19. Ebel S, Hübner L, Köhler B, et al. Validation of two accelerated 4D flow MRI sequences at 3 T: a phantom study. Eur Radiol Exp. 2019;3(1):10.
20. David A, Le Touze D, Warin-Fresse K, et al. In-vitro validation of 4D flow MRI measurements with an experimental pulsatile flow model. Diagn Interv Imaging. 2019;100(1):17–23.

21. Corrado PA, Medero R, Johnson KM, François CJ, Roldán-Alzate A, Wieben O. A phantom study comparing radial trajectories for accelerated cardiac 4D flow MRI against a particle imaging velocimetry reference. Magn Reson Med. 2021;86(1):363–371.
22. Filippou V, Tsoumpas C. Recent advances on the development of phantoms using 3D printing for imaging with CT, MRI, PET, SPECT, and ultrasound. Med Phys. 2018;45(9):e740–e760.
23. Hussein N, Voyer-Nguyen P, Portnoy S, et al. Simulation of semilunar valve function: computer-aided design, 3D printing and flow assessment with MR. 3D Print Med. 2020;6(1):2.
24. Peper ES, Leopaldi AM, van Tuijl S, et al. An isolated beating pig heart platform for a comprehensive evaluation of intracardiac blood flow with 4D flow MRI: a feasibility study. Eur Radiol Exp. 2019;3(1):40.
25. Escher A, Choi Y, Callaghan F, et al. A Valveless Pulsatile Pump for Heart Failure with Preserved Ejection Fraction: Hemo- and Fluid Dynamic Feasibility. Ann Biomed Eng. 2020;48(6):1821–1836.
26. Hellmeier F, Brüning J, Sündermann S, et al. Hemodynamic Modeling of Biological Aortic Valve Replacement Using Preoperative Data Only. Front Cardiovasc Med. 2021;7:408.
27. Loke Y-H, Capuano F, Balaras E, Olivieri LJ. Computational Modeling of Right Ventricular Motion and Intracardiac Flow in Repaired Tetralogy of Fallot. Cardiovasc. Eng. Technol. 2021.
28. Lantz J, Bäck S, Carlhäll C-J, et al. Impact of prosthetic mitral valve orientation on the ventricular flow field: Comparison using patient-specific computational fluid dynamics. J Biomech. 2021;116:110209.
29. Lipp SN, Niedert EE, Cebull HL, et al. Computational Hemodynamic Modeling of Arterial Aneurysms: A Mini-Review. Front Physiol. 2020;11:454.
30. D'Elia M, Perego M, Veneziani A. A Variational Data Assimilation Procedure for the Incompressible Navier-Stokes Equations in Hemodynamics. J Sci Comput. 2011;52(2):340–359.
31. Dahmen W, Stevenson R, Westerdiep J. Accuracy controlled data assimilation for parabolic problems. Math. Comput. 2021.
32. Karniadakis GE, Kevrekidis IG, Lu L, Perdikaris P, Wang S, Yang L. Physics-informed machine learning. Nat Rev Phys. 2021;3(6):422–440.
33. Funke SW, Nordaas M, Evju Ø, Alnaes MS, Mardal KA. Variational data assimilation for transient blood flow simulations: Cerebral aneurysms as an illustrative example. Int j numer method biomed eng. 2019;35(1):e3152.
34. Gaidzik F, Pathiraja S, Saalfeld S, et al. Hemodynamic Data Assimilation in a Subject-specific Circle of Willis Geometry. Clin Neuroradiol. 2021;31(3):643–651.
35. Töger J, Zahr MJ, Aristokleous N, Markenroth Bloch K, Carlsson M, Persson P. Blood flow imaging by optimal matching of computational fluid dynamics to 4D-flow data. Magn Reson Med. 2020;84(4):2231–2245.
36. Habibi M, D'Souza RM, Dawson STM, Arzani A. Integrating multi-fidelity blood flow data with reduced-order data assimilation. Comput Biol Med. 2021;135:104566.
37. Borger MA, Fedak PWM, Stephens EH, et al. The American Association for Thoracic Surgery consensus guidelines on bicuspid aortic valve–related aortopathy: Full online-only version. J Thorac Cardiovasc Surg. 2018;156(2):e41–e74.
38. Gottwald LM, Nelissen JL, Planken RN, den Harder C, Groot PFC. Closing the gap between research and clinical practice: The 4D flow MRI example. MT Integr. 2020.
39. Retson TA, Besser AH, Sall S, Golden D, Hsiao A. Machine Learning and Deep Neural Networks in Thoracic and Cardiovascular Imaging. J Thorac Imaging. 2019;34(3):192–201.
40. Berhane H, Scott M, Elbaz M, et al. Fully automated 3D aortic segmentation of 4D flow MRI for hemodynamic analysis using deep learning. Magn Reson Med. 2020;84(4):2204–2218.
41. Garcia J, Beckie K, Hassanabad AF, Sojoudi A, White JA. Aortic and mitral flow quantification using dynamic valve tracking and machine learning: Prospective study assessing static and dynamic plane repeatability, variability and agreement. JRSM Cardiovasc Dis. 2021;10:1–8.

42. Küstner T, Bustin A, Jaubert O, et al. Isotropic 3D Cartesian single breath-hold CINE MRI with multi-bin patch-based low-rank reconstruction. Magn Reson Med. 2020;84(4):2018–2033.
43. Muscogiuri G, Gatti M, Dell'Aversana S, et al. Reliability of single breath hold three-dimensional cine kat-ARC for the assessment of biventricular dimensions and function. Eur J Radiol. 2020;124:108820.

7.2 Summary

Unlike X-ray, CT, PET and SPECT, which image body tissues based on their interaction with ionizing radiation, MRI exploits the tissues' interaction with a magnetic field and radio waves. It does so non-invasively, without harming the body, and has become a popular imaging technique in hospitals all over the world. Not only does it allow for the imaging of tissues, it can also measure blood flow velocities, making it a useful technique for the assessment of cardiac disease. Currently, MRI-based assessment of cardiac hemodynamics largely relies on 2D flow MRI, which can characterize blood flow in two-dimensional imaging planes over time. 4D flow MRI offers three-dimensional velocity measurement over time.

In 4D flow MRI, two-dimensional analysis planes are placed during post-processing. Those planes can have any location within the scanned volume, and can even be made to follow the motion of the heart valves, a technique called valve tracking. For the quantification of valvular regurgitation (i.e. leakage), a variation on valve tracking has been proposed: flow tracking, to avoid flow underestimation caused by large local velocity differences and turbulence at the level of the valve.

Accelerated measurement strategies have enabled whole-heart 4D flow MRI at scan times of approximately ten minutes. In this thesis, two accelerated 4D flow MRI techniques are used: echo planar imaging (EPI) and pseudo-spiral sampling (PROUD) 4D flow MRI.

Chapter 2 reviews various 4D flow MRI-derived hemodynamic parameters, together with their diagnostic and prognostic potential for the evaluation of left-sided valvular heart disease (VHD). Furthermore, the role of MRI-based myocardial tissue mapping and left-ventricular strain quantification is discussed. We conclude that 4D flow MRI, tissue mapping and strain quantification provide valuable information for the diagnosis and quantitative assessment of left-sided VHD. Future research should include longitudinal studies to further investigate their prognostic value.

In **Chapter 3**, flow tracking is compared with valve tracking for the quantification of mild, moderate and severe mitral valve (MV) regurgitation. We find that flow tracking provides more accurate quantification of MV regurgitation than valve tracking in terms of agreement with conventional cardiac MRI and intervalve consistency,

particularly in severe MV regurgitation. Interobserver analysis demonstrates moderate reproducibility for valve tracking and excellent reproducibility for flow tracking, but also highlights the need for a more reproducible flow tracking method in the quantification of severe MV regurgitation with multiple regurgitation jets.

In **Chapter 4**, we investigate the robustness of whole-heart PROUD 4D flow MRI for quantification of normal and regurgitant blood flow across the heart valves. We compare its performance to that of EPI 4D flow MRI in terms of intervalve consistency and agreement with conventional cardiac MRI, and investigate the possibility of shortening the scan time further by retrospectively increasing the undersampling factor. Our findings suggest that PROUD 4D flow MRI is a reliable technique for intracardiac flow quantification in under 10 minutes, and scan times may be shortened by an additional 75% in healthy subjects and 50% in patients with valvular regurgitation.

In 4D flow MRI, respiratory (i.e. breathing) motion is typically monitored using a method called lung-liver interface navigation. A novel, camera-based, method records the motion of the breast cage and allows for a higher frame rate. In **Chapter 5**, camera-based respiratory monitoring is compared with lung-liver navigator-based respiratory monitoring in a cohort of patients with congenital and/or valvular heart disease. The acquired signals are used for respiratory gating with 60% acceptance. A high correlation is found between the phases of the two signals. Both techniques are shown to have an effect on quantitatively assessed image quality and valvular flow measurements compared to no gating.

4D flow MRI has also been applied to the aorta, pulmonary arteries, carotid arteries, intracranial arteries and abdominal arteries and veins. These application territories all are part of either the systemic or the pulmonary circulation. The *coronary* circulation has remained unexplored by 4D flow MRI. **Chapter 6** presents a framework for coronary blood flow quantification using PROUD 4D flow MRI equipped with 100%-acceptance respiratory motion correction. We achieve a spatial resolution of 1.0 mm^3 at a scan time of approximately 12 minutes, and improved image quality compared to no respiratory motion correction. Our results demonstrate good reproducibility and good agreement with 2D flow MRI-based flow and velocity measurements.

7.3 Nederlandse samenvatting

In tegenstelling tot röntgen, CT, PET en SPECT, die gebruik maken van ioniserende straling voor het in beeld brengen van lichaamsweefsels, is de werking van MRI gebaseerd op de interactie van weefsels met een magnetisch veld en radiogolven. MRI is non-invasief en niet schadelijk voor het lichaam, en mede daarom een populaire techniek in ziekenhuizen wereldwijd. Niet alleen weefsels, maar ook bloedstroompatronen kunnen ermee in beeld gebracht worden, bijvoorbeeld voor het diagnosticeren van hart- en vaatziekten. Voor dit laatste wordt vooralsnog meestal 2D flow MRI gebruikt, wat de bloedstroom in tweedimensionale meetvlakken in kaart kan brengen. 4D flow MRI kan dit in een volume over de tijd.

Na het meten van een snelheidsveld met 4D flow MRI kan met behulp van meetvlakken aan de bloedstroom worden gemeten. Het is zelfs mogelijk om de meetvlakken te laten meebewegen met de hartkleppen. Dit wordt valve tracking genoemd. Voor het meten aan een lekkende hartklep is een variatie op valve tracking geïntroduceerd: flow tracking. Dit om te voorkomen dat de meting te laag uitvalt vanwege grote snelheidsverschillen en turbulentie ter hoogte van de hartklep.

Dankzij geavanceerde versnellingstechnieken is het mogelijk om in ongeveer tien minuten een 4D flow-scan van het gehele hart te maken. In dit proefschrift komen twee versnelde 4D flow MRI-technieken aan bod: echo planar imaging (EPI) en pseudo-spiral sampling (PROUD).

Hoofdstuk 2 behandelt verschillende hemodynamische parameters die met 4D flow MRI bepaald kunnen worden, samen met hun diagnostische en eventuele prognostische waarde voor het beoordelen van hartklepaandoeningen in het linkerhart. Ook worden twee andere MRI-technieken besproken, waarmee de structuur en functie van de hartspier kan worden beoordeeld. We concluderen dat deze drie MRI-technieken waardevolle informatie opleveren voor het diagnosticeren van en meten aan linkszijdige hartklepaandoeningen. De prognostische waarde van de technieken zal uit toekomstige langetermijnstudies moeten blijken.

In **Hoofdstuk 3** wordt flow tracking met valve tracking vergeleken voor de kwantificatie van milde, middelmatige en ernstige mitralisregurgitatie (d.w.z. een lekkende mitralisklep). We zien dat flow tracking nauwkeuriger is dan valve tracking

in het meten van het lekkende bloedvolume in termen van 1) overeenstemming met conventionele MRI-metingen en 2) consistentie van de meetresultaten tussen de verschillende hartkleppen. Reproduceerbaarheid van de meetresultaten bij beoordeling door een tweede persoon is middelmatig bij gebruik van valve tracking, en uitstekend bij gebruik van flow tracking. Wel komt aan het licht dat de reproduceerbaarheid van flow tracking voor het kwantificeren van ernstige mitralisregurgitatie verbeterd moet worden.

In **Hoofdstuk 4** onderzoeken we de betrouwbaarheid van *whole-heart* PROUD 4D flow MRI voor het meten aan normale en lekkende bloedstromen over de hartkleppen. We vergelijken de meetresultaten van PROUD met die van EPI op grond van 1) overeenstemming met conventionele MRI-metingen en 2) consistentie van de meetresultaten tussen de verschillende hartkleppen. Ook onderzoeken we de mogelijkheid om de scantijd verder te verkorten, naar minder dan tien minuten. Onze bevindingen zijn dat PROUD 4D flow MRI een betrouwbare techniek is voor het kwantificeren van bloedstromen in het hart, en dat de scantijd met nog eens 75% verkort kan worden in gezonde vrijwilligers en 50% in patiënten met een lekkende hartklep.

Ademhalingsbeweging wordt in 4D flow MRI typisch gemonitord door middel van een methode geheten long-lever-navigatie. Een nieuwe methode meet de beweging van de borstkas met een camera en heeft een hogere frame rate. In **Hoofdstuk 5** worden deze twee methoden met elkaar vergeleken in een groep patiënten met congenitale hartafwijkingen en/of hartklepaandoeningen. Op basis van de meetsignalen worden alleen 4D flow MRI-metingen meegenomen die tijdens eind-uitademing zijn gedaan. De twee signalen vertonen een hoge correlatie. Verder hebben ze beiden een positief effect op de kwaliteit van de beelden en op metingen van bloedstroom over de hartkleppen.

4D flow MRI heeft ook toepassingen in de aorta, longslagaders, halsslagaders, en bloedvaten in het brein en in de buik. Deze toepassingsgebieden maken allemaal deel uit van ofwel de grote ofwel de kleine bloedsomloop. De bloedsomloop door de *kransvaten* was tot op heden onontgonnen terrein voor 4D flow MRI. In **Hoofdstuk 6** presenteren we een manier om PROUD 4D flow MRI op de kransslagaderen toe te passen. We bereiken een spatiële resolutie van 1.0 mm^3 in een scantijd van ongeveer 12 minuten, en verbeteren de beeldkwaliteit door middel van ademhalingscompensatie. De resultaten zijn reproduceerbaar en vertonen goede overeenstemming met 2D flow MRI-metingen.

Appendices

8

8.1 List of publications

- **Blanken CPS**, Farag ES, Boekholdt SM, Leiner T, Kluin J, Nederveen AJ, van Ooij P, Planken RN. Advanced cardiac MRI techniques for evaluation of left-sided valvular heart disease. J Magn Reson Imaging. 2018;48(2):318–329.

- Ma LE, Vali A, **Blanken CPS**, Barker AJ, Malaisrie C, McCarthy P, Collins JD, Carr JC, Schnell S, Markl M. Altered Aortic 3-Dimensional Hemodynamics in Patients With Functionally Unicuspid Aortic Valves. Circ Cardiovasc Imaging. 2018;11(8):e007915.

- **Blanken CPS**, Westenberg JJM, Aben J-P, Bijvoet GP, Chamuleau SAJ, Boekholdt SM, Nederveen AJ, Leiner T, van Ooij P, Planken RN. Quantification of Mitral Valve Regurgitation from 4D Flow MRI Using Semiautomated Flow Tracking. Radiol Cardiothorac Imaging. 2020;2(5):e200004.

- Rahman O, Markl M, Balte P, Berhane H, **Blanken CPS**, Suwa K, Dashnaw S, Wieben O, Bluemke DA, Prince MR, Lima J, Michos E, Ambale-Venkatesh B, Hoffman EA, Gomes AS, Watson K, Sun Y, Carr J, Barr RG. Reproducibility and Changes in Vena Caval Blood Flow by Using 4D Flow MRI in Pulmonary Emphysema and Chronic Obstructive Pulmonary Disease (COPD): The Multi-Ethnic Study of Atherosclerosis (MESA) COPD Substudy. Radiology. 2019;292(3):585–594.

- Juffermans JF, Minderhoud SCS, Wittgren J, Kilburg A, Ese A, Fidock B, Zheng Y-C, Zhang J-M, **Blanken CPS**, Lamb HJ, Goeman JJ, Carlsson M, Zhao S, Planken RN, van Ooij P, Zhong L, Chen X, Garg P, Emrich T, Hirsch A, Töger J, Westenberg JJM. Multicenter Consistency Assessment of Valvular Flow Quantification With Automated Valve Tracking in 4D Flow CMR. JACC Cardiovasc Imaging. 2021;14(7):1354–1366.

- Gottwald LM, **Blanken CPS**, Tourais J, Smink J, Planken RN, Boekholdt SM, Meijboom LJ, Coolen BF, Strijkers GJ, Nederveen AJ, van Ooij P. Retrospective Camera-Based Respiratory Gating in Clinical Whole-Heart 4D Flow MRI. J Magn Reson Imaging. 2021;54(2):440–451.

- Demirkiran A, van Ooij P, Westenberg JJM, Hofman MBM, van Assen HC, Schoonmade LJ, Asim U, **Blanken CPS**, Nederveen AJ, van Rossum AC, Götte MJW. Clinical intra-

cardiac 4D flow CMR: acquisition, analysis, and clinical applications. Eur Hear J - Cardiovasc Imaging. 2021;00:1–12.

- **Blanken CPS**, Schrauben EM, Peper ES, Gottwald LM, Coolen BF, van Wijk DF, Piek JJ, Strijkers GJ, Planken RN, van Ooij P, Nederveen AJ. Coronary Flow Assessment Using Accelerated 4D Flow MRI With Respiratory Motion Correction. Front Bioeng Biotechnol. 2021;9:729.

- **Blanken CPS**, Gottwald LM, Westenberg JJM, Peper ES, Coolen BF, Strijkers GJ, Nederveen AJ, Planken RN, Ooij P. Whole-Heart 4D Flow MRI for Evaluation of Normal and Regurgitant Valvular Flow: A Quantitative Comparison Between Pseudo-Spiral Sampling and EPI Readout. J Magn Reson Imaging. 2021.

- van Ooij P, Farag ES, **Blanken CPS**, Nederveen AJ, Groenink M, Planken RN, Boekholdt SM. Fully quantitative mapping of abnormal aortic velocity and wall shear stress direction in patients with bicuspid aortic valves and repaired coarctation using 4D flow cardiovascular magnetic resonance. J Cardiovasc Magn Reson. 2021;23(1):9.

8.2 PhD portfolio

Name PhD student: Carmen P.S. Blanken
PhD period: January 2018 – June 2021
Supervisor: prof. dr. Aart J. Nederveen
Co-supervisors: dr. R. Nils Planken and dr. ir. Pim van Ooij

PhD training	Year	ECTS
Courses		
Basiscursus Regelgeving en Organisatie voor Klinisch Onderzoekers (eBROK)	2019	1.0
In-vivo NMR	2018	1.4
Pulse programming	2018	1.4
Bedrijfshulpverlening	2019, 2020	0.9
Project management	2019	0.6
Practical biostatistics	2020	1.1
Seminars and workshops		
PhD days	2018	0.6
4D flow MRI workshop, York	2019	0.6
Attended international conferences and symposia		
Society for Cardiovascular Magnetic Resonance	2018	1.1
Rembrandt Institute of Cardiovascular Science (RICS)	2018	0.3
Institute Quantivision (iQ)	2019	0.3
Society for Magnetic Resonance Angiography (SMRA)	2019, 2021	1.4
European Society for Magnetic Resonance in Medicine and Biology (ESMRMB)	2019	0.6
International Society for Magnetic Resonance in Medicine (ISMRM)	2018–2021	6.0
ISMRM Benelux	2018–2021	1.1
Presentations at international conferences and symposia		
Oral		
Cardiac 4D flow MRI using semi-automated retrospective valve tracking for assessment of severe mitral valve regurgitation *ISMRM, Paris*	2018	0.2
Whole-heart 4D flow MRI: comparison between pseudo-spiral undersampling with compressed sensing reconstruction and EPI readout *ISMRM Benelux, Leiden*	2019	0.2

Machine learning for automatic three-dimensional segmentation of the aorta in 4D flow MRI *iQ, Amsterdam*	2019	0.2
Quantification of mitral valve regurgitation from 4D flow MRI using semi-automated flow tracking *SMRA, Nantes; ESMRMB, Rotterdam*	2019	0.4
Coronary Flow Assessment with Accelerated 4D Flow MRI *ISMRM Benelux, Arnhem; ISMRM, virtual; SMRA, virtual*	2020	0.6

Poster

Cardiac 4D flow MRI using semi-automated retrospective valve tracking for assessment of severe mitral and aortic valve regurgitation *SCMR, Barcelona*	2018	0.2
Mapping of reversed flow and wall shear stress in aortas with bicuspid valves *RICS, Noordwijkerhout*	2018	0.2
Whole-heart 4D flow MRI: comparison between pseudo-spiral undersampling with compressed sensing reconstruction and EPI readout *ISMRM, Montreal*	2019, 2021	0.2

Teaching

Tutoring

Data analysis in MATLAB	2020	0.3

Supervising

Pit Spee, 3-month BSc graduation project	2019	2.0
Sheryl ten Hove, 5-month MSc graduation project	2020–2021	2.0
Fatima el Kharraz, 3-month BSc graduation project	2021	2.0

Parameters of esteem

ISMRM educational stipend	2018, 2019
SMRA travel award	2019

International journal reviewing

Magnetic Resonance Materials in Physics, Biology and Medicine, two articles	2019, 2020
International Journal of Cardiovascular Imaging	2019

Other

Candidate interview for NWO Industrial Doctorates call	2018
Audio slides for YouTube channel JMRI	2018
Grant proposal for NWO Open Mind call	2020

8.3 Acknowledgements

Onderweg naar die begeerde titel heb ik gelachen en gehuild, maar me altijd gesteund gevoeld door velen. Dit proefschrift is niet compleet zonder een dankwoord aan alle lieve mensen die er op directe of indirecte manier aan hebben bijgedragen.

Beste **Aart**, ik kan me haast niet voorstellen dat er een fijnere afdeling bestaat dan Z0 om als PhD-student te werken. Dat is te danken aan het team dat jij bij elkaar hebt weten te krijgen. Op Z0 is overal een mouw aan te passen en is de enige beperking je eigen verbeelding (en het aantal beschikbare scanuren). Gedurende mijn promotietraject heb ik me vrij gevoeld om niet alleen mijn enthousiasme en ideeën maar ook mijn twijfels en soms zelfs wanhoop met je te delen. Jij nam ze allemaal even serieus, dankjewel daarvoor.

Beste **Nils**, bedankt voor je vertrouwen in mij om een rol te vervullen in de klinische 4D flow-droom. Er zijn tijden geweest dat ik me overweldigd voelde door deze taak. Juist op die momenten bracht jij orde en helderheid, en wist je me te prikkelen oplossingsgericht te denken. Jouw mentaliteit is er een van rustig blijven maar ook doorpakken als het moeilijk wordt. Jouw visie, creativiteit en moed zijn als brandstof geweest voor mijn promotietraject. Veel dank daarvoor.

Beste **Pim**, bij onze eerste kennismaking liet jij vallen dat ik na mijn stage in Chicago wel een PhD kon komen doen op Z0. Ik dacht dat het een grapje was en vergat het weer. Wat ben ik blij dat je me een paar maanden later daadwerkelijk vroeg! Tijdens mijn PhD gaf je me de vrijheid die ik nodig had om echt zelfstandig onderzoeker te worden. Als ik dreigde te verdwalen in die vrijheid wist je me met een simpele “ja zou ik doen” of “nee zou ik niet doen” weer in de juiste richting te wijzen. Je stond altijd klaar met advies, en hebt me geleerd strakker dan strak te schrijven. Maar ik herinner me ook vooral de supergezellige borrels met je in binnen- en buitenland!

Many thanks to **my opponents**, who were so kind to accept the invitation to read my thesis and discuss it with me during the defense ceremony.

Mijn dank gaat ook uit naar alle **vrijwilligers** en **patiënten** die mij een kijkje lieten nemen in hun prachtige harten.

Lieve **Lukas**, toen ik op Z0 kwam kijken was jij de aangewezen persoon om mij wegwijs te maken in de donkere krochten van alles wat met PROUD 4D flow te maken had. Je voelde als een grote broer wiens aandacht ik moest zien te winnen. Hoe leuk dat we zijn uitgegroeid tot echte maatjes! Jij hebt een hart van goud en een stel hersenen waar je u tegen zegt. Maar bovenal ook de wil om die twee te delen met de mensen om je heen. Dankjewel daarvoor.

Lieve **Bobby**, **Koen** en **Liza**, wat hebben we wat afgelachen. De roadtrip in Canada met jullie heeft een speciaal plekje in mijn hart. Op de werkvloer waren jullie mijn go-to collega's om wel en wee mee te delen en stoom bij af te blazen. Dankjulliewel dat ik mijn gekke zelf bij jullie kon zijn. De musicalzang met Koen, volkszang van Bobby en schapenlach-imitatie van Liza zullen me nog lang bijblijven.

Dear **Eric**, it was as if Aart had sent an angel from heaven when you entered the scene. Thank you for your tireless contributions to the coronaries project, and words of encouragement when I needed them. Your calm and confident energy – and, most of all, expertise – were the keys to success.

Dear **prof. dr. Markl**, if it wasn't for the opportunity you offered me back in 2016 to gain experience in your lab, I may have never ended up doing this PhD. Thank you for your generous hospitality.

Chiel, **Josien**, **Jules** en **Paul**, mag ik jullie uitroepen tot het clinical 4D flow dreamteam? Zelfs de meetings waren in een soort automatische pipeline gegoten! **Anita**, **Joena**, **Raschel** en **Sandra**, jullie rol in het slagen van mijn projecten is substantieel geweest – of het nu was in de vorm van scanondersteuning of het draaiende houden van de afdeling. Dankjewel dat ik op jullie kon bouwen. **Anne**, **Anouk**, **Eva**, **Daphne**, **Jasper**, **Johan**, **Kadere**, **Marieke**, **Melissa**, **Myrte**, **Nienke**, **Oliver**, **Ot**, **Renske**, **Sofieke**, **Toni**, **Viktor** en **Zarah**, fijnere collega's dan jullie had ik me niet kunnen wensen. Ik kan niet anders dan de parallel trekken met een familie! **Bram**, **Gustav**, **Hugo**, **Laura**, **Mariah** en **Susi**, als Z0 familie is, dan zijn jullie *extended family*. Nooit te beroerd het AMC te doorkruisen voor wat gezelligheid of een helpende hand! **Emile**, veel PhD tips en tricks heb ik van jou geleerd al voordat ik goed en wel begonnen was aan mijn promotietraject, dankjewel daarvoor. **Jean-Paul**, **Jos** en **Joe**, ik kijk terug op een fijne samenwerking. Dankzij jullie werk is valve tracking de wereld aan het veroveren!

Lieve **paranimfen**, ik ben enorm blij om jullie naast me te hebben tijdens de verdediging. Lieve **Sophie**, al sinds de Ideeweek en Natuurkundepracticum tover jij een lach op mijn gezicht met jouw *vibrant* energie en heerlijke humor. Je hebt een aanstekelijk enthousiasme voor alles wat met wetenschap te maken heeft, maar neemt het nooit té serieus. Dear **Sassi**, during those four years, our friendship was so many times exactly what I needed. Sometimes we just hung out, sometimes we danced, did yoga or had long talks about the struggles of being a PhD-student – or young woman in general. You encouraged me to take a step back when I got too caught up in work, and at the same time you fully understood because you had been there yourself. Thank you for being there.

Lieve **vrienden**, de energie, blijdschap en inspiratie die ik haal uit het contact met jullie neem ik ook mee in mijn werkzame uurtjes! Lieve **Shruti**, wat ben ik blij met een vriendin als jij. Jij begrijpt mij soms beter dan ikzelf. Je moedigt me altijd aan om me te blijven vernieuwen en weet me het lichtje aan het einde van de tunnel te laten zien als het even tegenzit. Je bent een inspiratie voor me! Lieve **Floor**, het voelt als gisteren dat we als brugwup partners-in-crime door de gangen van het Strabrecht wandelden. We hadden lol om dingen die alleen wij begrepen, en dat hebben we nog steeds :) De band met jou is er een die nooit af zal nemen. Lieve **Amber**, **Irma**, **Jenna**, **Loes**, **Mirte**, **Natascha** en **Ruby**, tijd doorbrengen met jullie geeft me altijd zoveel energie! Juist omdat we allemaal zo verschillend zijn wordt het nooit saai. De weekendjes weg met jullie zijn goud waard; ik hoop dat we die er nog lang in houden. Lieve **Willemijn**, kleine meisjes worden groot :) We hebben al heel wat mijlpalen van elkaar meegemaakt en ik hoop dat er nog veel mogen volgen! Lieve **Anniek**, **Margo**, **Marjolein**, **Naomi** en **Sophie**, als ik terugkijk op onze vriendschap over de jaren dan denk ik aan veel gekkigheid, gezelligheid en groepsgevoel. Jullie hebben mijn studietijd gemaakt tot de fijne tijd die hij was. Maar ook in de jaren erna zijn jullie altijd een stabiele factor gebleven, waar ik heel dankbaar voor ben. Lieve **Victor**, met jou raak ik nooit uitgepraat. Ook al zullen onze toevallige encounters op het AMC nu stoppen, we blijven elkaar zien! Dear **Isi**, I'm so happy we kept in touch after our time in Chicago. You are as sensitive and reflective as I am and that makes it so good to spend time with you. Our half-yearly get-togethers have been the perfect getaway to reset my mind and feel refreshed again. Dear **Eric** and **Rhiannon**, from the moment you guys set foot in our house, I felt like we would become friends. I'm so happy we did! Getting to know you has been a ray of light in the darkness of covid. A special word of thanks goes out to **Hermes**, who made even the toughest article deadline into a bearable one. Lieve **Olivia** en **Gregor**, **Ray** en **Ingrid**,

ik kom altijd met pijn in mijn lachspieren thuis van avondjes met jullie. Ik hoop dat we nog eens een echte Koningsdag met elkaar mogen meemaken! Tot slot wil ik ook **ctrl+F** en **Thesaurus.com** bedanken, op wiens hulp ik altijd kon rekenen.

Lieve **Sanne**, dankzij jou is dit boekje niet alleen een boekje maar ook een kunstwerk. Ik had niet durven dromen dat het zo mooi zou worden! Dankjewel voor de magie die je erop losgelaten hebt.

Lieve **Mieke**, bedankt voor je wijze woorden en schop onder de kont toen het laatste jaar van mijn PhD eruit zag als een monster. Je herinnerde me aan mijn kracht! En het is allemaal gelukt!

Lieve **Fenna**, dankjewel dat je mij met open armen ontvangen hebt en dat ik altijd op je advies kan rekenen. Ik kijk uit naar nog veel etentjes, weekendjes weg en kledingpassessies. Lieve **Thomas** en **Anne**, **Lennart** en **Tinke**, jullie zijn als een warm nest voor me. Bedankt dat jullie altijd klaarstaan om met mij mee te filosoferen over levensvragen, dilemma's en ambities. Lieve **papa** en **mama**, wat ik in de afgelopen vier jaar aan kennis heb opgedaan is in de verste verte niet te vergelijken met de schat aan dingen die jullie me hebben geleerd. Doorzettingsvermogen, het vormen van je eigen oordeel, creativiteit, zelfredzaamheid; het zijn maar voorbeelden. Dankzij jullie kan ik de wereld aan.

Lieve lieve **Jan**, wat is er mooier dan een dankwoord te mogen schrijven aan de persoon die me elke dag aan het lachen maakt, inspireert, motiveert en in zijn armen sluit? Jouw liefdevolle steun heeft me door de heetste vuren heen geholpen. Met jou ervaar ik nooit stilstand. Jij laat me voelen dat wat er ook gebeurt: we zijn een team. Ik voel me een rijk mens met jou aan mijn zijde.
Ik hou van jou.

8.4 Curriculum vitae

Carmen Pieta Susanna Blanken was born on April 7th 1994 in Nuenen, the Netherlands. After having graduated from secondary school (Strabrecht College, Geldrop), she in 2012 started her bachelor studies in Medical Natural Sciences at Vrije Universiteit Amsterdam. She completed these in 2015 with a graduation project on the subject of optical coherence tomography. With a strong interest in the field of medical imaging, she continued studying at Vrije Universiteit Amsterdam for a master's degree in Medical Natural Sciences. During her master studies, she visited Northwestern University's Radiology department, Chicago, Illinois, USA for a three-month research internship on "Evaluation of aortic hemodynamics in patients with Sievers type 2 bicuspid aortic valve disease". This internship, supervised by prof. dr. Michael Markl, sparked her interest in cardiac magnetic resonance imaging. Back in the Netherlands, she completed her master studies with a six-month graduation project on "Cardiac 4D flow MRI using semi-automated retrospective valve tracking for assessment of severe mitral and aortic valve insufficiency" at the Radiology and Nuclear Medicine department of the Academic Medical Center in Amsterdam (now Amsterdam UMC). Her supervisors during this project – dr. R. Nils Planken, dr. ir. Pim van Ooij and prof. dr. ir. Aart J. Nederveen – granted her the opportunity to start a PhD in January 2018. During her PhD programme, Carmen worked on the innovation and validation of cardiac 4D flow MRI for blood flow quantification in valvular heart disease and coronary artery disease. She presented her work at various international conferences and supervised multiple students. Apart from her research tasks, she was involved in the implementation of cardiac 4D flow MRI into routine clinical practice at Amsterdam UMC.